UNIVERSITY OF ROCHESTER
LABORATORY FOR LASER ENERGETICS

Volume 103
April–June 2005
DOE/SF/19460-626

LLE Review

Quarterly Report

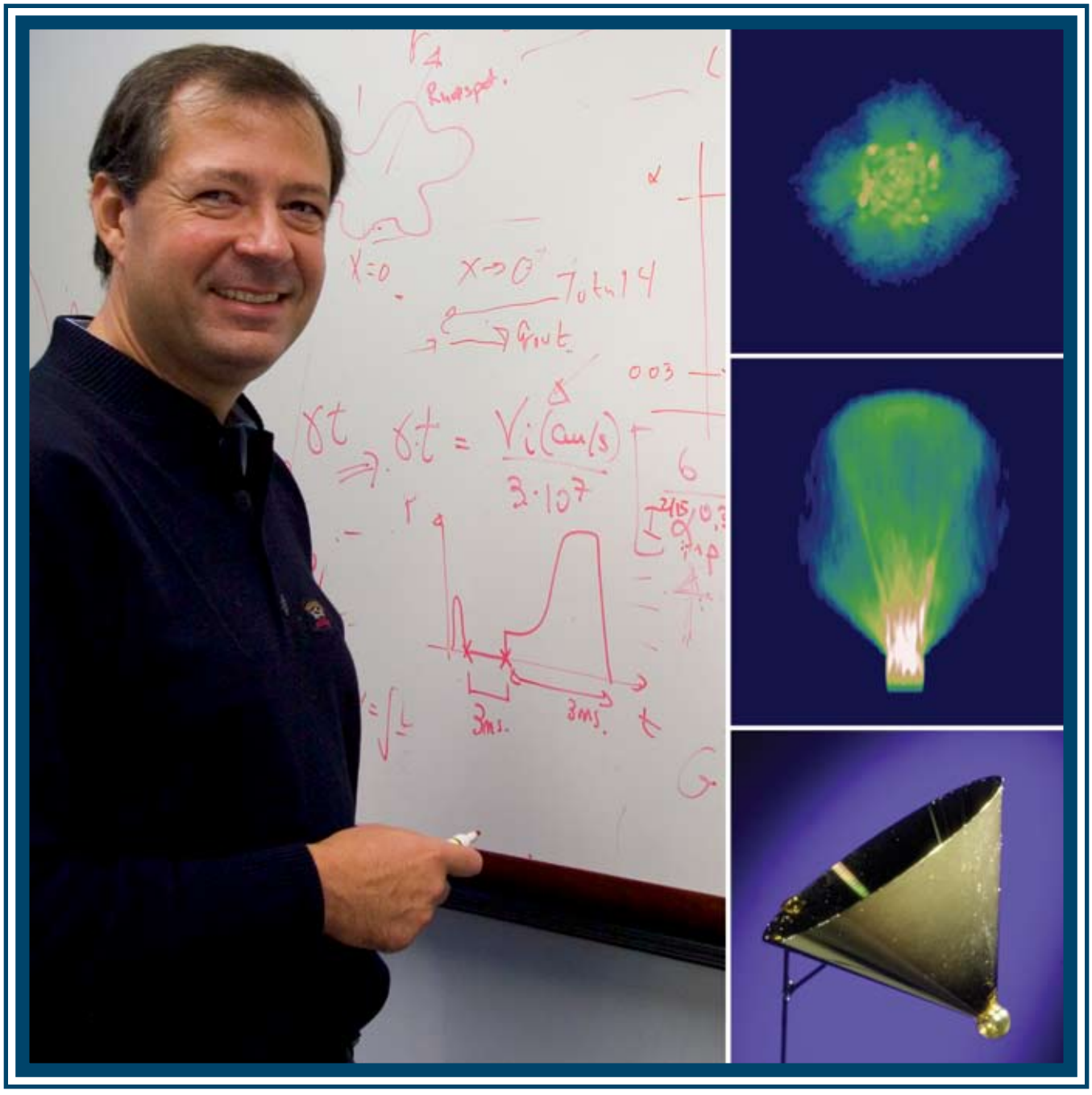

About the Cover:

The cover shows a picture of Dr. Riccardo Betti, director of the newly formed University of Rochester Fusion Science Center (UR-FSC), deriving scaling relations that can be used to optimize implosion parameters for fast-ignition targets. The target-design goal for fast ignition is to achieve a cold, high-density, high-ρR assembly of thermonuclear fuel. Once assembled, the fuel is ignited by fast electrons generated by an ultra-intense petawatt laser pulse (such as that provided by the OMEGA EP Facility). Images from numerical calculations of fast-electron transport in such targets appear to the right along with a cone-in-shell target.

Inside cover: Members of the University of Rochester Fusion Science Center: (from left to right) Chuandong Zhou (Dept. of Mechanical Engineering, Graduate Student, Research Assistant), Riccardo Betti (LLE and Dept. of Mechanical Engineering), Andrey Solodov (UR-FSC postdoctoral Research Associate), and Chuang Ren (Dept. of Mechanical Engineering).

The work described in this volume includes current research at the Laboratory for Laser Energetics, which is supported by New York State Energy Research and Development Authority, the University of Rochester, the U.S. Department of Energy Office of Inertial Confinement Fusion under Cooperative Agreement No. DE-FC03-92SF19460, and other agencies.

Printed in the United States of America
Available from
National Technical Information Services
U.S. Department of Commerce
5285 Port Royal Road
Springfield, VA 22161
Price codes: Printed Copy A04
Microfiche A01

For questions or comments, contact Jason Myatt, Editor, Laboratory for Laser Energetics, 250 East River Road, Rochester, NY 14623-1299, (585) 275-5772.

Worldwide-Web Home Page: http://www.lle.rochester.edu/

UNIVERSITY OF ROCHESTER
LABORATORY FOR LASER ENERGETICS

Volume 103
April–June 2005
DOE/SF/19460-626

LLE Review

Quarterly Report

UR LLE

Contents

In Brief

This volume of the LLE Review, covering April–June 2005, features "High-Density and High-ρR Fuel Assembly for Fast-Ignition Inertial Confinement Fusion" by R. Betti and C. Zhou. In this article (p. 117), the authors optimize implosion parameters for fast-ignition inertial confinement fusion and design fast-ignition targets relevant to direct-drive inertial fusion energy (IFE). It is shown that a 750-kJ laser can assemble fuel with $V_I = 1.7 \times 10^7$ cm/s, $\alpha = 0.7$, $\rho = 400$ g/cc, $\rho R = 3$ g/cm^2, and a hot-spot volume of less than 10% of the compressed core. If fully ignited, this fuel assembly can produce energy gains of 150.

In the second article (p. 122), C. Stoeckl, T. R. Boehly, J. A. Delettrez, V. Yu. Glebov, J. Miller, V. A. Smalyuk, W. Theobald, B. Yaakobi, and T. C. Sangster, along with J. A. Frenje, C. K. Li, R. D. Petrasso, and F. H. Séguin (MIT), S. P. Hatchett (LLNL), and R. B. Stephens (GA) describe recent OMEGA experiments that have studied the fuel assembly of gas-filled, cone-in-shell, fast-ignition targets. Using both fusion products and backlit images, an areal density of ~60–70 mg/cm^2 was inferred for the dense core assembly. The results are promising for successful integrated fast-ignition experiments on the OMEGA EP facility, scheduled to be completed in 2007.

Additional highlights of research presented in this issue include the following:

- D. Jacobs-Perkins, R. E. Earley, S. G. Noyes, M. J. Bonino, L. D. Lund, and R. Q. Gram describe a high-performance "planar" cryogenic target handling system that has been added to LLE's OMEGA Laser Fusion Facility (p. 128). The system has demonstrated a shot-to-shot cycle interval of less than two hours and has fielded more than 125 experiments using several distinct target types. This article provides an overview of the cryogenic capabilities at LLE and then compares operational requirements of LLE's spherical and planar cryogenic systems.

- V. A. Smalyuk, O. Sadot, J. A. Delettrez, D. D. Meyerhofer, S. P. Regan, and T. C. Sangster present nonlinear growth measurements of 3-D broadband nonuniformities near saturation using x-ray radiography in planar foils accelerated by laser light (p. 137). The initial target modulations were seeded by laser nonuniformities and later amplified during acceleration by Rayleigh–Taylor instability.

- W. T. Shmayda describes the significant developments in tritium-capture technology that have occurred over the past two decades (p. 142). The merits and drawbacks of the various technologies that have been developed for both air and inert gas streams are discussed.

- A. V. Okishev, R. G. Roides, I. A. Begishev, and J. D. Zuegel describe an all-solid-state, diode-pumped Nd:YLF laser system that has been developed and tested (p. 155). It produces fiducial timing signals at three wavelengths (fundamental, second, and fourth harmonics) and will be used as a primary timing reference for the OMEGA facility diagnostics. Performance results of the new OMEGA fiducial laser are reported.

- B. Yaakobi, T. R. Boehly, D. D. Meyerhofer, and T. J. B. Collins of LLE and B. A. Remington, P. G. Allen, S. M. Pollaine, H. E. Lorenzana, and J. H. Eggert of LLNL present extended x-ray absorption fine structure (EXAFS) measurements (p. 161). These have been used to demonstrate the phase transformation from body-centered-cubic (bcc) to hexagonal-closely-packed (hcp) iron due to nanosecond, laser-generated shocks. This is a direct, atomic-level, and *in-situ* proof of shock-induced transformation in iron.

Jason Myatt
Editor

High Density and High ρR Fuel Assembly for Fast-Ignition Inertial Confinement Fusion

Introduction

In direct-drive inertial confinement fusion,[1] a cryogenic shell of deuterium and tritium (DT) filled with DT gas is accelerated inward by direct laser irradiation (direct drive). The energy gain G is defined as the ratio between the thermonuclear energy yield and the laser energy on target. The gain is directly related to the capsule implosion velocity $G = \left(1/V_I^2\right)\eta_h \theta E_f / m_i$, where V_I is the implosion velocity, $\eta_h = E_K/E_L$ is the hydrodynamic efficiency representing the ratio between the shell kinetic energy and the laser energy on target, E_f = 17.6 MeV is the energy of the fusion products for a DT fusion reaction, and $m_i = 2.5\, m_H$ is the average ion mass. The function θ represents the fraction of burned fuel depending on the fuel areal density $\rho R \equiv \int_0^R \rho dr$. The function $\theta = \theta(\rho R)$ is commonly approximated[1] by $\theta \simeq \left(1 + 7/\rho R\right)^{-1}$, where ρR is given in g/cm^2. If the driver energy is kept constant, higher implosion velocities require lower masses. In this case, the effect on the ρR of a lower mass balances the effect of higher velocity, thus making ρR independent of velocity. The hydrodynamic efficiency[1] depends on the ratio between the initial M_0 and final mass M_1 of the capsule; $\eta_h \propto \left(M_1/M_0\right)\left(\ln M_1/M_0\right)^2/\left(1 - M_1/M_0\right)$. The difference $M_a = M_0 - M_1$ is the ablated mass, and the approximation $\eta_h \propto \left(M_a/M_0\right)^{0.87}$ can be used for $M_a < 0.7\, M_0$. The ablated mass is proportional to the ablation velocity V_a, the in-flight shell density $\rho_{\rm if}$, the implosion time t_I, and the ablation surface area $\sim R^2$; $\left[M_a \sim \rho_{\rm if} V_a R^2 t_I\right]$. By setting $M_0 \sim \rho_{\rm if} R^2 \Delta_{\rm if}$ ($\Delta_{\rm if}$ is the in-flight thickness) and by using the well-known scaling relation[1] $V_a \sim \alpha_{\rm if}^{3/5} I_L^{-1/5}$, where $\alpha_{\rm if}$ is the in-flight adiabat and I_L is the laser intensity, one can easily rewrite $\left(M_a/M_0\right) \sim \alpha_{\rm if}^{3/5} A_{\rm if}/V_I I_L^{1/15}$, where $A_{\rm if}$ is the in-flight aspect ratio and the relation $t_I \sim R/V_I$ has been used. Since the aspect ratio[1] scales as $A_{\rm if} \sim M_{\rm if}^2$ (where $M_{\rm if}$ is the in-flight Mach number), the final scaling of the hydro-efficiency can be easily derived by substituting $\rho_{\rm if} \sim \left(p_{\rm if}/\alpha_{\rm if}\right)^{3/5}$ into the Mach number, and[1] $p_{\rm if} \sim P_L \sim I_L^{2/3}$, where P_L is the laser-driven ablation pressure. A straightforward manipulation yields $\eta_h \sim V_I^{0.87} I_L^{-0.29}$, which compares favorably with a numerical fit obtained from 1-D hydrodynamic simulations

$$\eta_h^{\rm fit} \approx \frac{0.049}{I_{15}^{0.25}}\left[\frac{V_I\left({\rm cm/s}\right)}{3\times 10^7}\right]^{0.75}, \tag{1}$$

where I_{15} is the laser intensity in 10^{15} W/cm^2. The simulations are for ten direct-drive cryogenic targets with laser energies varying from 25 kJ to 1.5 MJ and are carried out using the 1-D code *LILAC*.[2] The targets used in the simulations are either all DT ice or wetted-foam CH(DT)$_6$ capsules with a 2-μm CH overcoat. Substituting the hydro-efficiency into the gain formula yields a thermonuclear gain that increases for the lower implosion velocities

$$G \approx \frac{73}{I_{15}^{0.25}}\left[\frac{3\times 10^7}{V_I\left({\rm cm/s}\right)}\right]^{1.25}\left(\frac{\theta}{0.2}\right). \tag{2}$$

Equation (2) shows that, if ignited, slow targets yield high gains. The energy required for ignition from a central hot spot, however, increases rapidly as the velocity decreases[3] $\left(E_{\rm ign}^{\rm hot-spot} \sim V_I^{-6}\right)$. This is because the hot-spot temperature increases with the velocity. Since the fusion cross section is a strong function of the temperature, slow targets have a relatively cold hot spot and therefore require greater energy for ignition. If the implosion velocity is below 2×10^7 cm/s, the hot spot cannot be ignited regardless of the shell energy since the radiation losses dominate the hot-spot energy balance. However, such slow targets can be optimal for fast ignition (FI) since the hot-spot size and energy decreases with the implosion velocity.

In fast ignition,[4] a relatively cold, high-density, and high-areal-density assembly of thermonuclear fuel is ignited by the external heating of a small volume of the dense fuel. The external heating is provided by fast electrons accelerated by the interaction of an ultra-intense petawatt (= 10^{15} W) laser pulse with either the coronal plasma or a solid target. The fast electrons slow down in the cold, dense fuel and release their kinetic energy through collisions with the electrons.

The electron range is measured in terms of the fuel areal density that, for a 1-MeV electron beam,[5] is about 0.4 to 0.6 g/cm^2. The igniter beam energy required for fast ignition increases inversely to the fuel density.[6] According to Ref. 6, the 1-MeV e-beam ignition energy follows the simple formula $E_{\rm ign}^{\rm fast} = 11\left(400/\rho_f\right)^{1.85}$, where ρ_f is the dense fuel density in g/cc. In order to keep the petawatt laser energy in the range of a few tens of kilojoules, the thermonuclear fuel density needs to exceed the value of about 300 g/cc. However, higher densities require higher beam intensities and a smaller beam radius;[6] $r_b\left(\mu{\rm m}\right) \simeq 15\left(400/\rho_f\right)$. Because of the difficulties in focusing the electron beam at radii less than 10 μm, fuel densities within the 300 to 500 g/cc range are desirable. In addition to the density range, fast ignition requires that the volume of the hot spot be much smaller than the dense core volume to reduce the thermal energy of the hot spot in favor of the internal energy of the compressed fuel. Furthermore, a small-size hot spot limits the detrimental effects of the central low-density plasma on the burn wave propagation that starts in the dense volume. Other fuel-assembly requirements come from the specific applications of FI. For inertial fusion energy (IFE) applications, the thermonuclear gain must be greater than 100 and the areal density must be at least 2.5 to 3 g/cm^2. Here we show that a fuel assembly meeting all these requirements can be produced with a direct-drive laser facility in the 700 kJ range, about half the size of the National Ignition Facility[7] and significantly smaller than the multimegajoule drivers required for direct-drive IFE based on hot-spot ignition.

Scaling Laws for Density, Areal Density, and Stagnation Aspect Ratio

We start our analysis by deriving a scaling law for the shell density, areal density, and hot-spot size as a function of characteristic implosion parameters such as shell energy, implosion velocity, and in-flight adiabat. By indicating with Δ_s the stagnating shell thickness, with R_h the hot-spot radius and M_s the shell mass, the compressed shell areal density scales as

$$\rho_s\Delta_s \sim M_s/R_h^2\Sigma\left(A_s\right) \sim E_K/R_h^2V_I^2\Sigma\left(A_s\right),$$

where E_K is the shell kinetic energy at the end of the acceleration phase, $A_s = R_h/\Delta_s$ is the stagnation aspect ratio, and $\Sigma\left(x\right) = 1 + 1/x + 1/3x^2$ is a volume factor. The hot-spot radius R_h can be derived by setting the total shell internal energy at stagnation equal to the shell kinetic energy $E_K \sim p_s\left(R_h + \Delta_s\right)^3$, where the stagnation pressure p_s has been assumed to be approximately uniform through the hot spot and shell. This energy conversion condition (from kinetic to internal) can be rewritten by setting $p_s \sim \alpha_s\rho_s^{5/3}$, where $\alpha_{\rm s}$ is the stagnation adiabat that is related[8] to the in-flight adiabat $\alpha_{\rm if}$ through the in-flight Mach number $\alpha_s \sim \alpha_{\rm if}M_{\rm if}^{2/3}$, leading to $\alpha_s \sim \alpha_{\rm if}^{0.8}V_I^{0.67}/P_L^{0.13}$. It follows that the shell density and the shell areal density can be rewritten as

$$\rho_s\Delta_s \sim \Phi\left(A_s\right)E_K^{0.33}V_I^{0.67}I_L^{0.09}\alpha_{\rm if}^{-0.8} \tag{3}$$

and

$$\rho_s \sim \Psi\left(A_s\right)V_I^2I_L^{0.13}\alpha_{\rm if}^{-1.2}, \tag{4}$$

where

$$\Phi\left(x\right) \equiv \left(x^2 + x + 1/3\right)^{2/3}/\left(1 + x\right)^3$$

and

$$\Psi\left(x\right) = \left[\Phi\left(x\right)\left(1 + x\right)\right]^{9/4}.$$

Though the stagnation aspect ratio is of order unity, it is important to accurately determine its functional dependency on the implosion parameters. For reasonable values of the stagnation aspect ratio ranging between $1 < A_s < 4$, Φ and Ψ can be approximated with a power law as $\Phi\left(A_s\right) \sim 1/A_s^{0.92}$ and $\Psi\left(A_s\right) \sim 1/A_s^{0.62}$. A_s grows with the implosion velocity since the mass decreases for a fixed energy leading to smaller Δ_s, while R_h depends mostly on energy. In order to determine an accurate dependence on the velocity, we fit the results of the simulations where R_h is defined as the point of maximum shell density, and Δ_s is the distance between R_h and the return shock at the time of peak areal density. The simulations show a clear dependence on the velocity and almost no dependence on energy and adiabat leading to

$$A_s^{\rm fit} \approx 2.1\left[\frac{V_I\left({\rm cm/s}\right)}{3 \times 10^7}\right]^{0.96}, \tag{5}$$

as shown in Fig. 103.1. Substituting Eq. (5) into (3) and (4) yields scaling laws for the density and areal density

$$\rho_s\Delta_s \sim E_L^{0.33}V_I^{0.03}\alpha_{\rm if}^{-0.8}, \quad \rho_s \sim V_I^{1.4}I_L^{0.13}\alpha_{\rm if}^{-1.2}, \tag{6}$$

where the hydro-efficiency from Eq. (1) has been used. These semi-analytical scaling laws compare favorably with the numerical fits of the peak values of the densities and areal densities

$$\left(\rho R\right)_{\max}^{\text{fit}} \approx \frac{1.3}{\alpha_{\text{if}}^{0.55}}\left[\frac{E_L\,(\text{kJ})}{100}\right]^{0.33}\left[\frac{V_I\left(\text{cm}/\text{s}\right)}{3\times 10^7}\right]^{0.06} \tag{7}$$

and

$$\rho_{\max}^{\text{fit}} \approx \frac{788}{\alpha_{\text{if}}}\, I_{15}^{0.13}\left[\frac{V_I\left(\text{cm}/\text{s}\right)}{3\times 10^7}\right], \tag{8}$$

where the subscript max indicates the maximum values during the implosion and ρR and $\rho_{\max}$ are in g/cm^2 and g/cc, respectively. The laser-intensity scaling in (8) is analytical from (6) since the intensity varies only within a ±15% range in the simulation, and it does not represent a good scaling parameter. Note the density scaling is somewhat different from the indirect-drive scaling shown in Ref. 9. The areal density in Eq. (7) includes the inner portion of the shell that has been compressed by the return shock as well as the surrounding portion that has not been shocked. Typically, the unshocked portion has significantly lower density and lower ρR with respect to the shocked portion (see Fig. 103.4 on p. 121). In a $\rho R \sim 3$ g/cm^2 implosion, however, a 20% fraction of unshocked ρR can stop energetic electrons at lower densities (with $\rho < 300$ g/cc), preventing them from reaching the dense shocked core. The presence of the unshocked areal density has important consequences on the choice of the fast-ignition time. If the fast electrons have 1-MeV energy, then the fast-ignition time is when the unshocked areal ρR is significantly less than 0.6 g/cm^2, which occurs after the time of peak ρR. This constraint is relaxed as the fast-electron energy exceeds 1 MeV. Note that Eq. (8) represents the maximum density. The time of peak ρR occurs after the time of peak density, and the average density at the time of peak ρR is slightly below 80% of Eq. (8). If fast ignition is triggered at or soon after the time of peak ρR, the corresponding average density is significantly below its maximum value.

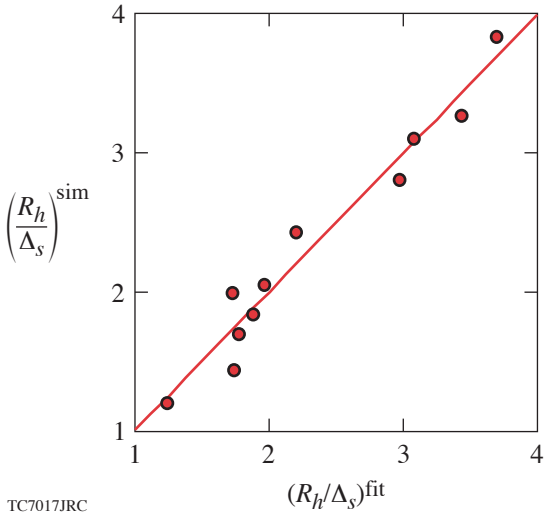

Figure 103.1
Hot-spot aspect ratio from simulation compared with numerical fit (9).

Laser Pulse Shaping

Other important considerations in optimizing fast-ignition targets concern the pulse length and laser power contrast ratio. It is clear from Eqs. (7) and (8) that low adiabat implosions lead to high densities and areal densities. However, very low adiabat implosions require long pulse lengths and careful pulse shaping. The long pulse length is because of the slow velocity of the low-adiabat shocks, and the careful shaping is required to prevent spurious shocks from changing the desired adiabat. Furthermore, the ratio between the peak power and the power in the foot of the laser pulse (i.e., the power contrast ratio) increases as the adiabat decreases thus leading to difficult technical issues in calibrating the pulse shape. These constraints on the pulse shape are relaxed by using the relaxation (RX) laser pulse technique.[10] The relaxation pulse consists of a prepulse followed by an interval of laser shutoff and the main pulse. The RX pulse induces an adiabat profile that is monotonically decreasing from the ablation surface to the inner shell surface. In addition to improving the hydrodynamic stability of the implosions, the RX main pulse is shorter and requires a lower contrast ratio than the equivalent flat adiabat pulse with the same inner surface adiabat.

High-Gain Fast-Ignition Capsule Design

By using the results in Eqs. (5), (7), and (8), a high-gain fast-ignition capsule can be designed. We start by setting a low value for the inner-surface adiabat $\alpha_{\text{if}}^{\min} \approx 0.7$. An adiabat below unity implies that, at shock breakout, the inner portion of the shell is not fully ionized. In order to achieve a $\rho R \approx 3$ g/cm^2, Eq. (7) yields a laser energy $E_L \simeq 750$ kJ [the velocity term in Eq. (7) has been ignored because of the low power index]. Equation (8) is then used to determine the velocity required to obtain a peak density of 640 g/cc that corresponds to an average density of the shocked shell at the time of peak ρR of $\langle\rho\rangle \simeq 0.8\,\rho_{\max} \simeq 500$ g/cc. The corresponding velocity from (8) is $V_I = 1.7\times 10^7$ cm/s, leading to a hot-spot aspect ratio [Eq. (5)] of $A_s \sim 1$. Since the required laser energy of 750 kJ is approximately half the NIF energy, we use a reference driver with half the energy and half the power of the NIF. For a peak power of 220 TW, the outer shell radius is chosen to keep the

peak intensity at 10^{15} W/cm^2, thus leading to $R_{out} \simeq 1.3$ mm. The target mass at stagnation is derived from the kinetic energy $M_s \approx 2E_K/V_I^2$, with $E_K \approx \eta_h E_L$. Using Eq. (1) for η_h and $E_L = 750$ kJ, $V_I \approx 1.7 \times 10^7$ cm/s yields a stagnation mass of $M_s \simeq 1.7$ mg. Assuming that ~20% of the mass is ablated leads to an initial mass of about $M_0 \simeq 2$ mg. In order to improve the laser energy absorption, we consider a wetted-foam target with an inner ice layer, an outer wetted-foam $CH(DT)_6$ layer, and a 2-μm CH overcoat. Given the low density of the foam and the small thickness of the overcoat, we can assume that the average density is the same as DT ice, $\rho_0 \simeq 0.25$ g/cc, and determine the inner-shell radius from the volume $\sim M_0/\rho_0$ and the outer radius leading to $R_{inn} \simeq 660$ μm. Figure 103.2 shows the FI target with a foam layer thickness that is large enough to reabsorb the coronal radiation and reduce the radiation heating of the inner ice layer. It is important to notice that the large shell thickness combined with the slow implosion velocity makes the target performance insensitive to the hydrodynamic instabilities and 1-D codes suitable for realistic simulations of the implosion. The 750-kJ RX pulse is shown in Fig. 103.3. The main foot-pulse length is about 22 ns, and the power contrast ratio is about 150. Those pulse characteristics are not far from the NIF indirect-drive pulse requirements with a pulse length of ~18 ns and a contrast ratio of ~100. A *LILAC* simulation of the 750-kJ implosion yields the exact desired implosion parameters. Substituting the implosion parameters into the gain formula (1) yields a thermonuclear gain of about $G = 220/(1 + E_{PW}/750)$, where E_{PW} is the petawatt laser energy required for ignition in kilojoules. This is probably an optimistic assessment since it assumes that the peak value of the areal density is available at the time of ignition. Figure 103.4 shows the density profiles versus the areal density at different times about the peak ρR time. The sharp drops in density shown in Fig. 103.4 correspond to the return shock traveling outward from the center. Notice that the density varies significantly while the total ρR remains above 2.5 g/cm^2. Ignition can therefore be triggered at an average density varying from 300 to 550 g/cc without significant changes to the target gain. It is important to observe that the areal density of the low-density unshocked portion of the shell is significant and decreases with time from 0.9 g/cm^2 at time of $\rho R = 3$ g/cm^2 to 0.3 g/cm^2 at the time $\rho R = 2.5$ g/cm^2. This implies that the electron energy in the fast-ignitor beam needs to exceed 1 MeV to allow the electron penetration into the high-density core. The density versus volume plots in Fig. 103.5 indicate that the hot-spot volume is less than 10% of dense core during hundreds of picoseconds about the time of peak ρR. Notice that at 27.5 ns, the density is about 300 g/cc, and its profile is approximately uniform. The "hot-spot" volume is small, and values below $\rho < 300$ g/cc are confined within a tiny region occupying only 6%–7% of the core.

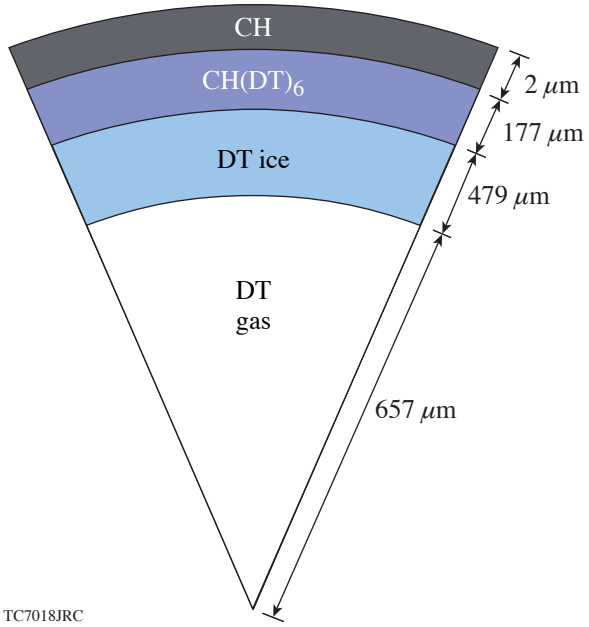

Figure 103.2
Fast-ignition IFE target.

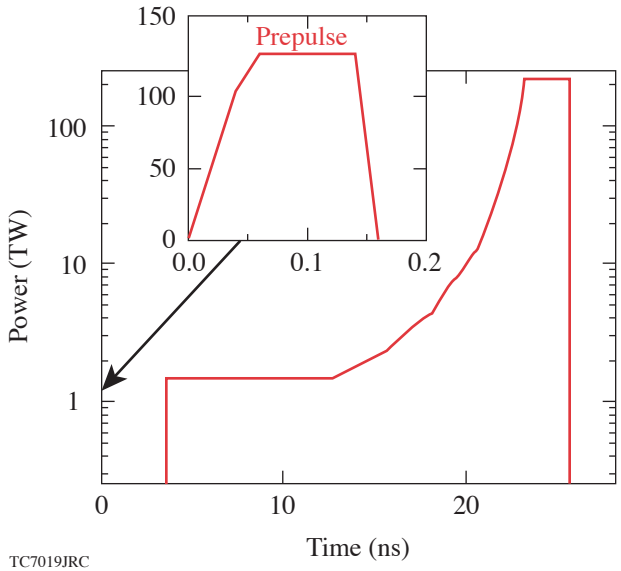

Figure 103.3
750 kJ, $\alpha = 0.7$ relaxation laser pulse.

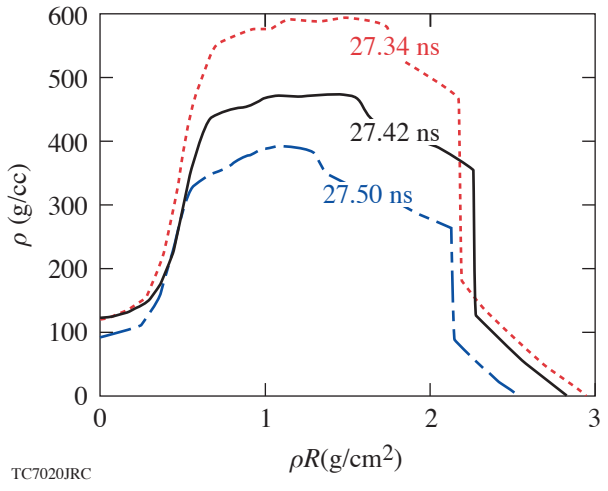

Figure 103.4
Density profiles versus areal density at three times about the time of peak areal density.

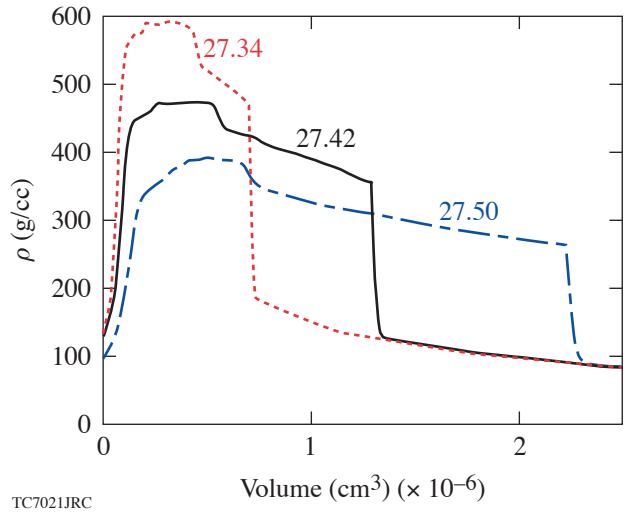

Figure 103.5
Density profiles versus volume at three times about the time of peak areal density.

ACKNOWLEDGMENT

This work has been supported by the US Department of Energy under Cooperative Agreement DE-FC02-04-ER54789 and DE-FC52-92SF19460, the University of Rochester, and the New York State Energy Research and Development Authority. The support of DOE does not constitute an endorsement by DOE of the views expressed in this article.

REFERENCES

1. S. Atzeni and J. Mer-ter-Vehn, *The Physics of Inertial Fusion: Beam Plasma Interaction, Hydrodynamics, Hot Dense Matter*, International Series of Monographs on Physics (Clarendon Press, Oxford, 2004); J. D. Lindl, *Inertial Confinement Fusion: The Quest for Ignition and Energy Gain Using Indirect Drive* (Springer-Verlag, New York, 1998).

2. J. Delettrez and E. B. Goldman, Laboratory for Laser Energetics Report No. 36, University of Rochester (1976).

3. M. C. Herrmann, M. Tabak, and J. D. Lindl, Nucl. Fusion **41**, 99 (2001).

4. M. Tabak *et al*., Phys. Plasmas **1**, 1626 (1994).

5. C. Deutsch *et al*., Phys. Rev. Lett. **77**, 2483 (1996); **85**, 1140(E) (2000); C. K. Li and R. D. Petrasso, Phys. Rev. E **70**, 067401 (2004).

6. S. Atzeni, Phys. Plasmas **6**, 3316 (1999).

7. E. M. Campbell and W. J. Hogan, Plasma Phys. Control. Fusion **41**, B39 (1999).

8. R. Betti, K. Anderson, V. N. Goncharov, R. L. McCrory, D. D. Meyerhofer, S. Skupsky, and R. P. J. Town, Phys. Plasmas **9**, 2277 (2002).

9. S. A. Slutz and M. C. Herrmann, Phys. Plasmas **10**, 234 (2003).

10. R. Betti, K. Anderson, J. Knauer, T. J. B. Collins, R. L. McCrory, P. W. McKenty, and S. Skupsky, Phys. Plasmas **12**, 042703 (2005).

Direct-Drive Fuel-Assembly Experiments with Gas-Filled, Cone-in-Shell, Fast-Ignition Targets on the OMEGA Laser

Introduction

The fast-ignition concept for inertial confinement fusion[1,2] has the potential for higher gains and lower driver energies than central hot-spot ignition.[3] The fast-ignition concept separates the fuel assembly and heating by using an ultrafast laser. The ultrafast laser produces relativistic electrons with high efficiency (up to 50% has been reported[4]) that heat the fuel, significantly easing the requirements on the compression driver.[2,5] Laser or heavy-ion beam-heated hohlraums or direct-drive laser are options for the compression driver.

The biggest challenge of the fast-ignition concept is the transport of the relativistic electrons from the critical-density region ($n_e \sim 10^{21}$ cm^{-3} for a typical 1-μm laser), where the ultrafast laser is absorbed and converted into electrons, to the compressed fuel—a distance that can be hundreds of microns in an ignition-scale target. For an electron beam divergence of >20°, the overlap between the electron beam originating from a small focal spot (~10-μm radius) and the dense core with a diameter of <50 μm would be very small.[6,7] Most of the energy in the electron beam would be wasted. Two solutions have been proposed to minimize this standoff distance: a channeling beam to bore a hole in the plasma atmosphere around the core[2,8] that allows the ultrafast laser to be absorbed closer to the core and a re-entrant cone to keep the path of the ultrafast laser free of plasma and bring it as close as possible to the dense core.[9–11]

A few experiments have been performed to assess the potential of the re-entrant–cone concept. Integrated experiments at ILE-Osaka examined the coupling between the electron beam and the compressed core and found a 20%–30% energy transfer.[11,12] A thousand-fold increase in neutron yield from 10^4 to 10^7 was observed by coupling a 0.5-PW, short-pulse laser into an empty CD target imploded by 2.5 kJ of laser light at a wavelength of 0.53 μm. A first series of hydro experiments[13] with re-entrant cone targets in indirect-drive geometry on OMEGA studied the fuel assembly with 1 kJ of x-ray energy coupled to the capsule. Significant mixing between the gold cone and plastic shell material was observed. Mixing gold into the dense fuel/shell material substantially increases the required ignition energy. Stephens *et al.* predicted that using direct drive would minimize the mixing between the gold cone and the fuel/shell material.[13] Plasma filling the inside of the cone where the ultrafast laser has to propagate is another issue for cone targets. The high-pressure core plasma sends a shock wave through the gold cone that creates a plasma inside the cone when it breaks out, significantly increasing the electron propagation distance.

Fuel-assembly experiments with gas-filled, direct-drive, re-entrant cone-in-shell targets were performed on the OMEGA Laser System[14] to study whether the cone-in-shell design is scalable to higher-energy densities and in preparation for future integrated experiments on the OMEGA EP laser,[15,16] which will be operational in 2007. The experimental setup is described in the next section, which includes the laser configuration and imaging diagnostic arrangement. **Fuel Assembly in 35° and 70° Cone Targets** (p. 123) discusses backlighting of the fuel assembly of 35° and 70° cone targets. **Mixing of Au Cone and Core Material** (p. 124) reports an analysis of the mixing of cone and shell material, and **Compressed Core Areal Density Measurements** (p. 125) describes areal-density measurements using nuclear diagnostic methods. **Cone Filling** (p. 125) shows measurements of the shock breakout into the inside of the cone. Conclusions are presented in the last section, which also describes prospects for integrated experiments using the OMEGA EP laser.

Experimental Setup

Several different laser configurations were used for the direct-drive, cone-in-shell experiments on the 60-beam OMEGA laser. The targets were illuminated at a wavelength of 351 nm with a 1-ns square pulse and an energy of ~400 J per beam using two-dimensional smoothing by spectral dispersion (SSD)[17] with 1-THz bandwidth in the UV and polarization smoothing (PS).[18] The beams driving the shell used distributed phase plates (DPP).[19] For the backlighting experiments, 15 beams (~6-kJ energy) were diverted to a backlighter foil of either vanadium (V) or iron (Fe) and focused to a spot size of

600 μm without DPP's. To provide a nearly uniform illumination of the shell, 15 beams were run at half energy and 20 beams at full energy, a total of ~11 kJ of laser energy driving the implosion. The nuclear diagnostics experiments used 55 beams, with ~21 kJ of total energy. The cone-filling experiments used 48 beams for the 70° cones or 54 beams for the 35° cones to avoid the laser hitting the inside of the cones.

The targets consist of gas-tight, ~870-μm outer diameter, 24-μm-thick CH shells with a hollow gold cone with an opening angle of 35° or 70° inserted through a hole in the shell (see Fig. 103.6). The distance between the cone tip and the center of the shell, typically 30±10 μm, is defined by a shelf on the cone that provides a gas-tight interface for the assembly. Both the 70° and 35° gold cones had a thickness of roughly 100 μm outside the shell, approximately 10 μm inside the shell, and end in a hyperbolic-shaped tip with its asymptotes intersecting 12 μm from the target center resulting in an Au thickness of ~30 μm at the tip of the cone. Time-resolved x-ray framing cameras[20] recorded both backlit and self-emission images. The backlighter framing camera had an exposure time of ~40 ps and the self-emission camera ~80 ps. The framing cameras acquired 16 images with an ~60 ps temporal separation between exposures. Both cameras used a pinhole imager with a spatial resolution of ~10 μm in the target plane. The self-emission camera was filtered with ~200 μm of beryllium, with a lower cutoff at 50% transmission of ~3 keV. The backlighter camera used either a 25-μm-thick V filter to pass the predominantly He_α line emission of the V backlighter at 4.95 keV or a 25-μm-thick Fe filter for the He_α line emission of a Fe backlighter at 6.7 keV. These filters suppress the thermal radiation from the implosion, improving the contrast of the backlit images.

Fuel Assembly in 35° and 70° Cone Targets

A comparison of the fuel assembly between 35° and 70° cone targets is shown in Fig. 103.7. Backlit images from unfilled 35° [Fig. 103.7(a)] and 70° [Fig. 103.7(b)] targets were recorded using a Fe backlighter. Three images spaced ~250 ps apart

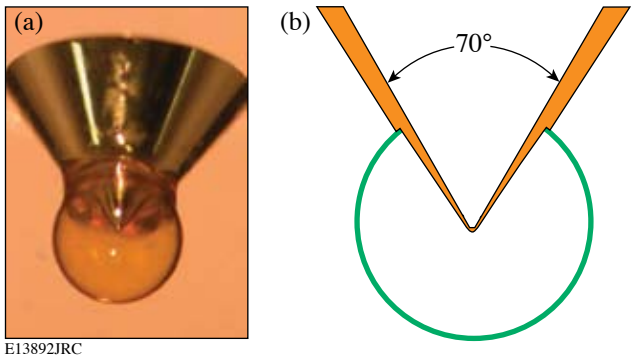

Figure 103.6
Picture of a gas-tight, fast-ignition cone target (a) and a schematic of its cross section (b). A gold cone with an opening angle of 70° is inserted through a hole in a 24-μm-thick CH shell of ~870-μm outer diameter.

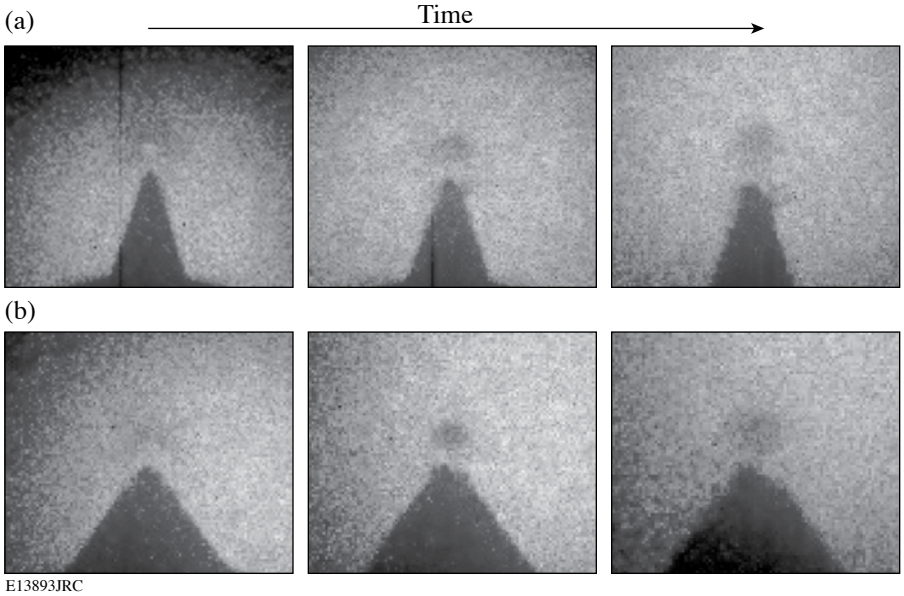

Figure 103.7
Backlit framing camera images from a 35° cone target (a) and a 70° target (b) using a Fe backlighter. Three images spaced ~250 ps apart show the assembly of the core and the erosion of the cone, with the central image close to the time of peak compression.

show the assembly of the core, with the central image close to the time of peak compression. The core assembly is similar in both cases, particularly the evolution of the core size. At early times, a horseshoe-shaped dense area is observed, with the opening toward the cone as expected. At peak compression, the core looks quite round and symmetric, with no influence of the cone visible. After peak compression, the core expands in an almost symmetric fashion. Both targets exhaust plasma toward the tip of the cone, eroding the tip at later times. The 35° targets shows less backlighter absorption in the core than the 70° cone targets, possibly due to the incomplete suppression of the core self-emission since the narrow cones are expected to disturb the implosion less and lead to higher core temperatures. The images also show that the plasma flow is directed from the core toward the tip of the cone, an indication that mixing gold and core material is not significant in these implosions.

Mixing of Au Cone and Core Material

Unfilled capsules were used to evaluate the mixing of the gold cone with the CH shell material to compare with previous indirect-drive experiments.[13] Figure 103.8 shows a backlit image using a V backlighter (a) and a self-emission image (b) taken at the time of peak compression. The backlit image shows absorption outside the original extent of the cone, as indicated by the dashed lines, showing that an expanding plasma is created on the surface of the cone. A gap between the cone tip and core assembly is seen in both images, unlike the data obtained using indirect drive.[13] The indirect-drive data were interpreted as a 0.04% mass density gold contamination in the compressed shell material. No signatures of mixing were observed in direct drive data; therefore, only an estimate of the minimum detectable gold contamination can be obtained from the analysis of the self-emission images. Figure 103.8(c) shows a lineout through the center of the self-emission image. A Gaussian fit of the core emission shows a symmetric core, with no indication of extra emission because of Au mixing into the core from the cone. At high temperatures (>1 keV) and moderate densities (<1 g/cm^3), the plasma conditions expected in the gap, the CH emissivity at 2 to 4 keV is roughly 2,000× smaller than the Au opacity. Consequently, a gold contamination of the order of 0.01% of the mass density in the gap would be visible as an ~10% enhancement of the emission, the estimated error of the symmetry of the emission profile. The x-ray emission from shell plasma in the gap between cone and core reduces the absorption minimum seen in the backlit image. This can be corrected using the self-emission images that show that the emission intensity in the gap is about 1/3 of the emission at the center of the collapsed shell. An analysis of corrected backlit images analogous to the self-emission images using the cold Au and the hot CH opacities shows no indication of gold plasma streaming into the core with a detection threshold of roughly 0.01% of the mass density.

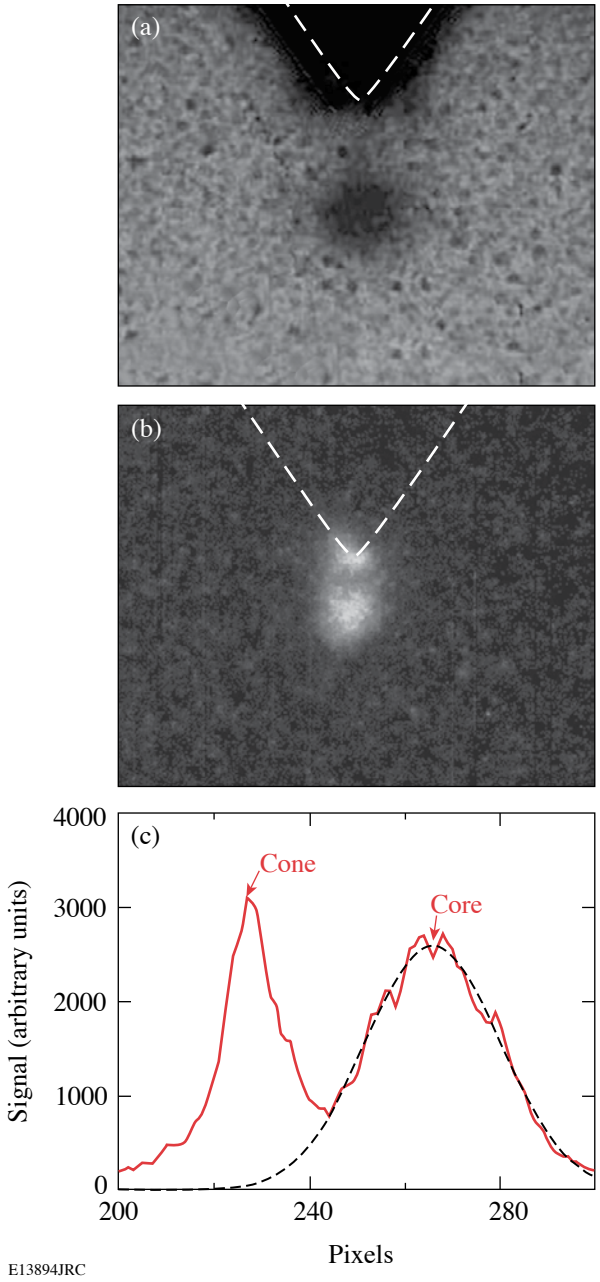

Figure 103.8
(a) Backlit and (b) self-emission x-ray framing camera images of unfilled cone targets obtained using pinhole imaging taken at peak compression. The extent of the cone before the laser shot is indicated with dashed lines. A lineout through the self-emission image is shown in (c).

Compressed Core Areal Density Measurements

The areal density of the assembled core was determined from experiments with targets filled with D^3He gas using nuclear diagnostics. Because of the strong He x-ray emission, the size and location of the hot-fuel region can be inferred from x-ray images of D^3He-filled targets. Figure 103.9(a) shows a backlit x-ray image of a 70° cone target filled with 10-atm D^3He at the time of peak proton production using a Fe backlighter at 6.7 keV. Wedged-range-filter spectrometers[21] are used to infer the areal density of the compressed shell[22,23] from the energy loss of the 14.7-MeV primary fusion protons. The proton spectrometers are deployed in two different directions ~15 cm from the target. Figure 103.9(a) shows the line of sight of the two proton spectrometers (labeled TIM1 and TIM3). Figure 103.9 also shows the proton spectra from three 35° cone targets imploded with 55 beams at 21 kJ with a total a proton yield (~3×10^6) integrated onto the wedged-range filters in TIM3 (b) and TIM1 (c). Two peaks are observed in the TIM3 spectrum, because the protons detected in TIM3 pass through the dense core (see Fig. 103.9). The narrow peak at ~14 MeV is attributed to the shock coalescence phase of the implosion, when the assembled areal density is low.[23] The second, broader peak at ~12 MeV is due to protons passing through the dense core close to peak compression.[23] An areal density of ~70±5 mg/cm^2 is inferred from the average energy downshift of ~2 MeV (Ref. 21). The protons detected on the TIM2 detector from both the shock and compression phases experience little energy loss and produce only a single narrow peak. The proton yields from the 70° cone targets were about a factor of 2 lower than the yields recorded from the 35° cone targets and showed marginally lower areal densities of ~60±10 mg/cm^2. A fuel ion temperature of 1.2±0.4 keV was inferred from the ratio of the D^3He proton and the DD neutron yields.[22]

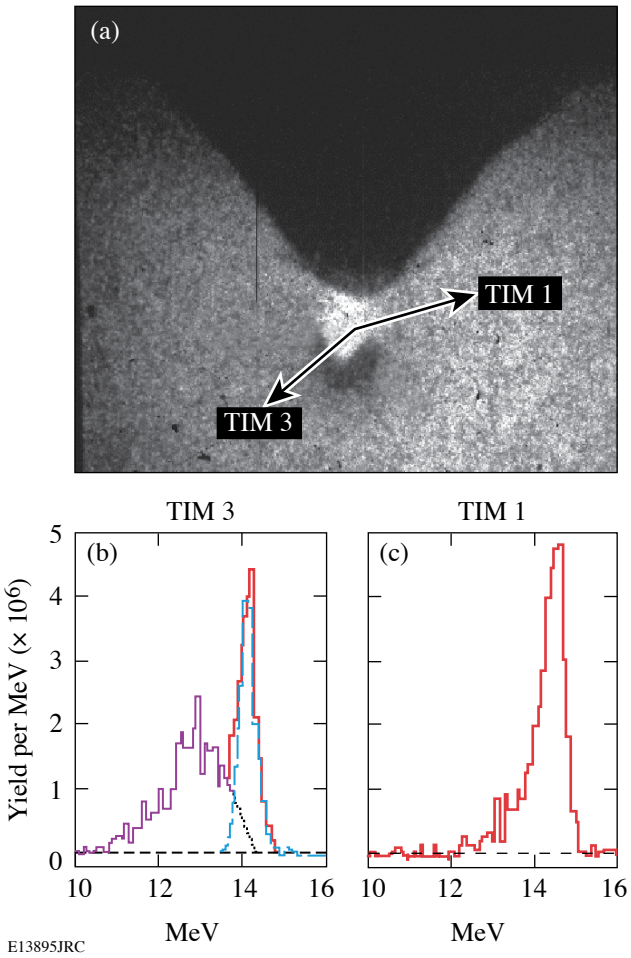

Figure 103.9
Backlit image (a) of a 10-atm, D^3He-filled cone target at time of peak proton production using a Fe backlighter. Significant self-emission from the hot D^3He gas is seen in the image. The directions of the proton spectrometers used to determine the core areal density are indicated as TIM1 and TIM3. D^3He proton spectra taken along two different lines of sight: TIM3 (b) and TIM1 (c).

The experimental areal density values were compared to simulations of full-sphere (no cone) implosions using the 1-D hydrocode *LILAC*.[24] *LILAC* predicts a total areal density (shell and fuel) of ~90 mg/cm^2 at the time of peak proton emission for a 24-μm-thick full spherical shell with an average ion temperature of 2.3 keV and a total proton yield of 3×10^8. The experimental areal density values are more than 66% of the predicted values in both cases. The measured ion temperature is much lower and the measured proton yield is almost three orders of magnitude lower than the simulation yield, showing that the presence of the cone reduces the central hot-spot temperature. Breaking the spherical symmetry by introducing a cone in the shell affects the ion temperature and consequently the proton yield much more than the fuel assembly and the core areal density. Reducing the cone angle from 70° to 35° has a small effect on the areal density. It improves the yield by a factor of 2, though it is still very far from the 1-D predictions.

Cone Filling

The filling of the inside of the cones was investigated using a streaked optical pyrometer (SOP)[25] (see Fig. 103.10). The SOP optical system images the inside of the tip of the cone onto the slit of the streak camera with an ~10-μm spatial resolution and a 500-μm field of view. The camera is filtered to record in a wavelength band centered at 660 nm with a 140-nm FWHM to minimize the background from scattered 3ω, 2ω, and 1ω laser light. The breakout of the shock produces a short burst of light.

Its timing relative to peak compression can be determined from the absolute temporal calibration of the SOP with an uncertainty of 50 ps. The shock temperature is inferred from the observed light signal using the absolute calibration of the SOP in intensity with an uncertainty of 10% above ~1 eV (Ref. 26). The number of laser beams used to drive the target is limited to prevent laser light from hitting the inside of the cone and produce a high background signal on the SOP. Figure 103.11(a) shows the SOP streak signal from a 70° cone target irradiated by 48 OMEGA beams with a total energy of ~18 kJ in a 1-ns square pulse. The time axis zero represents the start of the laser pulse. A very clean shock-breakout signal can be seen starting at the tip of the cone and becoming less intense and moving away from the tip as time progresses. Figure 103.11(b) shows a lineout through the center of the SOP trace in comparison with 1-D hydrocode simulations from *LILAC* of the total areal density of the compressed core for a spherical target. The 70° cone targets show a clean shock-breakout signal, similar to data seen in planar shock experiments.[27] The shock signal starts well after the time of peak compression (~500 ps) as calculated by *LILAC*, showing that the inside of the cone is free of plasma at the time when the short-pulse laser would propagate. An estimated shock temperature of ~10 eV is obtained using the absolute intensity calibration of SOP.

Conclusions

Fuel-assembly experiments with laser-irradiated, cone-in-shell targets performed on OMEGA indicate that this fast-ignition concept is likely to be scalable to higher energy cryogenic targets. No significant mixing of the gold from the cone with the fuel/shell material was observed, unlike the earlier results seen in the indirect-drive experiments. The core assembly is not severely affected by the presence of the cone, and more than 66% of the expected areal density is inferred from the experiments. Shock-breakout plasma does not begin filling the inside of the cone before peak compression when the ultrafast laser propagates.

In a cryogenic DT ignition capsule, the final core density will be higher, but the core pressure will be similar because of the lower average ionization of the DT compared to CH and the lower-drive adiabat.[28] This limits the strength and speed of the shock that causes the inside of the cone to fill with plasma and the erosion of the cone by the core plasma. The thin plastic shell containing the cryogenic fuel radiates much less in cryogenic implosions, reducing the heating and expansion of the gold cone at early times, which minimizes the amount of Au that can mix with the fuel.

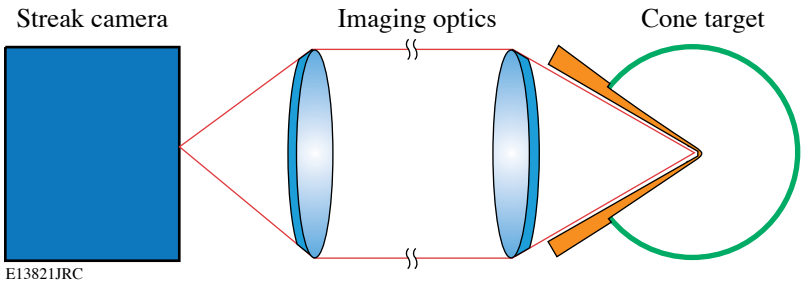

Figure 103.10
Streaked optical pyrometry (SOP) setup used to investigate the filling of the inside of the cone.

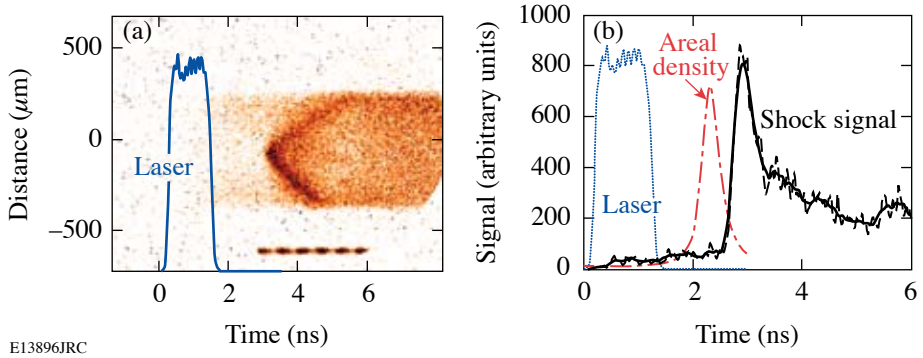

Figure 103.11
Streaked SOP signal from a 70° cone target (a) and lineout through the center of the signal (b) showing a clean shock breakout.

ACKNOWLEDGMENT

The authors are indebted to the Target Fabrication Groups at GA and LLE, especially Mark Bonino, Abbas Nikroo, and Joe Smith. This work was supported by the U.S. Department of Energy Office of Inertial Confinement Fusion under Cooperative Agreement No. DE-FC52-92SF19460, the University of Rochester, and the New York State Energy Research and Development Authority and with corporate support from General Atomics. The support of DOE does not constitute an endorsement by DOE of the views expressed in this article.

REFERENCES

1. N. G. Basov, S. Yu. Gus'kov, and L. P. Feokistov, J. Sov. Laser Res. **13**, 396 (1992).
2. M. Tabak *et al*., Phys. Plasmas **1**, 1626 (1994).
3. J. D. Lindl, R. L. McCrory, and E. M. Campbell, Phys. Today **45**, 32 (1992).
4. K. Yasuike *et al*., Rev. Sci. Instrum. **72**, 1236 (2001).
5. S. Atzeni, Phys. Plasmas **6**, 3316 (1999).
6. Y. T. Li *et al*., Phys. Rev. E **69**, 036405 (2004).
7. R. B. Stephens *et al*., Phys. Rev. E **69**, 066414 (2004).
8. Y. Kitagawa *et al*., Phys. Plasmas **9**, 2202 (2002).
9. M. Tabak *et al*., Lawrence Livermore National Laboratory Patent Disclosure, IL-8826B, Lawrence Livermore National Laboratory, Livermore, CA (1997).
10. P. A. Norreys *et al*., Phys. Plasmas **7**, 3721 (2000).
11. R. Kodama *et al*., Nature **412**, 798 (2001).
12. R. Kodama *et al*., Nature **418**, 933 (2002).
13. R. B. Stephens *et al*., Phys. Rev. Lett. **91**, 185001 (2003).
14. T. R. Boehly, D. L. Brown, R. S. Craxton, R. L. Keck, J. P. Knauer, J. H. Kelly, T. J. Kessler, S. A. Kumpan, S. J. Loucks, S. A. Letzring, F. J. Marshall, R. L. McCrory, S. F. B. Morse, W. Seka, J. M. Soures, and C. P. Verdon, Opt. Commun. **133**, 495 (1997).
15. C. Stoeckl, J. A. Delettrez, J. A. Kelly, T. J. Kessler, B. E. Kruschwitz, S. J. Loucks, R. L. McCrory, D. D. Meyerhofer, D. N. Maywar, S. F. B. Morse, J. Myatt, A. Rigatti, L. J. Waxer, J. D. Zuegel, and R. B. Stephens "High-Energy Petawatt Project at the University of Rochester's Laboratory for Laser Energetics," submitted to Fusion Science and Technology.
16. L. J. Waxer, D. N. Maywar, J. H. Kelly, T. J. Kessler, B. E. Kruschwitz, S. J. Loucks, R. L. McCrory, D. D. Meyerhofer, S. F. B. Morse, C. Stoeckl, and J. D. Zuegel, Opt. Photonics News **16**, 30 (2005).
17. S. Skupsky and R. S. Craxton, Phys. Plasmas **6**, 2157 (1999).
18. T. R. Boehly, V. A. Smalyuk, D. D. Meyerhofer, J. P. Knauer, D. K. Bradley, R. S. Craxton, M. J. Guardalben, S. Skupsky, and T. J. Kessler, J. Appl. Phys. **85**, 3444 (1999).
19. Y. Lin, T. J. Kessler, and G. N. Lawrence, Opt. Lett. **21**, 1703 (1996).
20. D. K. Bradley *et al*., Rev. Sci. Instrum. **66**, 716 (1995).
21. F. H. Séguin, J. A. Frenje, C. K. Li, D. G. Hicks, S. Kurebayashi, J. R. Rygg, B.-E. Schwartz, R. D. Petrasso, S. Roberts, J. M. Soures, D. D. Meyerhofer, T. C. Sangster, J. P. Knauer, C. Sorce, V. Yu. Glebov, C. Stoeckl, T. W. Phillips, R. J. Leeper, K. Fletcher, and S. Padalino, Rev. Sci. Instrum. **74**, 975 (2003).
22. C. K. Li, D. G. Hicks, F. H. Séguin, J. A. Frenje, R. D. Petrasso, J. M. Soures, P. B. Radha, V. Yu. Glebov, C. Stoeckl, D. R. Harding, J. P. Knauer, R. L. Kremens, F. J. Marshall, D. D. Meyerhofer, S. Skupsky, S. Roberts, C. Sorce, T. C. Sangster, T. W. Phillips, M. D. Cable, and R. J. Leeper, Phys. Plasmas **7**, 2578 (2000).
23. R. D. Petrasso, J. A. Frenje, C. K. Li, F. H. Séguin, J. R. Rygg, B. E. Schwartz, S. Kurebayashi, P. B. Radha, C. Stoeckl, J. M. Soures, J. Delettrez, V. Yu. Glebov, D. D. Meyerhofer, and T. C. Sangster, Phys. Rev. Lett. **90**, 095002 (2003).
24. J. Delettrez, R. Epstein, M. C. Richardson, P. A. Jaanimagi, and B. L. Henke, Phys. Rev. A, Gen. Phys. **36**, 3926 (1987).
25. J. A. Oertel *et al*., Rev. Sci. Instrum. **70**, 803 (1999).
26. J. Miller, Bull. Am. Phys. Soc **49**, 181 (2004).
27. R. E. Olson *et al*., Phys. Rev. Lett. **91**, 235002 (2003).
28. C. Stoeckl, C. Chiritescu, J. A. Delettrez, R. Epstein, V. Yu. Glebov, D. R. Harding, R. L. Keck, S. J. Loucks, L. D. Lund, R. L. McCrory, P. W. McKenty, F. J. Marshall, D. D. Meyerhofer, S. F. B. Morse, S. P. Regan, P. B. Radha, S. Roberts, T. C. Sangster, W. Seka, S. Skupsky, V. A. Smalyuk, C. Sorce, J. M. Soures, R. P. J. Town, J. A. Frenje, C. K. Li, R. D. Petrasso, F. H. Séguin, K. Fletcher, S. Padalino, C. Freeman, N. Izumi, R. Lerche, and T. W. Phillips, Phys. Plasmas **9**, 2195 (2002).
29. T. C. Sangster, J. A. Delettrez, R. Epstein, V. Yu. Glebov, V. N. Goncharov, D. R. Harding, J. P. Knauer, R. L. Keck, J. D. Kilkenny, S. J. Loucks, L. D. Lund, R. L. McCrory, P. W. McKenty, F. J. Marshall, D. D. Meyerhofer, S. F. B. Morse, S. P. Regan, P. B. Radha, S. Roberts, W. Seka, S. Skupsky, V. A. Smalyuk, C. Sorce, J. M. Soures, C. Stoeckl, K. Thorp, J. A. Frenje, C. K. Li, R. D. Petrasso, F. H. Séguin, K. A. Fletcher, S. Padalino, C. Freeman, N. Izumi, J. A. Koch, R. A. Lerche, M. J. Moran, T. W. Phillips, and G. J. Schmid, Phys. Plasmas **10**, 1937 (2003).
30. J. A. Delettrez, J. Myatt, P. B. Radha, C. Stoeckl, S. Skupsky, and D. D. Meyerhofer, "Hydrodynamic Simulations of Integrated Experiments Planned for OMEGA/OMEGA EP Laser Systems," submitted to Plasma Physics and Controlled Fusion.

Planar Cryogenic Target Handling Capability for the OMEGA Laser-Fusion Facility

Introduction

A high-performance "planar" Cryogenic Target Handling System has been added to LLE's OMEGA Laser-Fusion Facility.[1] Initially designed for equation of state measurements of liquefied D_2, it's versatility enables studies of Rayleigh–Taylor instabilities, shock timing, and cryogenic hohlraum performance. The system has demonstrated a shot-to-shot cycle interval of less than two hours and has fielded more than 125 experiments using several distinct target types. This article provides an overview of the cryogenic capabilities at LLE and compares the operational requirements of LLE's spherical and planar cryogenic systems. The unique features of the planar cryogenic system are described, and applications of this technology within the ICF community are discussed.

Direct-drive inertial confinement fusion (ICF)[2] implosion targets are susceptible to shell distortion because of Rayleigh–Taylor instability.[3] During the ablation phase, shock waves are launched into the capsule, resulting in compression of the fuel and gas core. Drive nonuniformities can be mitigated by rapidly heating the ablative surface of a fuel-containing capsule. Models used to predict how shock waves propagate in an ICF target and the resulting target performance depend on an accurate knowledge of the equation of state (EOS) of hydrogen isotopes at pressures exceeding 1000 GPa. Numerous experiments have been conducted in this regime using several different techniques with differing measured compressibility.[4]

LLE's planar Cryogenic Target Handling System [CTHS (Fig. 103.12)] is a versatile experimental platform used to study the EOS of D_2 using laser-driven shock waves. This apparatus was developed to obtain a better understanding of the discrepancies in prior experimental results. The planar CTHS leverages the technical expertise and infrastructure developed for direct-drive spherical cryogenic target experiments at LLE.[5–8] This system produces very repeatable experimental conditions with a short (~2 h) cycle time between target experiments and has been adapted to many different target and diagnostic configurations. Because of its versatile design, it is well suited to other applications like testing cryogenic sensors and evaluating tube-filled spherical ICF targets.

This article presents an overview of LLE's cryogenic target capabilities followed by a discussion of the operational differences between spherical and planar cryogenic experiments. Details of the planar CTHS hardware implementation and target construction are presented. Finally, performance of the planar cryogenic system is discussed.

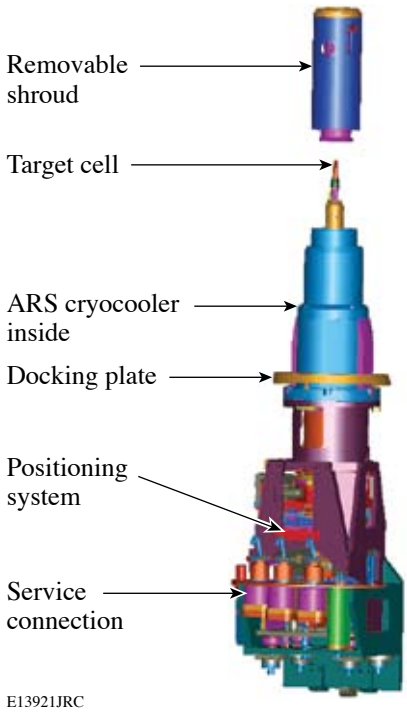

Figure 103.12
This moving cryostat (MC) was developed for cryogenic equation of state experiments. It occupies the same space envelope as a spherical MC. An MC module can be installed in approximately 4 h.

Overview

Since 1999, LLE has had the unique capability of diffusion-filling, freezing, layering, characterizing, and imploding thin-walled spherical cryogenic targets on the OMEGA Laser System.[5,6] This system requires an extensive infrastructure to support each stage of the process, as described in Refs. 7 and 8. The Planar and Spherical Cryogenic Target Handling Systems have much in common. In contrast, planar targets are filled through a tube from a self-contained reservoir, making the process much simpler than the diffusion-filling process used for spherical targets.

LLE's diffusion-filling apparatus for spherical ICF targets is located remotely from the OMEGA target chamber. Consequently, a self-contained transport system, known as the Moving Cryostat Transfer Cart (MCTC), was developed so that filled targets could be maintained at cryogenic temperatures indefinitely and transported between the filling and characterization stations and to the target chamber. The MCTC payload, known as the moving cryostat (MC), has several functions that include

- precisely controlling the thermal environment surrounding the target until moments before an implosion experiment,
- transporting targets ~6 m vertically into the target chamber, and
- providing fine-position control for the target once it is at target chamber center (TCC).

Cooling power for the MC is provided by a closed-cycle Gifford–McMahon helium refrigeration system.[9] A helium compressor is mounted on the MCTC, and a two-stage cryocooler is housed within the MC. The first stage of the cryocooler operates near 50 K, and the second stage operates between 10 and 20 K. Services for the MC, which include high-pressure helium lines, electrical conductors used for sensors and actuators, optical fibers, and exchange gas lines, are provided by an umbilical that extends and retracts with the MC.

Each MC assembly includes a multilayer removable shroud; its outer wall is at room temperature, whereas the inner walls are cooled. Once an MC is raised and secured at TCC, a four-axis positioner (X, Y, Z, rotation about Z) within the MC is used to position the target as it is viewed through windows in the shroud. A linear induction motor (LIM) then lowers a gripping mechanism that mates to the thermal shroud. Immediately before the laser is fired, the LIM rapidly pulls the shroud clear of all laser beams. The hardware supporting the target is designed so that it does not interfere with laser beam propagation.

The entire process is controlled by a combination of hardware and software interlocks, automated control systems, and operating procedures. Five MCTC's have been deployed. Currently, four are dedicated to spherical ICF experiments and one is configured for planar cryogenic target experiments. In all, more than two hundred cryogenic target experiments have been fielded on OMEGA.

Distinguishing Differences Between Spherical and Planar Moving Cryostats

The planar and spherical CTHS's are required to field (up to) 15 and 8 targets per 36-h shot week, respectively.[(a)] A major distinction between these systems is that a single planar MC can satisfy this requirement, whereas four spherical MC's are required. In addition, planar targets are hand-loaded into a warm MC, while spherical targets are transferred into a cold (~18 K) MC. The cycle time for planar targets includes cool down and warm up of the MC, whereas a spherical MC is not generally warmed between shots. As a result, the cycle time for planar targets is governed by the planar MC's thermal time constant and evacuation/vent times, while for spherical targets cycle times are dictated by the ice layering process.[8] Table 103.I summarizes some of the key requirements of, and differences between, the planar and spherical MC's.

The cooldown time (time to reach 18 K) for a spherical MC exceeds 3 h. Many MCTC's would have been required to satisfy the goal of 15 planar shots/week if the same MC were adapted for the planar experiments. Instead, a new planar MC having a short thermal time constant (τ_{th}) was developed. The required shot rate is satisfied using a single MCTC. The reduction of τ_{th} was possible because of the different operating requirements of the two systems, as discussed below.

Spherical cryogenic targets are cooled indirectly using helium "exchange" gas to conduct heat from the target to the surrounding cold copper "layering" sphere [Fig. 103.13(a)].[8] This design minimizes thermal gradients surrounding the capsule so that uniformly smooth ice layers form on the interior of the target shell. Exchange gas also allows the target support hardware to be mechanically decoupled from the cryocooler. The layering sphere is contained in the upper half

[(a)]Eight spherical target implosions have been carried out in a single week, but campaigns are currently planned assuming ≤4 shots/week to allow sufficient time to develop an ice layer and characterize it.

Table 103.I: Key differences and requirements for planar and spherical moving cryostats.

	Planar MC	Spherical MC
Target cooling method	Conduction through copper	Conduction through ~80 mTorr He exchange gas
Target temperature	13 to 30 K±50 mK (achieves <±10 mK)	17 to 21 K±10 mK
Target filling method	"Cryopumping" from integral reservoir through fill tube while target is in the MC	Diffusion filled in dedicated filling station, then frozen before transferring to the MC
Target installation method	Loaded by hand into the warm MC (open to atmosphere)	Mechanical manipulator transfers target at cryogenic temperature
Required shot rate	Up to 15 shots/week using ≤2 MCTC's	Up to 8 shots/week using 4 MCTC's
Laser beams required for target shots	Selected from all beams with $\theta < 155°$ (55 possible)*	All 60 beams
Target rotation	±5°	360°, continuous
Target heat source	Resistance heater	OPO IR laser, $\lambda = 3.16\ \mu$m

*θ is the angle measured relative to the vertical axis of the chamber. $\theta = 0°$ = top of chamber.

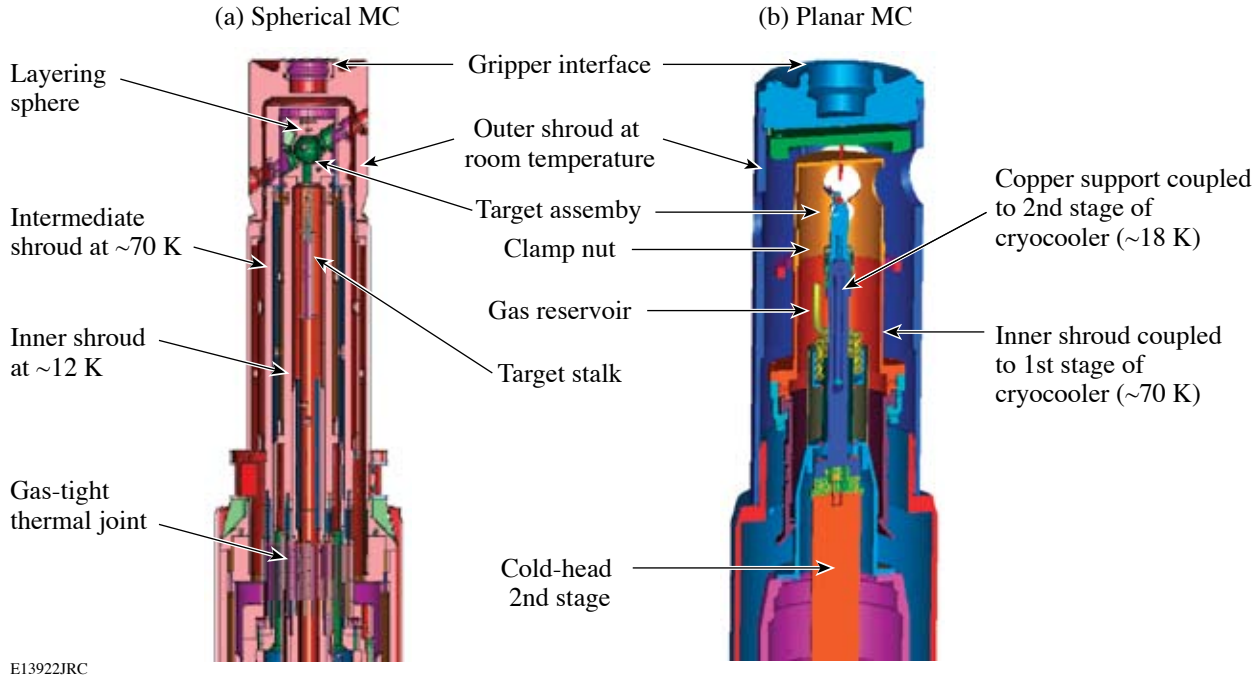

Figure 103.13
Exploded views of (a) a spherical MC and (b) a planar MC. The spherical system cools targets using a helium exchange gas; the planar system uses direct conduction through copper. These cross sections do not show the four-axis target positioners or the cold heads. The planar cold head is attached directly to the positioner; the spherical cold head is mechanically and thermally decoupled from the positioner.

of the shroud and is thermally connected to the second stage of the cryocooler.

The entire MC is inside the target chamber (maintained below 1×10^{-5} Torr); therefore, exchange-gas leakage from the spherical MC must be minimized. This constraint is satisfied by enclosing the (room temperature) fine-motion target positioner in a sealed box that mates to the upper shroud using complex, gas-tight, thermal joints. The room-temperature positioner is mechanically coupled to, but thermally isolated from, the target by means of a long slender "stalk." This stalk is supported near its midpoint by a compliant joint that provides the necessary degrees of freedom to position a target, including the full 360° rotation needed to characterize the ice layer.[10,11] The design chosen to satisfy these requirements separates the layering sphere from the cryocooler's second stage by nearly 0.6 m. Approximately 8 kg of material must be cooled to an average temperature of 14 K in order to freeze the D_2 fuel in a spherical target.

The layering sphere in a spherical MC has an optical fiber to transmit radiation heat from an optical parametric oscillator (OPO) IR laser source ($\lambda = 3.16\ \mu$m, matched to an absorption band of D_2) to heat the ice during the layering process.[8] This requires spherical shrouds to be equipped with optical fiber connectors as well as temperature sensors and a cryogenic photodetector to provide feedback for closed-loop control of the OPO. The planar system has no requirements for sensors in the shroud.

Vibration is a critical issue for the spherical MC.[6] Spherical target assemblies are delicate, supported by a slender stalk (and its compliant joint), and are susceptible to vibration sources that couple to the MC. Many hardware improvements have been made to mitigate vibration susceptibility, with more pending.

Planar Cryogenic Target Handling System

The planar MC was designed to be interchangeable with a spherical MC and to use a common control system. The planar MC module [Fig. 103.13(b)] can be interchanged with a spherical MC in approximately 4 h, giving a high degree of flexibility when planning experimental campaigns. Since its first use on OMEGA, one planar MCTC has been used for over 125 target shots with up to 5 shots per day. OMEGA typically has three shot days per week; one planar MC can meet the 15 shot per week requirement. Target fabrication, diagnostic setup, and personnel availability are often the rate-limiting factors in the shot cycle. Typically, ambient temperature shots are interleaved with planar cryo shots to take advantage of OMEGA's 1-h repetition rate.

The planar system was not required to use exchange gas and was required to have only ±5° of rotation, since coarse rotational alignment can be established by target design. These requirements were satisfied by mounting an ARS (Advanced Research Systems, Inc.)[12] cryocooler directly onto the planar MC's fine-motion positioner. The target is attached to the cryocooler's second stage using a high-thermal-conductivity copper support [Fig. 103.13(b)]. The resulting cold mass in the planar MC is less than 0.5 kg; therefore, the time constant τ_c is dramatically shorter than a spherical MC. This design is mechanically very stable and eliminates the exchange gas and complex thermal joints used on a spherical MC. Figure 103.14 shows the structure of the planar MC without a shroud.

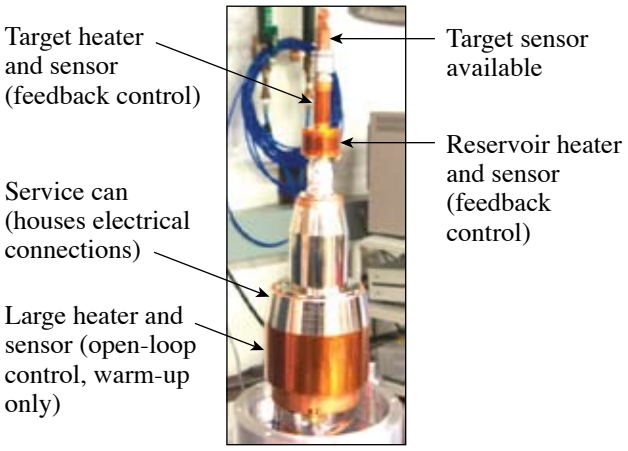

Figure 103.14
The internal structure of the planar MC (target is shown without reservoir).

Planar cryogenic experiments typically use a subset of OMEGA's 60 laser beams that are located no more than 65° below the equator, however, spherical targets with fill tubes could be fielded on the planar MC using all 60 beams.

1. Planar Cryogenic Target Design

The primary requirement for planar cryogenic targets is to contain liquid or solid D_2 in a cell having a 1-mm inside diameter and a 0.5-mm depth. Diffusion filling was deemed impractical; therefore, targets are filled through a tube from a local reservoir. Various options were considered, including supplying the fill gas through the umbilical and using valves and pressure sensors to meter the gas. This would have required a vent line in the umbilical to purge contaminants from the

target cell and fill lines. A much simpler approach was adopted; a sealed gas reservoir is connected to each target cell by a stainless steel capillary fill tube (Fig. 103.15). The reservoir (approximately 4-cc capacity at STP) is an accurately formed spiral copper tubing coil that is filled to a known initial temperature and pressure.

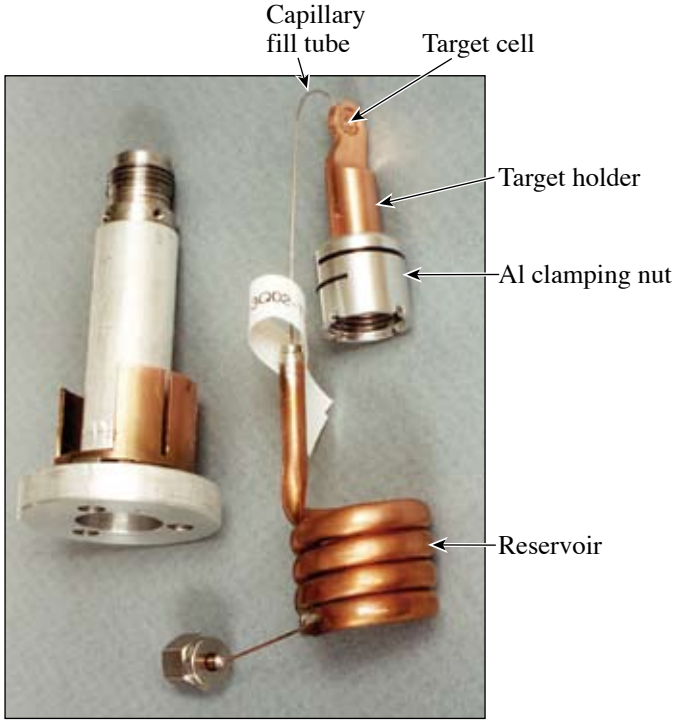

E13924JRC

Figure 103.15
A typical planar cryogenic target assembly (right) is shown beside an assembly fixture (left). The split aluminum nut maintains joint preload when cooled. The gas reservoir is connected to the target cell by a capillary tube.

Planar targets are filled off-line at room temperature. Purge gas is circulated through the reservoir/cell assembly and exits through vent tube attached to the cell. Blocked tubes are detected if the purge gas is not discharged through the vent tube. After purging, the vent tube is crimped to form a gas-tight seal, and the assembly is filled to the desired pressure (typically <2 atm). After reaching the desired pressure, the valve on the fill source is closed, and the reservoir pressure is monitored.[(b)] If the pressure decay is within acceptable limits, the fill line is crimped and the target is ready for use.

This design allows great flexibility in the choice of fill gas with no chance of cross-contamination between experiments. It minimizes the volume of gas released into the target chamber and limits the total gas inventory for each target in the event that DT targets are fielded using this system.

When conducting equation of state experiments, the MC maintains the gas reservoir at about 250 K. Once the cell reaches 20 K, gas begins to condense in the cell, creating a pressure gradient between the cell and reservoir. Condensation is monitored with cameras that view the target through the shroud windows, and the process continues until the cell is full. Given that the fill volume of a target cell is approximately 0.2 mm^3, it is not practical to install sensors in the cell. Instead, a temperature sensor is permanently installed in the copper adapter, immediately below the target holder.

Liquid D_2 density decreases at a rate of –1.3%/K from 20 to 24 K (Ref. 13). Targets that can withstand ice formation are cooled through the triple point (18.63 K) during shot preparation. The temperature at which an operator first observes ice formation in the cell is recorded. This calibrates the sensor with the accuracy needed to determine the initial state. Variations in observed triple-point measurements give a clear indication of the quality of the thermal joint formed between the target and the copper support [Fig. 103.13(b)]. Targets that cannot withstand ice formation are equipped with temperature and pressure sensors on the gas reservoir. These sensors are connected to the umbilical for readout by signal conditioning hardware external to the MCTC.

Thermal joints require preload to maintain intimate contact between mating surfaces. The thermal conductivity of a joint degrades if this preload decreases when it is cooled. The planar MC overcomes this difficulty by using a novel aluminum nut to clamp the copper target to the copper cryocooler adapter (Fig. 103.15). Spiral grooves on the nut's perimeter form bending-beam spring elements. Joint preload increases in a deterministic manner as the target assembly is cooled because of differential contraction of the aluminum and copper components. An optimized nut design results from properly choosing the cross section and length of the bending element. When a small amount of thermal grease is applied between the mating copper surfaces that have roughness ≤16 μin rms, the temperature drop across the joint is less than 1 mK, even when the nut is initially only finger-tight.

The gas reservoir rests inside a copper cup that is weakly coupled to the first stage of the cryocooler. The perimeter of the cup is split axially, forming a series of spring "fingers" similar to the assembly fixture in Fig. 103.15. A resistive foil heater

[(b)]The pressure sensor is part of the filling apparatus, not the target.

on a Kapton substrate[14] is wrapped around the cup to heat the reservoir. This joint also employs differential contraction to increase preload between the cup and reservoir as the heater's Kapton substrate cools and contracts. It is possible to operate with a differential up to 250 K between the reservoir and cell and still freeze D_2 in the cell.

Controlling the thermal gradient between the reservoir and target has several benefits. It permits control of gas transfer into the cell, prevents ice from obstructing the fill tube, and provides a heat source that controls the rate of ice formation in the cell. Void-free ice layers have been produced. Heat transfer through the fill tube is very low because it is made of low thermal conductivity stainless steel. The thermal conductivity of this path can be altered as needed by adding a thermal shunt or by altering the tubing's cross section, length, or material.

2. Target Cell Construction

A typical target cell is shown in Fig. 103.16; it consists of stacked components that are bonded together and then inserted into a copper holder. This modular design allows users to select from various windows, "pushers," cell sizes, and radiographic windows without altering the basic geometry. Copper holders are reused 2 to 3 times or until laser-induced damage is too severe. Reservoirs can be reused many times after replacing the fill and vent tubes.

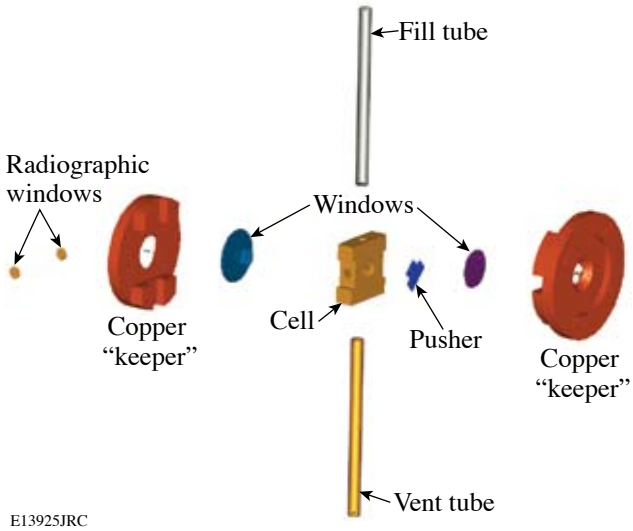

Figure 103.16
A target cell assembly consists of several elements that enclose a gas-tight volume of approximately 1-mm diameter and 500-μm deep. Fill and vent tubes are soldered to the cell. Some cells have radiographic windows (far left) that permit the driven shock to be imaged using an x-ray camera.

The outermost rings, referred to as "keepers," clamp the assembly into the holder. Safety wires are wrapped through holes in the keepers and holder to minimize debris ejection into the target chamber. The tension in these safety wires is critical to their effectiveness. Two opposing wires are tightly twisted, and the remaining two are relatively loose. The tight pair suffers from the initial impact and generally fail. The remaining pair of safety wires generally survive, allowing the entire assembly to be retrieved.

Although this modular target design is robust, fabrication is time consuming and requires highly skilled technicians to achieve satisfactory results. Some early targets failed because of gas leakage or blockage of the fill tube. These and other problems have been virtually eliminated with the processes that have been developed and the quality-control measures employed.

3. Shroud Construction

The spherical MC shrouds use a complex design, primarily because of the exchange-gas requirement. The heat capacity of the planar system allows it to be operated without a shroud and still freeze the fill gas. When practical, a shroud is used to minimize the possibility of condensate formation on the target and other cold components in the MC. The inner shield of the shroud [Fig. 103.17(a)] is cooled by the cryocooler's first stage to below 70 K. Thin-film Kapton windows permit the target to be observed while the shroud is in place using the OMEGA target viewing system and the video camera on the active shock breakout diagnostic.[15] The upper-shroud thermal joint consists of a set of spring-loaded fingers [Fig. 103.17(b)] that maintain thermal conductivity with the lower half of the MC while accommodating large radial positioning errors. The shroud can accommodate targets of up to 50 mm in diameter. The planar MC shroud weighs 70% less than the spherical shroud (3.6 kg versus 12.7 kg), is far less costly to manufacture, and is robust. These shrouds require no maintenance.

4. Performance Results

The planar MC has a cooldown time of 50 min. It is a very robust and stable mechanical platform that can support a wide variety of targets. Figure 103.18 shows a flow chart of the shot process, including approximate times, based on the most rapid shot cycles achieved to date. Several processes are performed concurrently, such as diagnostic alignment and cooling. During warm-up, all heaters in the MC are run at maximum output. Once the MC reaches 70 K and it is isolated from the target chamber, heated dry nitrogen is used to vent the MCTC to ambient pressure. This prevents moisture from condensing in the multilayer insulation used in the MC that, in turn, reduces

the time required to achieve high vacuum for the next shot cycle. Variations in the shot cycle time are generally attributable to diagnostic preparation. Table 103.II summarizes performance achievements with planar and spherical MC's.

Figure 103.17
(a) The inner shroud of the planar MC operates at ~70 K during a target shot. Windows in the shroud permit the target to be imaged by the OMEGA target viewing system and the active shock breakout diagnostic. Window openings on the inner shroud are covered with Kapton film. (b) A compliant thermal joint connects the inner shroud to the cryocooler's first stage.

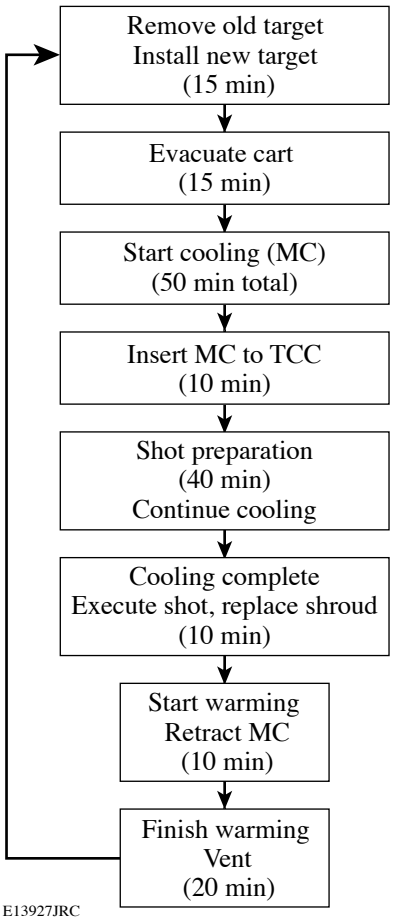

Figure 108.18
The shot cycle flow chart depicts how 2-h cycle times have been achieved.

Table 103.II: Cryocoolers used and resulting performance comparison between planar and spherical MC's.

	Planar MC	Spherical MC
Cryocooler model	ARS Displex DE204 60 Hz	Sumitomo RDK408S 60 Hz
Cryocooler load capacity	1 W at 10 K, 6 W at 16 K	1.8 W at 10 K, 9 W at 16 K
Target operating procedure	15 to 30 K	17 to 22 K
Mass cooled <50 K	<0.5 kg	8 kg
Maximum number of target shots/day	5, using single MCTC	4, using 4 MCTC's
Actual shot cycle using one MCTC (h)	<2	72 minimum
Cooldown time (min)	<50	>180

Future Applications

Many of the design features developed for, and proven on, LLE's planar Cryogenic Target Handling System are well-suited to other cryogenic applications within the ICF community and elsewhere. LLE may use the planar cryogenic system to evaluate the feasibility of filling spherical targets with a fill tube. Targets such as this may be used for cryogenic campaigns at the National Ignition Facility.[16]

The exceptional stability of the planar moving cryostat allows it to be used as a target chamber center alignment reference on OMEGA, both at vacuum and at ambient pressure. The planar MC serves as a "transfer standard" so that the target chamber center can be accurately established throughout the cryogenic system infrastructure, including the characterization stations used for layering spherical cryogenic targets.

Conclusion

This article has described a high-performance planar cryogenic target positioner for use on the OMEGA Laser System. Although initially designed for equation of state studies of cryogenic hydrogen isotopes, it is a versatile platform, readily adapted to suit a wide range of experimental designs. Through careful attention to experimental and operational requirements, this design has achieved shot-to-shot cycle times below two hours. Novel thermal joints employ differential contraction of dissimilar materials to maintain joint preload at all temperatures. The target has an integrated gas reservoir, permitting users wide latitude in designing experiments with different gasses. Modularity permits flexibility in designing each target. Many of these concepts are directly applicable to cryogenic devices being developed for the ICF community and elsewhere.

ACKNOWLEDGMENT

The authors would like to thank the entire LLE cryogenic support staff for their contributions in the development and operation of the P-CTHS. This work was supported by the U.S. Department of Energy Office of Inertial Confinement Fusion under Cooperative Agreement No. DE-FC52-92SF19460 and the University of Rochester. The support of DOE does not constitute an endorsement by DOE of the views expressed in this article.

REFERENCES

1. T. R. Boehly, D. L. Brown, R. S. Craxton, R. L. Keck, J. P. Knauer, J. H. Kelly, T. J. Kessler, S. A. Kumpan, S. J. Loucks, S. A. Letzring, F. J. Marshall, R. L. McCrory, S. F. B. Morse, W. Seka, J. M. Soures, and C. P. Verdon, Opt. Commun. **133**, 495 (1997).

2. J. D. Lindl, Phys. Plasmas **2**, 3933 (1995).

3. V. N. Goncharov, S. Skupsky, T. R. Boehly, J. P. Knauer, P. McKenty, V. A. Smalyuk, R. P. J. Town, O. V. Gotchev, R. Betti, and D. D. Meyerhofer, Phys. Plasmas **7**, 2062 (2000).

4. T. R. Boehly, D. G. Hicks, P. M. Celliers, T. J. B. Collins, R. Earley, J. H. Eggert, D. Jacobs-Perkins, S. J. Moon, E. Vianello, D. D. Meyerhofer, and G. W. Collins, Phys. Plasmas **11**, L49 (2004).

5. T. C. Sangster, J. A. Delettrez, R. Epstein, V. Yu. Glebov, V. N. Goncharov, D. R. Harding, J. P. Knauer, R. L. Keck, J. D. Kilkenny, S. J. Loucks, L. D. Lund, R. L. McCrory, P. W. McKenty, F. J. Marshall, D. D. Meyerhofer, S. F. B. Morse, S. P. Regan, P. B. Radha, S. Roberts, W. Seka, S. Skupsky, V. A. Smalyuk, C. Sorce, J. M. Soures, C. Stoeckl, K. Thorp, J. A. Frenje, C. K. Li, R. D. Petrasso, F. H. Séguin, K. A. Fletcher, S. Padalino, C. Freeman, N. Izumi, J. A. Koch, R. A. Lerche, M. J. Moran, T. W. Phillips, and G. J. Schmid, Phys. Plasmas **10**, 1937 (2003).

6. P. W. McKenty, T. C. Sangster, M. Alexander, R. Betti, R. S. Craxton, J. A. Delettrez, L. Elasky, R. Epstein, A. Frank, V. Yu. Glebov, V. N. Goncharov, D. R. Harding, S. Jin, J. P. Knauer, R. L. Keck, S. J. Loucks, L. D. Lund, R. L. McCrory, F. J. Marshall, D. D. Meyerhofer, S. P. Regan, P. B. Radha, S. Roberts, W. Seka, S. Skupsky, V. A. Smalyuk, J. M. Soures, K. A. Thorp, M. Wozniak, J. A. Frenje, C. K. Li, R. D.

Petrasso, F. H. Séguin, K. A. Fletcher, S. Padalino, C. Freeman, N. Izumi, J. A. Koch, R. A. Lerche, M. J. Moran, T. W. Phillips, G. J. Schmid, and C. Sorce, Phys. Plasmas **11**, 2790 (2004).

7. Laboratory for Laser Energetics LLE Review **81**, 21, NTIS document No. DOE/SF/19460-335 (1999). Copies may be obtained from the National Technical Information Service, Springfield, VA 22161.

8. D. R. Harding, T. C. Sangster, D. D. Meyerhofer, P. W. McKenty, L. D. Lund, and T. H. Hinterman, "Producing Cryogenic Deuterium Targets for Experiments on OMEGA," to be published in Fusion Science and Technology.

9. SHI-APD Cryogenics, Inc., A Subsidiary of Sumitomo Heavy Industries Ltd., Allentown, PA 18103-4783.

10. D. D. Meyerhofer, R. S. Craxton, L. M. Elasky, D. R. Harding, R. L. Keck, M. Pandina, W. Seka, M. D. Wittman, A. Warrick, and T. G. Brown, Bull. Am. Phys. Soc. **48**, 55 (2003).

11. D. H. Edgell, W. Seka, R. S. Craxton, L. M. Elasky, D. R. Harding, R. L. Keck, and M. D. Wittman, "Analysis of Cryogenic Target Shadowgraphs at LLE," to be published in Fusion Science and Technology.

12. Advanced Research Systems, Inc., Macungie, PA 18062.

13. P. C. Souers, *Hydrogen Properties for Fusion Energy* (University of California Press, Berkeley, 1986).

14. e.g., Minco, Minneapolis, MN 55432-3177.

15. R. J. Leeper, G. A. Chandler, G. W. Cooper, M. S. Derzon, D. L. Fehl, D. L. Hebron, A. R. Moats, D. D. Noack, J. L. Porter, L. E. Ruggles, J. A. Torres, M. D. Cable, P. M. Bell, C. A. Clower, B. A. Hammel, D. H. Kalantar, V. P. Karpenko, R. L. Kauffman, J. D. Kilkenny, F. D. Lee, R. A. Lerche, B. J. MacGowan, M. J. Moran, M. B. Nelson, W. Olson, T. J. Orzechowski, T. W. Phillips, D. Ress, G. L. Tietbohl, J. E. Trebes, R. J. Bartlett, R. Berggren, S. E. Caldwell, R. E. Chrien, B. H. Failor, J. C. Fernández, A. Hauer, G. Idzorek, R. G. Hockaday, T. J. Murphy, J. Oertel, R. Watt, M. Wilke, D. K. Bradley, J. Knauer, R. D. Petrasso, and C. K. Li, Rev. Sci. Instrum. **68**, 868 (1997).

16. J. Edwards *et al*., Phys. Plasmas **12**, 056318 (2005).

Fourier-Space, Nonlinear Rayleigh–Taylor Growth Measurements of 3-D Laser-Imprinted Modulations in Planar Targets

Introduction

The unstable growth of target nonuniformities is the most important factor that limits target performance in inertial confinement fusion (ICF)[1] and is crucial in understanding many astrophysics phenomena.[2] In ICF, the target is driven either directly with laser beams (direct drive)[3] or indirectly by x rays, in which the laser drive is converted into x rays in a high-Z enclosure (hohlraum).[4] When laser light is incident on the target in a direct-drive configuration, the pressure created by the target ablation launches a shock wave that compresses the target. Any target modulations, either existing surface imperfections or modulations created by laser nonuniformities through laser imprinting, grow because of shock-driven Richtmyer–Meshkov (RM) instability as a shock wave propagates toward the rear surface of the target.[5–8] When the shock front reaches the rear surface of the target, it sends a rarefaction wave back toward the ablation surface; when it arrives, the target begins to accelerate. During the acceleration phase, the ablation-surface modulations grow exponentially because of Rayleigh–Taylor (RT) instability.[9–19] RT instability has been extensively studied in both ablative[12–19] and classical[9–11] (with no ablative stabilization) regimes. RT growth rates were studied in the linear regime of the instability with both direct[14–17] and indirect[12,13] drive. The highly nonlinear, turbulent regime of RT instability was studied mostly in the classical regime.[8–11] Weakly nonlinear features, such as harmonic generation and mode coupling to longer wavelengths, were measured in experiments using indirect drive[12,19] coupled to targets with preimposed, single-mode, and multimode initial perturbations. The saturation amplitudes of 3-D broadband nonuniformities were measured using laser-imprinted modulations as initial seeds for RT growth (conditions most relevant to direct-drive ICF).[18] In those experiments, the finite target thickness limited unstable hydrodynamic growth, which did not allow accurate measurements of the nonlinear velocities.[20] The experiments in this article present the first measurements of nonlinear saturation velocities, allowing a direct comparison with the Haan nonlinear-growth model[21] near saturation levels. The transition from linear to nonlinear growth of 3-D broadband modulations presented in this article is among the key factors required to understand nonlinear RT instability. This experimental study is critical to the success of ICF because most ICF ignition designs rely on the accuracy of Haan's predictions.

Experimental Details

In the experiments, initially smooth, 1-mm-diam, 20- and 50-μm-thick CH targets were driven with 12-ns square pulses at a laser intensity of ~5×10^{13} W/cm^2 on the OMEGA Laser System.[22] The modulation growth was measured with through-foil, x-ray radiography[20] using x rays from three different backlighters: an ~1.3-keV uranium backlighter for 20-μm-thick targets and an ~2.0-keV dysprosium and an ~2.5-keV tantalum for 50-μm-thick targets. Harder x rays were used at later times when target modulations reached larger amplitudes. The backlighter x rays were imaged by an 8-μm pinhole array onto a framing camera, allowing for up to eight images with a temporal resolution of ~80 ps and a spatial resolution of ~10 μm to be captured at different times in each shot.[20] The initial target modulations, used for RT growth measurements, were imprinted by laser-intensity nonuniformities of the imprint beam, which arrived ~200 ps before all other drive beams, used for target acceleration.[18,20] The process of laser imprinting takes ~200 ps. During this time, a plasma develops (from laser ablation) between the laser absorption (near the critical surface) and ablation surfaces, which decouples laser beams from the target, thereby stopping the imprinting process.[23,24] Two different initial target modulations were created by a laser beam with either a standard distributed phase plate[25] (SG8 DPP) or a laser beam with no DPP, defocused to an ~1-mm spot. Figure 103.19 shows measured central, 333-μm-sq parts of laser equivalent-target-plane images with an SG8 DPP [Fig. 103.19(a)] and with no DPP [Fig. 103.19(b)]. The laser-modulation Fourier spectra of these laser images are shown in Fig. 103.19(c). The beam with a DPP (solid curve) has broadband modulations with spatial frequencies up to ~320 mm^{-1}, corresponding to the smallest spatial size of ~3 μm and an intensity modulation σ_{rms} of ~94%. The beam with no DPP (dashed curve) has modulations with spatial frequencies up to ~50 mm^{-1}, corresponding to the smallest spatial size of ~20 μm, and an intensity modulation σ_{rms} of ~51%.

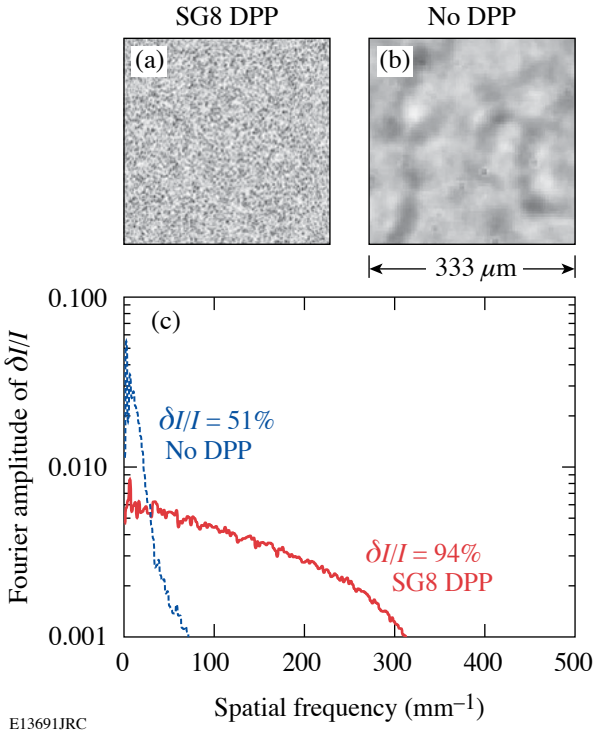

Figure 103.19
Central, 333-μm-sq parts of the measured equivalent-target-plane images of laser beams with (a) a regular SG8 DPP and (b) with no DPP used to produce initial 3-D broadband modulations for RT growth. (c) Fourier amplitudes of relative laser intensity as a function of a spatial frequency of these laser-beam images with a SG8 DPP (solid line) and with no DPP (dashed line).

Experimental Results

The optical-depth (OD) images (obtained by taking the natural logarithm of intensity-converted, framing-camera images) of x-ray radiographs are shown in Figs. 103.20(a), 103.20(b), and 103.20(c) for SG8 DPP initial conditions and in Figs. 103.20(d), 103.20(e), and 103.20(f) for no-DPP initial conditions. The early-time images (a) and (d) were obtained using a uranium backlighter, while later-time images (b) and (e) were obtained with a dysprosium backlighter and images (c) and (f) with a tantalum backlighter. A Weiner filter (based on measured system resolution and noise) was applied to these images to remove noise and deconvolve the system's modulation transfer function to recover target OD modulations.[20] The measured target OD variations are proportional to the variations of target areal density $\delta[\rho R]$, $\delta\left[\mathrm{OD}(t)\right] = \mu_{\mathrm{CH}}(E)\delta\left[\rho R(t)\right]$, where $\mu_{\mathrm{CH}}(E)$ is the CH target mass absorption rate at the x-ray energy E used for backlighting and t is the time of the measurement. The measured (in undriven targets) mass absorption rates were 950±100 cm^2/g, 320±30 cm^2/g, and 240±20 cm^2/g for uranium, dysprosium, and tantalum backlighters, respectively. The areal-density modulations were obtained by dividing measured OD modulations by the target mass absorption rates. Harder x rays were used to measure higher-amplitude modulations at late times because softer x rays are completely absorbed in large modulation spikes, compromising the measurements. Measurement timings of 20-μm-thick targets were converted to those of 50-μm-thick targets according to the calculated (by 1-D hydrocode *LILAC*[26]) target distance traveled.

During the acceleration phase, the target's laser-imprinted modulations grow because of RT instability. During this growth, the modulations shift to longer wavelengths, with initial small structures growing into large bubbles (the dark regions in x-ray radiographs shown in Fig. 103.20) and narrow spikes (light areas in the radiographs). Figure 103.21 shows the evolution of modulation areal-density Fourier amplitudes (for shots with DPP initial seeds). The dotted line is the Haan saturation level[20] $S_k = 2/Lk^2$, where $L = 333$ μm is the box size of the x-ray image, k is the spatial wave number of modulations, $k = 2\pi f$, and f is the spatial frequency. The saturation level S_k was converted to areal density by multiplying it by the *LILAC*-calculated foil density of ~1.7 g/cc, which was predicted to be constant (within about 10%) for the duration of the experiment. In the Haan model,[21] the spectral amplitudes grow exponentially with the RT growth rate $\gamma(k)$ until they reach the saturation levels S_k; at this point they grow

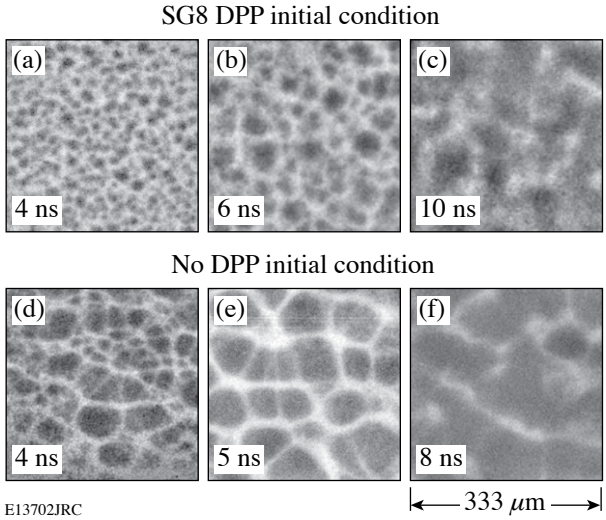

Figure 103.20
X-ray radiographs of the 3-D broadband modulations initially produced by the imprinting of the laser beam with a SG8 DPP and measured at 4, 6, and 10 ns [images (a), (b), and (c), respectively] and with the laser beam with no DPP and measured at 4, 5, and 8 ns [images (d), (e), and (f), respectively].

linearly in time with saturation velocities $V_s(k) = S_k\gamma(k)$. The RT growth rate is determined by the Betti–Goncharov dispersion relation[27] $\gamma(k) = 0.94\left[kg/(1 + kL_m)\right]^{0.5} - 1.5kV_a$, where $g = 10\ \mu$m/ns^2 is the target acceleration, $V_a = 0.65\ \mu$m/ns is the ablation velocity, and $L_m = 0.1\ \mu$m is the density scale length (all three parameters were calculated by *LILAC*). The shorter-wavelength modes grow most rapidly and quickly saturate at levels S_k while the longer-wavelength modes grow more slowly. As a result, the mid-wavelength modes have the largest growth factors, producing a peak in the spectrum. As the evolution continues, this peak moves to longer wavelengths, as shown in Fig. 103.21. Because the effects of finite target thickness, which compromised the evolution of the thin, 20-μm-thick targets in previous experiments,[20] were detected only after ~7 ns in the present experiments with 50-μm-thick targets, the analysis was limited to data taken up to ~6 ns.

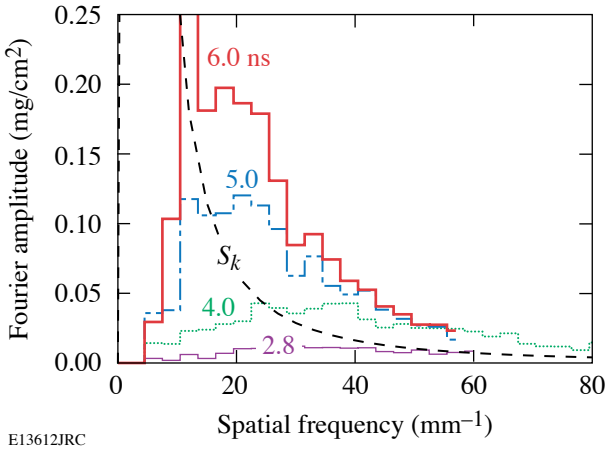

Figure 103.21
Fourier amplitudes of the target areal-density modulations as a function of spatial frequency initially produced by the imprinting of the laser beam with SG8 DPP and measured at 2.8 (thin solid), 4.0 (dotted), 5.0 (dotted-dashed), and 6.0 ns (thick solid curve). The dashed curve corresponds to the saturation amplitude predicted by Haan.[20]

Figure 103.22 shows the temporal evolution of the areal-density Fourier amplitudes at four spatial wavelengths of 20, 30, 60, and 120 μm for shots with DPP initial conditions. The amplitudes of the 120-μm spatial wavelength [see Fig. 103.22(a)] are below their saturation levels S_k. They are growing exponentially in the linear regime. The solid lines in Figs. 103.22(a) and 103.22(b) are the exponential fits to the data, from which the growth rate is determined. The amplitudes of the 60-μm-wavelength modulations [see Fig. 103.22(b)] undergo a transition from exponential growth to linear temporal growth. The solid lines represent the exponential fit to the data below the saturation level S_k, while the dashed lines represent the linear fit above the saturation level. The dotted lines in Figs. 103.22(c) and 103.22(d) are the linear fits to the 30- and 20-μm-wavelength data above their saturation levels. Similar fits were performed to the data with no DPP initial conditions. Figure 103.23 summarizes the growth results. The dashed line in Fig. 103.23(a) shows the growth rate $\gamma(k)$ (defined in the previous paragraph) as a function of spatial frequency. The diamonds correspond to the measured growth rates of 120- and 60-μm-wavelength modulations (corresponding to the spatial frequencies of 8 and 16 mm^{-1}, respectively) from all shots (with initial conditions including both SG8 DPP and no DPP). The dashed line in Fig. 103.23(b) shows the saturation velocity $V_s(k) = S_k\gamma(k)$ as a function of the spatial frequency, as defined by the Haan model.[21] The diamonds correspond to the measured saturation velocities of the 120-, 60-, 30-, and 20-μm-wavelength modulations (corresponding to spatial frequencies of 8, 16, 33, and 50 mm^{-1}, respectively). The measured saturation velocities are in excellent agreement with Haan-model[21] predictions. Once the modulations enter the nonlinear regime, the velocities no longer depend on initial conditions. The measured growth rates of long-wavelength modulations are higher (by about a factor of 2) than the Haan-model predictions (given by the Betti–Goncharov formula). Previous studies[28,29] have predicted enhanced growth (with respect to the Haan model) of long-wavelength modes in the classical RT instability (without

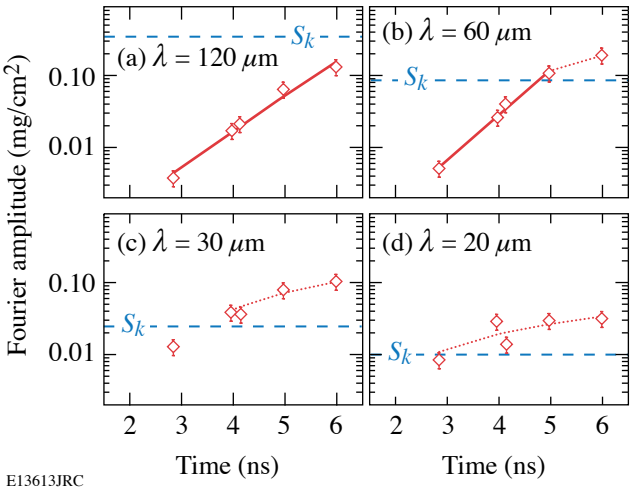

Figure 103.22
Temporal evolution of the target areal-density modulations measured at spatial wavelengths of 120, 60, 30, and 20 μm [(a), (b), (c), and (d), respectively]. The solid and dotted lines represent exponential and linear-in-time fits to the experimental data, respectively, initially produced by the imprinting of the laser beam with an SG8 DPP. The horizontal dashed lines show the saturation amplitudes predicted by Haan.[20]

ablation stabilization) because of enhanced mode-coupling of higher-amplitude, faster-growing, shorter-wavelength modes. The same studies,[28,29] however, predicted no significant contribution of mode coupling for the ablative RT growth (relevant to our experiments). A recent study[30] by Sanz *et al.* predicted enhanced mode coupling to longer-wavelength modes in the ablative RT instability, compared to the classical RT case. The present experiments are consistent with this new study[30] rather than with the previous predictions.[28,29] This correction to the Haan model has a small effect on the overall growth of the total rms modulation level because the longer wavelengths (120 μm and 60 μm) have smaller amplitudes than the shorter-wavelength modes (as shown in Fig. 103.21) and shorter modes grow with the velocities that are in agreement with Haan model. Therefore, the average modulation levels (rms amplitudes) grow very close to Haan-model predictions.[21] We find it remarkable that this simple model predicts so accurately such a complicated phenomenon as the nonlinear saturation of the RT instability.

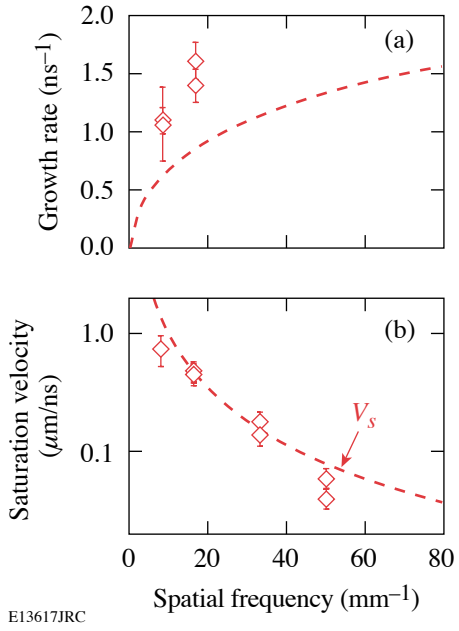

Figure 103.23
(a) Modulation RT growth rates as a function of spatial frequency measured (diamonds) and predicted by the Betti–Goncharov dispersion relation (dashed curve). (b) Modulation nonlinear saturation velocities as a function of spatial frequency measured (diamonds) and predicted by the Haan model (dashed curve).

Figure 103.24 shows the evolution of power spectra at three different times (with no DPP initial conditions). In the highly nonlinear, turbulent regime, it has been determined that the power spectra follow the "–5/3" Kolmogorov power-law scaling.[10] In the present experiments, the modulations undergo the transition from linear to nonlinear growth near the saturation levels. At a later time (~5.9 ns), a large part of the modulation spectrum is in the nonlinear regime, while modulations at 2.5 and 3.8 ns approach the saturation levels. The thin, solid line presents the power-law fit to the 5.9-ns data showing the power-law slope of ~ –2.1. This slope is steeper than Kolmogorov's slope of –5/3 = –1.67, shown by a dotted line. Once the modulations enter the highly nonlinear, turbulent regime of RT instability, the slope is expected to approach –5/3, as was shown in earlier classical RT experiments.[11]

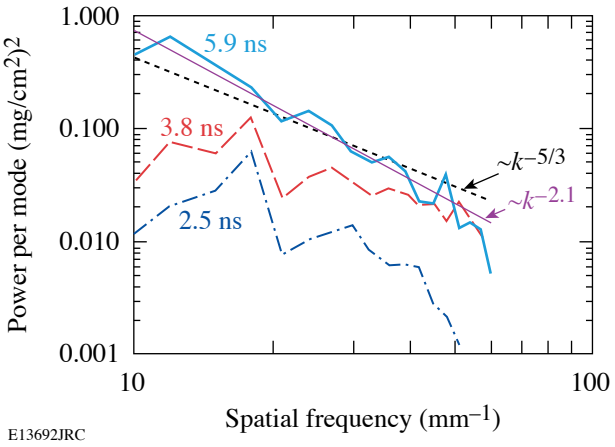

Figure 103.24
Measured power per mode of areal-density modulations at 2.5, 3.8, and 5.9 ns. The thin and dashed curves represent the lines with power-law slopes of –2.1 and –1.67 (or –5/3), respectively.

Conclusions

In conclusion, the unstable RT growth of 3-D broadband modulations was measured near nonlinear saturation levels in planar plastic targets directly accelerated by laser light. The nonlinear saturation velocities were measured for the first time and are in excellent agreement with the Haan model.[21] Once modulations enter the nonlinear regime, the measured growth does not depend on the initial modulation spectrum. The measured growth of low-amplitude, long-wavelength modes is consistent with the generation of enhanced nonlinear long wavelengths in ablatively driven targets, predicted[30] by Sanz *et al.* This experimental study is critical to the success of ICF because most ICF ignition designs rely on Haan's predictions.

ACKNOWLEDGMENT

The authors thank Prof. D. Shvarts, Prof. R. Betti, and Dr. B. A. Remington for helpful discussions. This work was supported by the U.S. Department of Energy Office of Inertial Confinement Fusion under Cooperative Agreement No. DE-FC52-92SF19460, the University of Rochester, and the New York State Energy Research and Development Authority. The support

of DOE does not constitute an endorsement by DOE of the views expressed in this article.

REFERENCES

1. J. Nuckolls *et al*., Nature **239**, 139 (1972).
2. B. A. Remington *et al*., Phys. Plasmas **4**, 1994 (1997).
3. S. E. Bodner, D. G. Colombant, J. H. Gardner, R. H. Lehmberg, S. P. Obenschain, L. Phillips, A. J. Schmitt, J. D. Sethian, R. L. McCrory, W. Seka, C. P. Verdon, J. P. Knauer, B. B. Afeyan, and H. T. Powell, Phys. Plasmas **5**, 1901 (1998).
4. J. D. Lindl, Phys. Plasmas **2**, 3933 (1995).
5. G. Dimonte and B. Remington, Phys. Rev. Lett. **70**, 1806 (1993).
6. Y. Aglitskiy *et al*., Phys. Plasmas **9**, 2264 (2002).
7. J. W. Jacobs and V. V. Krivets, Phys. Fluids **17**, 034105 (2005).
8. O. Sadot *et al*., Phys. Rev. Lett. **80**, 1654 (1998).
9. K. I. Read, Physica **12D**, 45 (1984).
10. M. B. Schneider, G. Dimonte, and B. Remington, Phys. Rev. Lett. **80**, 3507 (1998).
11. G. Dimonte *et al*., Phys. Fluids **16**, 1668 (2004).
12. B. A. Remington *et al*., Phys. Fluids B **5**, 2589 (1993).
13. K. S. Budil *et al*., Phys. Rev. Lett. **76**, 4536 (1996).
14. K. Shigemori *et al*., Phys. Rev. Lett. **78**, 250 (1997).
15. C. J. Pawley *et al*., Phys. Plasmas **4**, 1969 (1997).
16. J. P. Knauer, R. Betti, D. K. Bradley, T. R. Boehly, T. J. B. Collins, V. N. Goncharov, P. W. McKenty, D. D. Meyerhofer, V. A. Smalyuk, C. P. Verdon, S. G. Glendinning, D. H. Kalantar, and R. G. Watt, Phys. Plasmas **7**, 338 (2000).
17. T. Sakaiya *et al*., Phys. Rev. Lett. **88**, 145003 (2002).
18. V. A. Smalyuk, T. R. Boehly, D. K. Bradley, V. N. Goncharov, J. A. Delettrez, J. P. Knauer, D. D. Meyerhofer, D. Oron, and D. Shvarts, Phys. Rev. Lett. **81**, 5342 (1998).
19. M. M. Marinak *et al*., Phys. Rev. Lett. **80**, 4426 (1998).
20. V. A. Smalyuk, T. R. Boehly, D. K. Bradley, V. N. Goncharov, J. A. Delettrez, J. P. Knauer, D. D. Meyerhofer, D. Oron, D. Shvarts, Y. Srebro, and R. P. J. Town, Phys. Plasmas **6**, 4022 (1999).
21. S. W. Haan, Phys. Rev. A, Gen. Phys. **39**, 5812 (1989).
22. T. R. Boehly, D. L. Brown, R. S. Craxton, R. L. Keck, J. P. Knauer, J. H. Kelly, T. J. Kessler, S. A. Kumpan, S. J. Loucks, S. A. Letzring, F. J. Marshall, R. L. McCrory, S. F. B. Morse, W. Seka, J. M. Soures, and C. P. Verdon, Opt. Commun. **133**, 495 (1997).
23. S. E. Bodner, J. Fusion Energy **1**, 221 (1981).
24. V. N. Goncharov, S. Skupsky, T. R. Boehly, J. P. Knauer, P. McKenty, V. A. Smalyuk, R. P. J. Town, O. V. Gotchev, R. Betti, and D. D. Meyerhofer, Phys. Plasmas **7**, 2062 (2000).
25. Y. Lin, T. J. Kessler, and G. N. Lawrence, Opt. Lett. **20**, 764 (1995).
26. J. Delettrez, R. Epstein, M. C. Richardson, P. A. Jaanimagi, and B. L. Henke, Phys. Rev. A, Gen. Phys. **36**, 3926 (1987).
27. R. Betti, V. N. Goncharov, R. L. McCrory, and C. P. Verdon, Phys. Plasmas **5**, 1446 (1998).
28. S. W. Haan, Phys. Fluids B **3**, 2349 (1991).
29. D. Ofer, U. Alon, D. Shvarts, R. L. McCrory, and C. P. Verdon, Phys. Plasmas **3**, 3073 (1996).
30. J. Sanz, J. Ramírez, R. Ramis, R. Betti, and R. P. J. Town, Phys. Rev. Lett. **89**, 195002 (2002).

Technologies for Mitigating Tritium Releases to the Environment

Historical Background

The University of Rochester's Laboratory for Laser Energetics is preparing to fabricate and implode targets containing DT ice. To minimize risk to the environment and personnel, a tritium-handling infrastructure has been installed within the laboratory. The infrastructure strives to intercept tritium emissions from the process loops and to reduce emissions arising from contaminated surfaces.

Historically, in the 1950s through the late 1960s, tritium-handling systems were housed in air-ventilated enclosures. Room air was drawn over the equipment, directed to a stack, and discharged. Tritium that escaped through leaks in the plumbing, desorbed from contaminated internal surfaces exposed to air, or was collected by vacuum systems would be entrained in the airflow and directed to the stack. There was no effort to extract the tritium species from the effluent stream. This practice was attractive because it was the least costly to implement, offered flexibility during upgrades and maintenance, and imposed the least number of constraints during routine operations. The facilities needed to be remote from populated areas, however, because the emissions imposed a significant impact on the environment surrounding the plants. While this approach offered short-term relief from tritium releases, over the longer term, the environment surrounding the facilities became severely contaminated. As a consequence, contamination levels within the facilities gradually rose and chronic worker dose increased. By the time the United States Atomic Energy Commission issued a directive (in 1969) to all tritium facilities to reduce effluents to levels "as low as practical," most large-scale tritium-handling facilities had already started to implement containment technologies.

To be successful and economically viable, the trapping and removal technologies had to be installed as near the point of origin as possible before any excessive dilution with air had occurred. In most cases, gaseous effluents were converted to water and collected on molecular sieves. The system throughputs, which were determined to first order by the sizes of the oxidation reactors and the driers, varied from a few liters/h to 2000 liters/min (LPM).

In the mid to late 1970s, efforts to replace air in the containment boxes with inert gas were met with limited success. In this approach, tritium gas could be captured directly without conversion to tritium oxide by reacting with a titanium sponge. However, water vapor in the atmosphere would permeate into the boxes and passivate the sponge by forming an impenetrable oxide layer on the titanium. Systems containing fresh charges of titanium sponge would scavenge tritium from the inert gas for brief periods, but the performance would gradually degrade as the thickness of the oxide coating grew on the titanium. As a result, cleanup systems that collected tritium gas directly were reserved for special applications in which large quantities of tritium gas were at risk and needed to be recovered without conversion to tritium oxide. More common, however, containment systems using either air or inert gas relied on the oxidation of all tritium species and the collection of the tritiated water vapor with driers. Periodically, the driers could be regenerated to recover their effectiveness. The highly active condensate would be solidified and land disposed. In effect, tritium discharges that would have contaminated the environment around a processing facility were collected on disposable beds and stored at burial sites in leak-tight containers.

The advent of new alloys comprising a mixture of iron and zirconium (Zr-Fe) dramatically broadened the options for tritium effluent treatment.[1] The Zr-Fe alloy offered stability against passivation when exposed to impurity fluxes far superior to that demonstrated by titanium sponge and, simultaneously, offered the potential for recovering the captured tritium gas.[2] Facilities that handled significant quantities of gas could recover and re-use tritium originally destined for the stack, and, as such, recoup some of their investment in the tritium while simultaneously reducing the cost of land-disposing solidified tritiated effluent. In the 1980s and 1990s, this alloy found utility not only in glovebox applications, but also in treating vacuum effluents.[3] The acceptance of the alloy as a tritium-capture

device has spread across the tritium community over the past two decades.[4]

Currently, an array of devices including Zr-Fe scavenger beds,[5] uranium scavenger beds,[6] molecular sieve driers, and nickel catalyst beds[7] offers the potential to treat both inert gas and air streams.[8] Both glovebox atmospheres and vacuum effluent streams can be processed. These systems can be scaled over a broad range of throughputs and capacities, but, nevertheless, economic drivers continue to favor tritium recovery before any significant dilution with air occurs.[9,10]

By the mid-1970s, tritium became the dominant isotope for the radioluminescent industry, replacing both radium-226 and strontium-90. Tritium was viewed as radiologically safer and more environmentally acceptable by comparison to the other two isotopes. The industry appeared to be on the threshold of an unprecedented expansion with self-powered backlighting for digital watches leading a host of other ubiquitous applications. However, this optimistic growth was quickly tempered. The general tightening of environmental and safety regulations being applied to the nuclear industry spread to the radioluminescent industry. In part, this movement was driven by the Three Mile Island accident and the discovery of small amounts of tritium in a public school food-preparation facility across the street from a tritium light-manufacturing plant in Tucson, Arizona. By the 1980s the industry had stabilized, focusing on applications where absolute reliability was needed, such as in hospitals, mines, multilevel buildings, and aircraft exit markings. A number of military applications in which the benefit clearly outweighed the perceived risk have been identified and exploited.

Just as the optimism in the radioluminescent industry abated, fusion fuel needs for the magnetic confinement program spawned an intense, worldwide effort to identify materials suitable for tritium handling, techniques to purify and measure tritium, and technologies to extract tritium from effluent streams. Significant advances were made in tritium-handling systems during the 1980s and 1990s.

This article reviews the technologies that minimize tritium releases from systems and discusses the strengths and weaknesses of those options. To this end, the components and systems that apply are reviewed, the optimal applications for those components and systems are identified, and their applicability to air and inert gas streams discussed.

The section entitled **Guiding Principles** (p. 143) reviews the guiding principles to consider when designing and operating process and capture systems. Ignoring these principles could convert the capture equipment into emission sources. In **Options for Tritium Capture** (p. 144), capture options for both air-bearing and inert carrier streams are presented. Component selection and the rationale for selecting the order of the components are also discussed. **Typical Tritium-Capture Schemes** (p. 146) provides examples to illustrate the application of the guiding principles. **Description of Components Used for Tritium Capture** (p. 148) provides the salient performance features of the components discussed in the previous sections. Component throughputs are discussed in **Throughput and Construction Guidelines** (p. 153).

Guiding Principles

Several principles apply to the effective handling and capture of tritium. These include

- understanding the global requirement for tritium trapping,
- defense in depth,
- interception close to the emission source,
- circulation,
- tailoring the capture system to the application,
- monitoring all effluent streams, and
- minimizing process volumes.

Each of these principles is discussed in the following paragraphs.

Many of the devices discussed in this article have demonstrated long-term effectiveness in mitigating tritium releases. However, these devices do not represent "magic bullets." Their effectiveness depends heavily on the manner in which they are implemented and integrated into the process loops. To simply view these devices solely as "bolt-on" components will severely restrict their utility, reduce their effectiveness, or, in some cases, increase the potential for significant tritium releases. A holistic approach to trapping and containment is required. Careful evaluation of the intended application, the operating regime, and the composition of the effluent is required if the trapping and containment of the tritium in the effluent is to be effective and robust.

The defense-in-depth concept provides robustness. Layering trapping technologies provide the opportunity for staged tritium recovery. Should the first barrier fail or perform below

design expectations, the second barrier can reduce the impact of the impending release.

Intercepting tritium emissions as close to their sources as possible continues to be the preferred option. The approach holds several advantages.

- The scale of the equipment and, consequently, its cost can be greatly reduced.
- Emissions in one subsystem do not impact the operation of other subsystems.
- Equipment can be tailored with greater precision to address specific potential release scenarios.
- Component selection options increase significantly if trapping occurs before mixing with air.
- The degree of secondary contamination is usually greatly reduced.

Circulating systems are preferred over once-through systems. These systems provide more time to process tritiated effluent, increase the effective decontamination factor (DF) through the use of multiple passes, and permit monitoring of the efficiency of the trapping process. Operators can increase the processing time should the treated-gas activity remain unacceptably high. Additionally, they can temporarily stop the process to repair a defective component and then continue the treatment before releasing the gas to the environment.

Trapping and removal technology is most effective when designed for specific tasks. Additionally, technology effectiveness is enhanced when coupled with certain operating techniques. For example, lines and equipment should be evacuated repeatedly or flushed with inert gas or air and the effluent directed to the trapping system before proceeding with any dismantling. If feasible, air flushes should follow inert gas flushes to encourage the release of loosely bound tritium. Work should proceed in environments that are drier than the flush gas to minimize the moisture-stimulated release of tritium from surfaces. Plastic tents or temporary enclosures should be built around the equipment that will be maintained. The atmosphere from the tents or enclosures should be purged through the trapping system. Where routine maintenance is expected, separate maintenance gloveboxes with supporting trapping technology should be used to dismantle and decontaminate equipment. Materials, such as elastomeric O rings, have a high solubility for tritium and will release large quantities of tritium when removed from service. These items should be stored in small purged containers until they are packaged for land disposal. Effluent from these containers may contain sufficient tritium to collect with trapping technologies.

All process exhausts should be monitored and, if necessary, treated before release to the stack. Typically, process exhausts represent the highest activity streams and make up the majority of the tritium chronically vented to the stack. The need for redundant isolation valves, or combinations of valves that are actuated by inline tritium monitors, should be reviewed. Where the potential for release is high, automated isolation valves should be installed.

Process loop volumes should be minimized, particularly in regions where tritium gas is susceptible to accidental release. Similarly, loop volumes that require frequent dismantling should be minimized. To achieve this, microwelding is preferred to demountable fittings; smaller-diameter tubing is preferred over 1/2-in. tubing; and 1/4-in. bellows sealed valves are preferred over 1/2-in. valves. The use of close-fitted enclosures over vulnerable components is preferred over the use of larger, more conventional gloveboxes to reduce the amount of atmosphere that need to be processed. Such designs, in turn, reduce the scale of the trapping technology required. In high specific activity applications, inert gas is preferred over air as a purge gas. Tritium gas can be captured without conversion to oxide and recovered for re-use.

Options for Tritium Capture

The tritium-capture technologies available for scrubbing tritium from gaseous effluents fall into two categories: (1) those used to treat air or inert gas containing air, and (2) those used to treat inert gas streams. The devices used to process these gaseous effluent streams and their relative placement in the treatment train are illustrated in Figs. 103.25 and 103.26.

1. Air Detritiation

Elemental tritium can be readily converted to oxide with hot copper oxide (CuO), Hopcalite,[(a)] or a precious metal catalyst (Pd, Pt, etc.). Tritiated organic vapors are more difficult to oxidize than elemental tritium. CuO reactors need to operate at 750°C to promote hydrocarbon oxidation efficiencies greater than 50% with a gas residence time[(b)] in the reactor exceeding 2 s. Hopcalite should be operated at 700°C to achieve complete oxidation of hydrocarbons at similar residence times. Palladium catalysts are more effective and achieve complete oxidation at 400°C. Occasionally, combinations of catalysts are used in the

[(a)] Hopcalite is a commercially available mixture of MnO_2 and CuO.

[(b)] Gas residence time is the time required for a slug of gas to transverse the hot region of a reactor.

same oxidation system to ensure complete oxidation of tritiated hydrocarbon species. Additionally, the efficiency of oxidation decreases as the absolute concentration of hydrogen decreases. Hydrogen (protium) can be added in low concentrations to the effluent stream to raise the total hydrogen content in the stream and improve the oxidation efficiency.

In low-humidity applications and at low flow rates, the stream containing elemental tritium that has been oxidized to tritiated water (HTO)[c] enters the drier directly. The gas temperature leaving the oxidizer has sufficient time to return to room temperature. As the flow rate increases, however, the oxidizer effluent must be cooled with an air-to-air heat exchanger to prevent heating the molecular sieve above room temperature. Drier capacity and performance degrades with increasing temperature. In high-humidity applications, a condenser should be used to remove the bulk of the water vapor before directing the effluent stream to the drier. Drier capacity and performance also degrades with increasing water content in the drier.

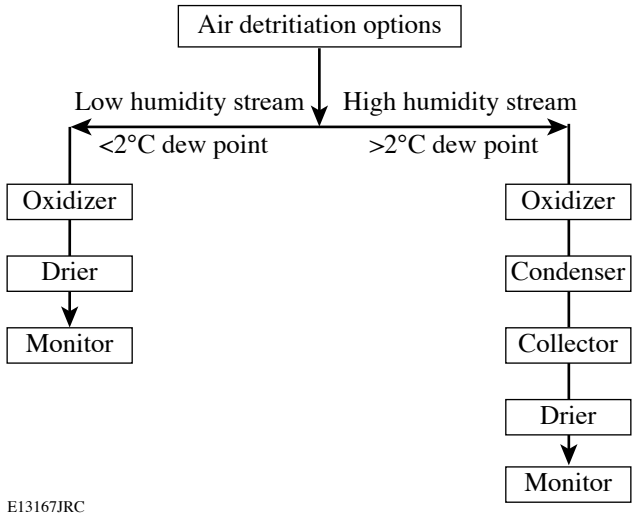

Figure 103.25
Devices used in air detritiation schemes.

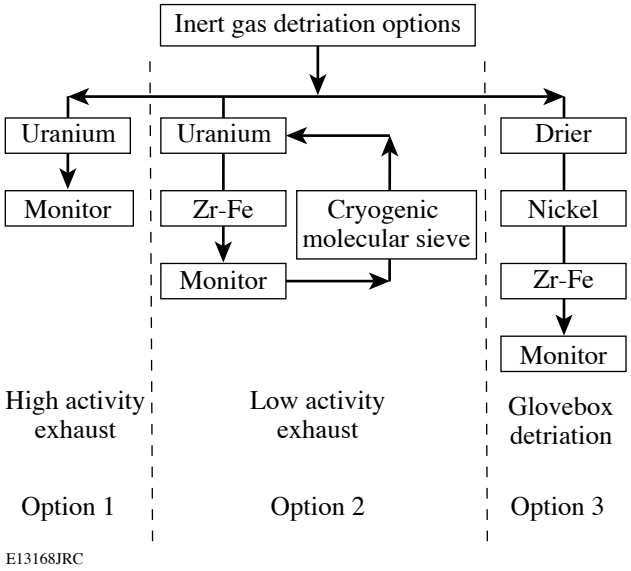

Figure 103.26
Inert gas detritiation options depend on the target activity of the effluent and the intended application.

Driers adsorb[d] tritiated water vapor on the molecular sieve. Approximately 7% water by weight can be loaded on the driers[e] before HTO breakthrough is observed. Dual-column drier systems permit continuous operation; while one drier is in service, the second can be regenerated.[f] Purging the drier during regeneration in the flow direction opposite to that used during the normal operation improves the performance of the drier because the exit end of the drier is never exposed to the high concentrations of HTO that are present at the drier inlet. Smaller systems may use a disposable drying column to eliminate the need for regeneration and packaging the desorbed water for land disposal. These driers can be outfitted with high-integrity, quick-disconnect fittings to minimize effluent releases during replacement.

The detritiation schemes for the high- and low-humidity effluent streams are illustrated in Fig. 103.25. A dew point of 2°C typically distinguishes the boundary between the two humidity regimes. When the water vapor concentration in the effluent exceeds 2°C (of the order of 0.7% water content by volume in the carrier), water can be condensed out of the effluent stream on a chilled surface and collected in a tank. The attractiveness of the condensation step increases as the humidity in the effluent increases because the drier operating time between regenerations can be optimized by capping the dew point of the effluent entering the drier at or near 2°C.

[c] In this document, tritiated water implies a mixture of H_2O and HTO. In HTO, one proton has been replaced with a triton.

[d] **Ad**sorption is a physical process by which water molecules bond to the surface of the molecular sieve without decomposing. During **ab**sorption, molecules decompose into their constituents and are incorporated into the bulk of the sorbing material.

[e] A drier containing 5 kg of molecular sieve will collect approximately 350 ml of water before any tritiated water is observed at the outlet of the drier.

[f] Regeneration is the process of removing adsorbed water by heating the molecular sieve and purging the drier with a very dry stream until the humidity of the purge gas at the drier exhaust drops below a target value, typically of the order of –80°C.

2. Inert Gas Detritiation

The options for detritiating inert gas streams are shown in Fig. 103.26. These options rely on the ability of elemental tritium to bind chemically with preactivated metal powder. The tritium concentration leaving one of these hydride-forming materials depends on the metal. In general, uranium finds utility within circulating process loops where exhaust concentrations up to 10 mCi/m^3 can be tolerated. Zr-Fe alloy, on the other hand, is more suited to polishing effluent streams and has the ability to reduce effluent concentrations below ~50 μCi/m^3.

Streams containing less than a few tens of parts per million (ppm) water vapor and/or organic species can be processed directly via option 1 or 2 without the need to dry or precondition the streams. Uranium will crack the incoming water vapor and modest quantities of hydrocarbons to form a uranium hydride/tritide, uranium oxides, and uranium carbides. The hydrogen can be released from the uranium metal thermally. However, the uranium oxide and carbides become irreversibly bound to the metal and represent a loss of hydrogen storage capacity and, ultimately, a reduction in the decontamination factor.[g] Water vapor will also react readily with the Zr-Fe alloy to form oxides. Hydrocarbons, however, tend to pass through the Zr-Fe alloy without reacting,[8] unless gas residence times exceed 10 s.

As the impurity content increases above a few ppm in the effluent stream, the oxides are more likely to passivate the reactive metal, making it incapable of capturing elemental hydrogen. In such cases, a nickel catalyst can be introduced upstream of the uranium and/or Zr-Fe beds to crack the hydrocarbons and the water vapor to form nickel carbides and oxides, respectively.[7] The hydrogen/tritium produced by the decomposition of the hydrocarbons or the water vapor passes through the nickel bed and is collected by the Zr-Fe alloy. Streams with larger water vapor loads, such as glovebox atmospheres, may require driers upstream of the nickel catalyst to remove the majority of the water first. In these applications, the nickel bed polishes the discharge from the drier to further decrease the stream humidity and reduces the load on the downstream hydrogen getter.

A cryogenic molecular sieve bed[h] can be added to the uranium/Zr-Fe circuit to facilitate *in-situ* regeneration of the Zr-Fe alloy. The regeneration entails transferring the tritium inventory from the Zr-Fe alloy to the cryogenic molecular sieve bed in a closed-loop operation and subsequently releasing the gas from the molecular sieve bed as a slug to the uranium. The intermediate step of transferring to the cryogenic molecular sieve bed is required to increase the elemental tritium partial pressure so that the uranium can absorb the gas.

Finally, the selection of one technological approach to trapping over another requires a considered evaluation by the end user, taking into account economic factors, intended end goals, and application. Although trapping technology for air applications tends to be somewhat more robust in that it is less likely to release its tritium inventory and less likely to be irreversibly damaged, that technology requires a significant investment in ancillary infrastructure if the tritium is to be reclaimed for re-use. Additional process loops are required to regenerate the drier and to collect and handle highly active water for either land disposal or for tritium recovery. In the latter case, the water must be decomposed in an electrolysis facility and the hydrogen transferred to an isotopic separation station for enrichment. On the other hand, metal beds are restricted to operate in inert gas streams. They can be destroyed with an unintentional ingress of air and release the entire resident tritium inventory during the accident. However, these metal beds capture elemental tritium directly and permit easy recovery of the gas for re-use. Metal beds avoid all issues related to water handling. Tritium enrichment, if required, can proceed directly after unloading the metal beds. In general, direct gas-capture systems are preferred over oxidation approaches in applications that

- require the recovery and re-use of elemental gas or
- lead to the production of high (>10 Ci/liter) specific activity water.

Direct gas-capture approaches can reduce gaseous emissions while simultaneously reducing the production of tritiated solid wastes that must be land disposed. Direct inert gas-capturing approaches simplify tritium recycling because these approaches eliminate the need to convert tritiated water to elemental hydrogen.

Typical Tritium-Capture Schemes

A configuration commonly used to reduce emissions from process loops is illustrated in Fig. 103.27. In this example, the tritium recovery subsystem comprising a tank, monitor, scavenger bed (or a train of scavenger beds if the makeup of the effluent dictates a more aggressive treatment), and isolation valves is installed between the process loop and the dry vacuum

[g] The decontamination factor is the ratio formed by dividing the inlet activity concentration by the outlet activity concentration.

[h] Elemental tritium can be adsorbed on a molecular sieve at 77 K (–196°C), provided all traces of water vapor are removed from the surface of the molecular sieve.

pump.[(i)] Instead of evacuating the process loop directly to stack or via a single scavenger bed in a once-through operation, the contents of the process loop are expanded into the pre-evacuated tank for treatment. The process loop is then isolated from the tritium recovery system. Helium gas pressurizes the tritium recovery system to raise the system pressure to one atmosphere. The contents of the expansion tank are circulated through the scavenger bed and the progress of detritiating the stream is monitored with an inline tritium process monitor. At a prescribed concentration, the contents of the subsystem are then evacuated to the stack, or flushed from the subsystem with clean helium and the tank subsequently evacuated in preparation for the next operating cycle. Purging the lines with helium is recommended because the inert gas flush reduces the potential of residual tritium lingering in the plumbing between the tritium recovery system and the stack. An accumulation in this plumbing can unexpectedly trip alarms during subsequent operations and mask the actual cause of the emission.

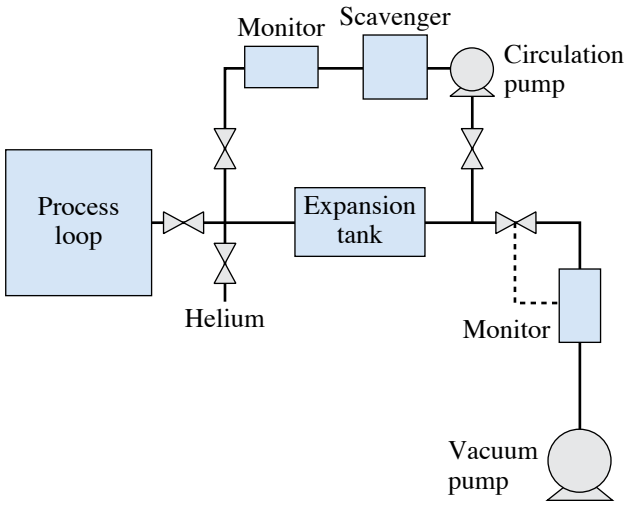

Figure 103.27
Incorporation of a simple cleanup subsystem into the exhaust of a process loop.

The second in-line tritium monitor between the vacuum pump and the treatment system is electronically coupled to the valve just upstream of the monitor. It automatically actuates the valve should the effluent activity exceed a predetermined level. Once the process loop has been isolated from the stack, an operator can intervene to rectify the fault, review the need for continued processing and, when ready, release the treated effluent to the stack. In effect, this monitor buys the operator time to make an informed decision.

Outgassing from tritiated components and tritium leaks from components represent common emission sources. Figure 103.28 illustrates an approach to capture the escaping tritium. This assembly comprises a container, a tritium scavenger bed, two in-line tritium monitors, a mass flow meter, a circulating pump, and a helium purge line. In this example, the leaky component is stored in the container. Tritium monitors track the effectiveness of the scavenger to capture the tritium. A low-throughput pump is ideal for this application. Although not shown, a nickel catalyst can be installed upstream of the Zr-Fe scavenger bed to protect the alloy from the trace water and modest amounts of air ingress. The nickel bed dramatically extends the life expectancy of the Zr-Fe alloy.

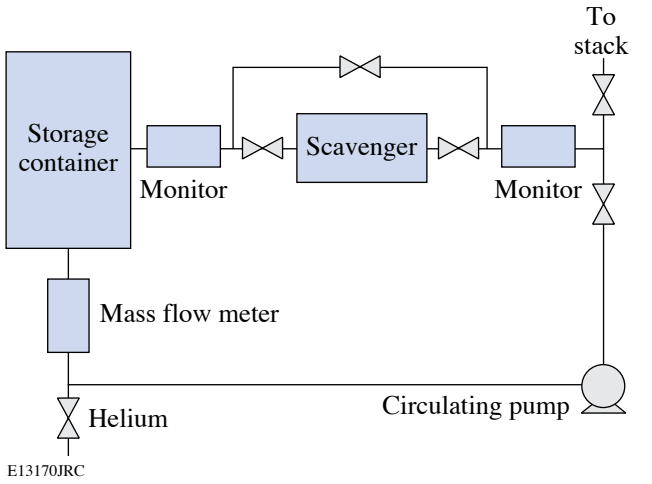

Figure 103.28
Tritium reclamation subsystem for leaky components.

A typical scheme for capturing tritium from an air stream is illustrated in Fig. 103.29. This subsystem comprises an oxidizer, an air-to-air heat exchanger, a drier, and an in-line tritium monitor. Elemental tritium entrained in the stream is converted to oxide and collected in the drier. Although air can be used as a purge gas, it should be predried to reduce the inactive water load delivered to the drier and extend the operating time between regenerations. Drying the air purge also reduces the isotopic dilution of the tritiated water should tritium recovery for re-use be planned.

This configuration can be readily modified to accommodate the high-humidity (HH) streams described in Fig. 103.25 by

[(i)] Dry vacuum pump development in recent years has permitted the replacement of mechanical oil vacuum pumps. Pump characteristics of these dry pumps rival those attainable with oil pumps without the attendant problems of handling and containing tritiated oil.

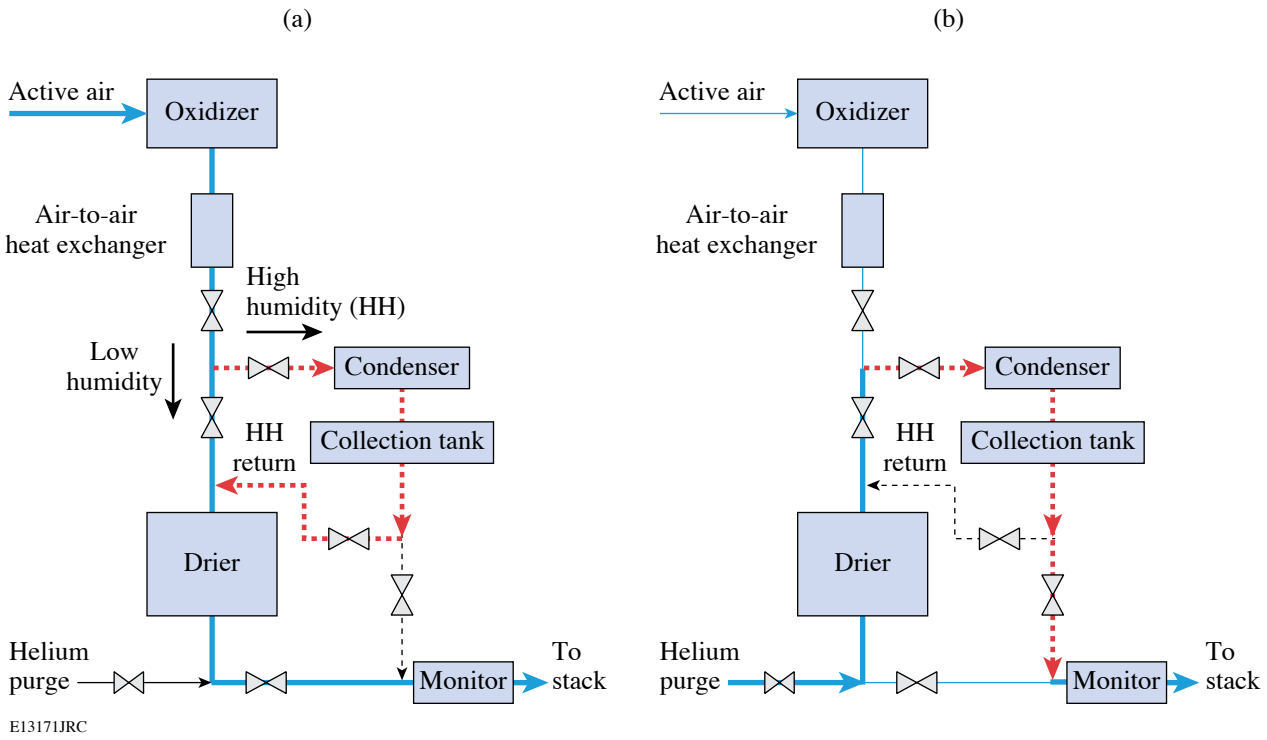

Figure 103.29
Simple air detritiation subsystem.

plumbing the system so that a condenser is used for both precipitating water vapor from the effluent stream [as shown in Fig. 103.29(a)] and for *in-situ* regeneration.

During regeneration, the helium[(j)] purge would enter the exhaust end of the drier and flow through the condenser and the collection tank to the stack, as shown in Fig. 103.29(b).[(k)] A second (polishing) drier could be installed downstream of the collection tank (not shown in the figure) to suppress any emissions from regeneration. System designers have the option of operating the regeneration circuit in the "once-through" mode, as shown in Fig. 103.29, or in a circulation mode by redirecting the helium flow back to the drier being regenerated.

The condensate can easily exceed several Ci/liter and requires caution when handling. The condensate can be immobilized for land disposal or packaged for shipment to a facility for tritium recovery.

[(j)]Nitrogen or dry air can replace helium as a purge gas in this application.
[(k)]The regenerating gas flow should be counter to the normal direction of operation so that HTO buildup near the driver exhaust is prevented.

Description of the Components used for Tritium Capture

Devices used for extracting tritium from flowing gas streams and their general integration in process loops have been described in the previous sections. This section discusses the strengths and weaknesses of the devices.

1. Uranium Scavenger Beds

Depleted uranium has a long-standing history in tritium service. This metal is used to store tritium, transport tritium gas, and, in special applications, selectively remove tritium from flowing gas streams. Designs that provide access into the uranium via a single line are the safest. They prevent the uranium from releasing its tritium inventory, even when accidentally exposed to air.[11,12] Additionally, only a fraction of the uranium will be oxidized during the air ingress. However, helium-3 produced by tritium decay will interfere with the ability of uranium to store tritium. "Flow-through" designs are commonly used in process loops to mitigate the "helium-blanketing" effect even though these designs pose an greater risk to releasing tritium during an accidental air ingress.

Uranium offers a very high storage capacity; 120 standard cubic centimeters (scc) of gas per gram of uranium can be

easily accommodated without compromising the reaction kinetics.[13–15] It is well-suited to removing tritium from clean inert gas streams containing high tritium concentrations and offers uniform reaction kinetics over a very broad range of tritium-to-uranium (T/U) atom ratios.[16] It is possible to charge uranium with tritium up to an atom ratio of nearly three tritium atoms per uranium atom although the operating range is usually restricted to a ratio of 1.5 so that sufficient tritium storage capacity remains for unforeseen events.

Tritium gas reacts with the uranium to form a uranium tritide. This chemical compound is stable at room temperature. Heating the uranium tritide will release the tritium as a gas. The reaction is fully reversible. The pressure-composition isotherms for the uranium–tritium system are very simple.[17] In the range of primary interest, i.e., at operating pressures below approximately 1.5 atm and at temperatures between 20°C and 450°C, the initiation of the tritide phase begins at T/U ~ 0.1 and is complete at T/U ~ 2.93. The plateau region between these two extremes is essentially flat. As a result, the temperature of the uranium tritide uniquely specifies the tritium gas pressure above the uranium powder. At 430°C, for example, the tritium gas pressure over uranium powder will be 1 atm. Caution is required when increasing the temperature much beyond 425°C; the pressure increases rapidly and can overpressurize the device containing the uranium. The equation

$$P = 10^{(-4590/T + 9.39)} \quad \text{(Torr)} \tag{1}$$

prescribes the pressure over the temperature range of 150°C to 600°C. In this equation, the pressure (P) is in Torr and the temperature (T) is in Kelvin.

The reaction rate to form tritide is dramatically enhanced by preconditioning the uranium. The uranium metal is charged to capacity with hydrogen gas to form UH_3 and subsequently unloaded by heating the UH_3 to 425°C in a vacuum. The hydrogen loading/unloading cycle should be repeated seven times to break down the uranium metal to its optimum size. This process, known as decrepitation, increases the surface area of the uranium by breaking down the bulk uranium metal into a fine powder with a particle distribution in the range of 0.1 to 10 μm. Following the last unloading, any residual hydrogen can be removed from the uranium by repeating the loading/unloading one additional time using isotopically downgraded tritium.

Uranium scavenger beds differ from storage devices in three ways. First, they require the carrier stream to flow through the container. Second, they operate at T/U ratios below 1 to enhance the detritiation factor (DF). Third, they are typically constructed from larger diameter containers to reduce the carrier molar flux(1) in the container. The equation[18]

$$G^{1/2}\log(\mathrm{DF}) = 0.019 - 0.006\ (\mathrm{T/U}) \tag{2}$$

relates the DF to the T/U for T/U ratios up to 2.5 and carrier molar fluxes (G) up to 2.5 mol/m^2/s. This equation assumes an impurity-free carrier and a uranium operating temperature of 22°C.

Two conditions can deteriorate the performance of these devices. Impurities will coat the uranium powder surface and reduce the amount of uranium available for removing tritium from the carrier. Secondly, increasing the uranium temperature will increase the tritium partial pressure over the uranium and lower the DF.

Figure 103.30 illustrates the lowest tritium concentration attainable over uranium as a function of temperature. Inspection of this figure is instructive for two reasons: it demonstrates how rapidly the DF will deteriorate with increasing temperature, and it illustrates that the lowest attainable tritium concentration in a carrier stream possible at room temperature with a uranium scavenger bed will be in the 10 mCi/m^3 range.

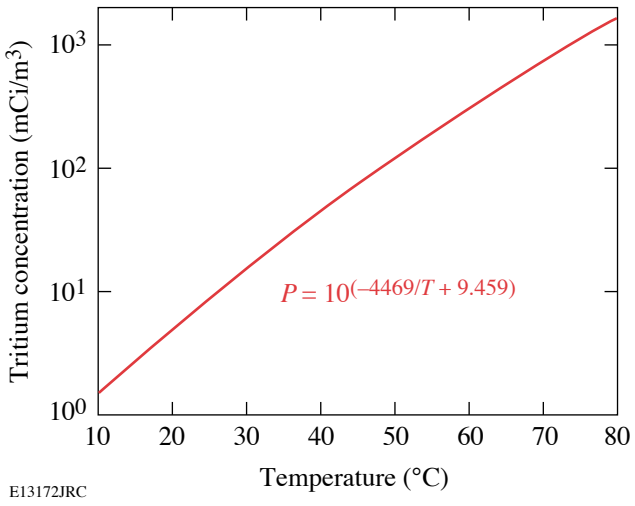

Figure 103.30
Tritium concentration dependence on uranium powder temperature.

(1)The molar flux of the carrier is the number of moles of carrier flow per unit time and per unit cross sectional area of container perpendicular to the flow direction. It is usually expressed as mol/m^2/s.

Increasing the uranium temperature twofold, from 20°C to 40°C, decreases the DF tenfold. Operating a uranium scavenger bed at 25°C precludes reducing the tritium activity of a carrier below 10 mCi/m^3.

Unconfined uranium powder oxidizes spontaneously when exposed to air. Undoubtedly, the term "pyrophors," used in the radioluminescent industry when referring to uranium storage beds, reflects some historic incident related to the propensity of the powder to ignite. Confined uranium powder, however, has a limited reaction with air, particularly if the container uses a low-porosity stainless steel filter to prevent uranium powder from migrating out of the device. In general, these devices will lose approximately 30% of their storage capacity and will not release their tritium inventory during an air ingress accident. Uranium tritide is the most secure tritium storage vehicle available to the tritium community, including any accident scenario involving air ingress not involving a flow-through configuration, i.e., a construction that permits air to enter via one port only and then becomes "dead-headed."

Flow-through devices, both for storage and scavenging applications, are used to preclude helium blanketing. Blanketing occurs when decay-helium interferes with the bulk flow of tritium gas to the uranium powder. During blanketing, the rate of gas transfer from a vessel to the uranium powder stalls before all the tritium has had an opportunity to transform into a tritide. The balance of the tritium in the process system volume, however, can be captured on the uranium powder by circulating the remaining gas over the powder to dislodge the helium cover. Any air ingress during circulation will completely and rapidly oxidize and nitride the uranium with a concomitant release of the entire resident tritium inventory to the carrier downstream of the device. Flow-through operations represent the single most likely action that can precipitate a significant tritium release. Extreme care must be exercised during flow-through operations. Housing the process equipment in an inert environment is a very effective way of preventing the accidental ingress of air during circulation.

2. Zr-Fe Scavenger Beds

A Zr-Fe alloy developed by SAES Getters under the trade name ST198 can also be used to scavenge tritium from gas streams.[1] The alloy can be used in conjunction with noble gas carriers and nitrogen gas streams, albeit there is a gradual loss of capacity with time as the elements of the alloy nitride.[5] As with uranium metal, the alloy spontaneously forms a tritide when exposed to elemental tritium; the reaction is reversible. The alloy must be heated to 550°C for the tritium recovery and has a moderate storage capacity for tritium, typically of the order of 0.8 scc of gas per gram of alloy.

The nominal operating temperature for ST198 is 350°C. Decreasing the operating temperature increases the storage capacity for tritium gas. Decreasing the operating temperature also decreases the tritium partial pressure over the alloy, thereby improving the DF. However, the reaction kinetics and the tolerance of the alloy to any impurities entrained in the carrier also decrease with decreasing temperature. Additionally, the modest ability of the alloy to crack organic volatile species decreases. Operating above 300°C strikes a reasonable balance between the various competing factors. At 350°C, excellent tritium scavenging properties are exhibited by ST198 in noble gas streams, provided the gas residence time in the reactor exceeds 3 s.

Scavenging tritium from a nitrogen environment requires special attention. The alloy exhibits good scavenging properties in nitrogen at 350°C. The reaction kinetics between the alloy and nitrogen are slow at this temperature; however, the rate of nitriding increases noticeably at alloy temperatures above 400°C. The alloy is unusable at 500°C in the presence of nitrogen. Operating conditions that momentarily spike the alloy above 500°C can lead to a runaway nitriding condition. The alloy will react vigorously with the nitrogen cover gas to release approximately 600 kJ per mole of gas consumed. This energy will heat the alloy to very high temperatures and desorb the entire tritium inventory from the alloy. For example, a sudden ingress of 20-scc air into the nitrogen carrier stream could precipitate such a runaway condition unless the alloy temperature is monitored and the flow stopped whenever the alloy temperature exceeds 400°C in nitrogen. Nitriding ST198 is irreversible and will decrease the capacity of the bed.

The pressure-composition isotherm for the Zr-Fe alloy/hydrogen system is considerably more complex than the uranium/hydrogen system. A single tritide phase does not exist for the Zr-Fe alloy/hydrogen system. The elemental gas pressure over the alloy depends on both the resident tritium inventory of the alloy and the operating alloy temperature. The relationship between tritium pressure P in Torr, the resident inventory Q in Torr-liters/g, and the alloy temperature T in Kelvin is given by the equation

$$P = Q^2 * 10^{\left(-6220/T + 5.03\right)}. \quad (3)$$

Inspection of Fig. 103.31 reveals that operating at 350°C will reduce the activity of a carrier below 20 μCi/m^3, provided

the resident inventory remains below approximately 100 mCi/g of alloy. In practice, this target is difficult to attain except for the first few operating cycles of the alloy. Typically, this alloy is used to reduce carrier stream activities below 400 to 500 μCi/m^3, suggesting that the resident inventory of the ZrFe reaches approximately 500 mCi/g.

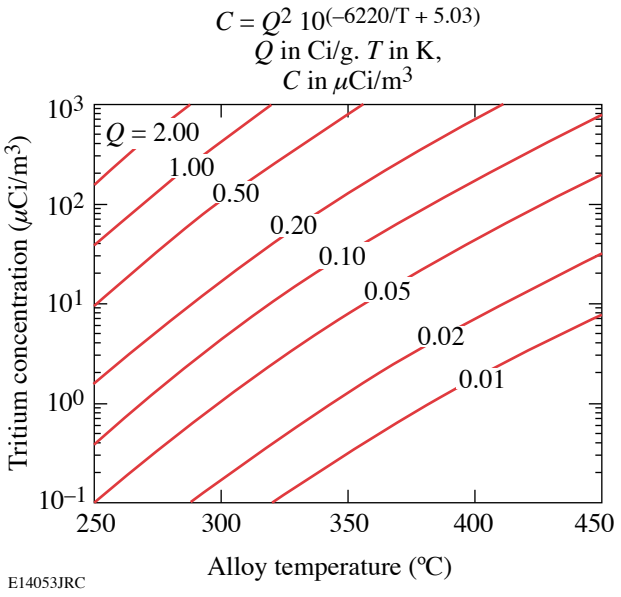

Figure 103.31
Tritium concentration dependence on resident inventory and ST198 alloy temperature.

The alloy is suitable for treating effluent streams that will be discharged to the stack. Examples include treating effluents evacuated from process loops, polishing effluent streams that have passed through uranium scavenger beds, and tritium recovery from gloveboxes using nitrogen or helium cover gases.

Impurities are decomposed at the alloy surface to form tritides, hydrides, oxides, and carbides. The latter two compounds represent an irreversible chemical reaction with the alloy that reduces its capacity for tritium storage. If the impurity flux to the alloy exceeds the impurity-clearing rate[(m)] from the alloy surface, the scavenging performance of the alloy will degrade with time. To recover the tritium-capture efficiency, either the incoming impurity flux needs to be reduced or the operating temperature of the alloy must be increased so that the oxides and carbides can diffuse into the alloy bulk more quickly. In both cases, however, the alloy will be consumed at an accelerated rate.

Preconditioning the effluent stream reduces or eliminates alloy consumption. Water vapor can be removed with driers; hydrocarbons can be decomposed on nickel powder. The alloy, drier, and nickel reactor can be regenerated and re-used. ST198 scavenger beds protected by driers and nickel beds in high impurity load applications, such as glovebox atmosphere clean-up service, have demonstrated continued long-term service at LLE without noticeable deterioration in performance over several years.

3. Molecular Sieve Driers

Many aspects of these driers have been discussed throughout this document. The following description highlights some of the salient features of these driers.

Driers based on zeolites, particularly 4A and 5A molecular sieves, are widely used in the tritium community to remove moisture from both noble-gas and air-bearing carrier streams. Typically, these devices operate at room temperature and provide upwards of seven weight-percent storage capacities without exceeding an exhaust dew point of –40°C. Water vapor is adsorbed on the zeolite; hydrogen and organic volatile species tend not to condense in significant amounts on the zeolite. The usefulness of the driers in removing tritiated water vapor from air streams has been discussed in **Options for Tritium Capture** (p. 144) and **Typical Tritium-Capture Schemes** (p. 146).

Water vapor from the atmosphere represents a considerable impurity burden on the hydride-forming materials. For example, water vapor from the atmosphere permeating through gloves into a two cubic meter glovebox with eight standard glove ports can easily accumulate 100 ml of water per month. Without drying the stream, an entire reactor containing 5 kg of Zr-Fe alloy would be oxidized within one year.

As previously discussed, driers should be regenerated in counter-flow, that is, in the opposite direction to normal use. Tritiated water vapor that migrated through the drier to the exhaust end during normal usage is pushed back toward the entrance side of the drier during the counter-flow regeneration. This regeneration philosophy improves the detritiation efficiency of the drier during normal service.

Typically, molecular sieve driers are regenerated between 300°C and 350°C. Progress in regenerating a drier can be

[(m)]Impurities bind chemically to the alloy surface as oxides or carbides of iron or zirconium. Gradually, the oxygen and carbon molecules diffuse into the alloy bulk where they continue to remain bound as oxides or carbides. In the process, the surface reactivates itself and can adsorb elemental hydrogen once again.

monitored by measuring the temperature of the purge gas leaving the drier. During the early phase of a regeneration cycle, the gas temperature leaving the drier will remain at, or close to, room temperature, even though the drier shell is fixed at 350°C. Most of the energy delivered to the molecular sieve by external band heaters clamped to the drier shell or by heated purge gas is used to desorb the water from the molecular sieve. Once the majority of the water has been released and purged from the drier, the temperature of the exhaust gas will gradually increase to the regeneration temperature. To thoroughly void the drier, the regeneration cycle should continue an additional 5000 volume exchanges of the drier, while the exhaust gas is at the regeneration temperature.

4. Cryogenic Molecular Sieve

The earliest application of cryogenic molecular sieves[(n)] was to separate hydrogen isotopes by gas–solid chromatography for the purpose of analyzing isotopic mixtures of elemental hydrogen.[19] Since that time, a variety of isotopic separation systems have been developed to selectively recover tritium from the other hydrogen isotopes.[20]

As temporary storage devices, however, cryogenic molecular sieves have found limited general utility in the tritium community. Nevertheless, these devices offer unique service in specialized applications, namely as short-term traps to capture tritium gas from a carrier and as tritium gas concentrators. For example, without the concentration step provided by the cryogenic molecular sieve, tritium could not be transferred to uranium from Zr-Fe except at high tritium partial pressures. At a concentration of 1 mCi/m^3, elemental tritium will pass through the uranium powder without reacting. At 77 K, the molecular sieve can condense hydrogen on its surfaces to reduce the hydrogen partial pressures in the carrier into the 10^{-6} to 10^{-5} torr range and release the hydrogen at a partial pressure of several mTorr when heated to 150 K. As a consequence, tritium can be released from a Zr-Fe reactor at an activity of 1 mCi/m^3, accumulated on a cryogenic molecular sieve, and released as a slug of gas at concentrations exceeding 1 Ci/m^3 at 150 K.

Figure 103.32 illustrates the transfer of tritium gas from ST198 alloy to a cryogenic molecular sieve. Helium gas exits from hot ST198 alloy, flows through a cryogenic molecular sieve, and returns to the ST198 alloy. In this example, the carrier activities at the ST198 exhaust and the cryogenic exhaust are monitored as a function of time. The activity at the ST198 exhaust varies with the temperature of the alloy and is seen to increase as high as 810 mCi/m^3. The activity of the helium gas leaving the cryogenic molecular sieve remains below 50 μCi/m^3, the sensitivity level of the in-line ionization chamber. At 88 min into the operation, tritium breaks through the molecular sieve and the activity of the gas leaving the cryogenic molecular sieve increases rapidly, albeit in the low mCi/m^3 range. The hydrogen content leaving the ST198 was not measured in this test. These tests demonstrate the excellent performance of the cryogenic molecular sieve trap to decontaminate the carrier stream, attaining DF's up to (750/0.5) 1500 in a single pass. This figure of merit is conservative since the presence of hydrogen was not included in the estimate.

At 77 K, tritium gas is resident on the cryogenic molecular sieve for a finite time and will slowly migrate toward the exhaust end of the bed. The transport rate from bed entrance to exhaust depends on the carrier flow rate, resident tritium inventory, resident hydrogen inventory, and the quantity of polar impurities adsorbed on the zeolite. Capacities of the order of 100 scc of elemental gas per gram of molecular sieve can be achieved on conditioned molecular sieve.

In a second example, a cryogenic molecular sieve can be used to capture the accidental release of elemental tritium from a process loop. In this case, the majority of the tritium may be held up on a cryogenic molecular sieve for 1 or 2 h before migrating through the bed. During this time, an operator can rectify the problem and return the gas directly to a storage bed.

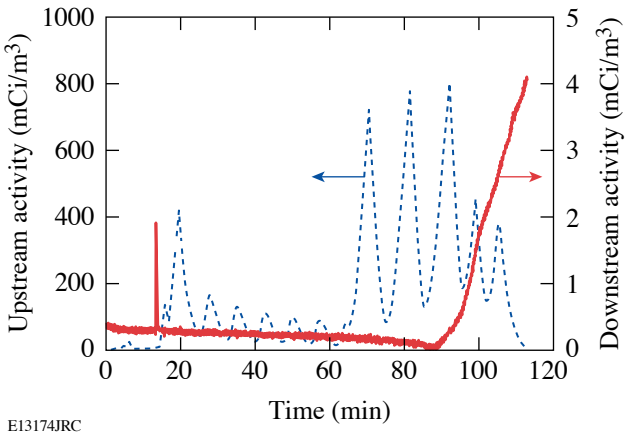

Figure 103.32
Comparison of tritium activities upstream and downstream of a cryogenic molecular sieve bed during the regeneration of a Zr-Fe bed. Helium carrier flow rate is 28 sLPM.

[(n)]Cryogenic molecular sieves operate at 77 K.

Cryogenic molecular sieve beds can be regenerated in steps to release different tritiated species. By raising the molecular sieve temperature from 77 K to 150 K, the elemental tritium gas will be released. Increasing the temperature further to 350°C will release all other bound impurities. Elemental tritium can be directed to one treatment process while impurities can be directed to a second treatment process.

These devices have several limitations. They are restricted to operate in helium purge streams, and the residence time on the molecular sieve is limited. Cryogenic molecular sieve beds behave more like capacitors than storage devices. They are not passively safe in that liquid nitrogen is needed to hold the tritium gas in place. There is limited experience with these devices in the tritium community for the applications discussed. Despite these limitations, however, cryogenic molecular sieve beds will fill a unique application in tritium-handling systems in the coming years.

Throughput and Construction Guidelines

The capture technology discussed in this article is intended for small-scale operations, typically required to operate between 10 standard liters/min (sLPM) to 60 sLPM with a focus on treating the emission as close to the source as feasible. Flow rates in the 10-sLPM range are suitable to a variety of process loops. Flow rates in the 60-sLPM range are more suited to glovebox cleanup applications. Table 103.III lists the approximate size of each capture device for these two throughput extremes and for three applications.

All heated devices must be rated to withstand elevated pressures, that is, they must be rated as pressure fittings. These devices must be constructed in shops qualified to build pressure vessels. The vessels must be helium leak-tight to 1×10^{-9} atm-cc/s when exposed to 1 atm of helium. The valves should be bellows-sealed and use a copper or stellite stem tip. Where valve actuation will be automated, VESPEL®[(o)] stem tips can be used, although these will require routine replacement. Stainless-steel frits should be integrated into device designs to prevent particulate transport into the process loop or the exhaust line.

Double containment can be used for devices that are expected to operate at an elevated temperature, such as uranium storage beds, where tritium permeation can be problematic. Doubly contained devices provide a secondary shell around the primary vessel. Heaters and thermocouples are attached to the primary vessel, and vacuum feed-throughs are used to access the heaters and thermocouples. The annular region between the primary and secondary vessels is evacuated and maintained under vacuum during operation. Periodically, the region is pumped to recover any tritium that has permeated into the interspace. Doubly contained devices release less tritium by permeation and consequently reduce the spread of surface contamination in the vicinity of the device. Additionally, these devices reduce heat loads in confined spaces such as gloveboxes. However, double-containment devices can easily cost twice that of single-containment device.

Uranium scavenger beds require manufacturing shops knowledgeable in handling and conditioning uranium. These facilities must be licensed to receive and handle bulk uranium metal. Manufacturing Zr-Fe and nickel beds requires caution to ensure the getter material is not accidentally oxidized during the manufacturing process.

Table 103.III: Size of the devices (in kilograms) used for three different detritiation applications.

Device	Application		
	Effluent treatment system without air[(a)]	Glovebox cleanup system using helium[(b)]	Detritiation system for high-humidity air streams[(b)]
Oxidizer	Not used	Not used	1
Drier	Not used	3	5
Nickel bed	1[(c)]	1.5	Not used
Uranium bed	1	Not used	Not used
Zr-Fe bed	3	5	Not used

[(a)]A volumetric flow rate below 10 sLPM is assumed,

[(b)]A volumetric flow rate of 60 sLPM is assumed.

[(c)]The quantity of material used in each device reflects the overall size of the capture devices.

[(o)]VESPEL® is a polyimide with good stability under radiation exposure.

Conclusion

Significant developments in tritium-capture technology for both air and inert gas streams have occurred over the past two decades. Tritium removal from air streams requires the oxidation of elemental tritium and the collection of the tritiated water on driers; recovery from inert streams can also use the oxidation. Alternately, metal getter technology can be used to detritiate inert gas streams by collecting elemental tritium directly without the oxidation step.

Direct elemental tritium recovery offers several advantages. Elemental tritium is significantly less hazardous to handle than tritium oxide. In some cases, the elemental tritium can be returned to the original storage device for re-use. Oxidation technology tends to be more robust; however, unless special infrastructure is installed, oxidized tritium is a waste stream destined for land disposal. Each tritium-capture application should be carefully evaluated to assess the merits and drawbacks of oxidation against direct elemental recovery before selecting a capture technology.

Capture technology does not provide magical "bolt-on" solutions to process systems that suffer from chronic or repeated accidental releases. Rather, this technology must be integrated with the operation of the process systems. Both the process systems and the capture technology need to be configured for reliable, fail-safe operation. For example, circulating closed-loop capture subsystems are preferred to once-through subsystems. Process loop exhaust lines to the stack should be monitored for activity and interlocked with valves that automatically isolate the system from discharging tritium to the stack above predetermined limits.

Economics favors small-scale systems. Emissions should be treated as close to the source as possible, certainly before any significant dilution with air or inert gas occurs, as the first step in reducing the size of the capture equipment. Distributed capture subsystems are preferred to one large clean-up system attached to the stack; the former costs significantly less. Additionally, releases in one process do not impact the operation of other processes.

ACKNOWLEDGMENT

This work was supported by the U.S. Department of Energy Office of Inertial Confinement Fusion under Cooperative Agreement No. DE-FC52-92SF19460, the University of Rochester, and the New York State Energy Research and Development Authority. The support of DOE does not constitute an endorsement by DOE of the views expressed in this article.

REFERENCES

1. C. Boffito *et al*., J. Vac. Sci. Technol. **18**, 1117 (1981).
2. C. Boffito, F. Doni, and L. Rosai, J. Less-Common Met. **104**, 149 (1984).
3. P. Manini *et al*., Vuoto Sci. Tecnol. **XX**, 299 (1990).
4. W. T. Shmayda, N. P. Kherani, B. Wallace, and F. Mazza, Fusion Technol. **21**, 616 (1992).
5. K. J. Maynard, N. P. Kherani, and W. T. Shmayda, Fusion Technol. **28**, 1546 (1995).
6. W. T. Shmayda and N. P. Kherani, Fusion Eng. Des. **10**, 359 (1989).
7. A. B. Antoniazzi and W. T. Shmayda, Fusion Technol. **30**, 879 (1996).
8. W. T. Shmayda, in *Safety in Tritium Handling Technology*, edited by F. Mannone, Nuclear Science and Technology, Vol. 1 (Kluwer Academic Publishers, Dordrecht, The Netherlands, 1993), pp. 23–52.
9. H. Brunnader, W. T. Shmayda, D. R. Harding, L. D. Lund, and R. Janezic, Fusion Sci. Technol. **41**, 840 (2002).
10. A. Nobile, H. Reichert, R. T. Janezic, D. R. Harding, L. D. Lund, and W. T. Shmayda, Fusion Sci. Technol. **43**, 522 (2003).
11. G. R. Longhurst, A. G. Heics, and W. T. Shmayda, Fusion Technol. **21**, 1017 (1992).
12. G. R. Longhurst and W. T. Shmayda, Fusion Eng. **2**, 812 (1989).
13. W. T. Shmayda and P. Mayer, J. Less-Common Met. **104**, 239 (1984).
14. N. P. Kherani and W. T. Shmayda, in *Proceedings of the Seventh Annual Conference* (Canadian Nuclear Society, Toronto, Ontario, Canada, 1986), pp. 232–236.
15. N. P. Kherani, W. T. Shmayda, and A. G. Heics, Z. Phys. Chem. **164**, 1421 (1988).
16. W. T. Shmayda, N. P. Kherani, and A. G. Heics, J. Vac. Sci. Technol. A **6**, 1259 (1988).
17. W. M. Mueller, J. P. Blackledge, and G. G. Libowitz, *Metal Hydrides* (Academic Press, New York, 1968).
18. W. T. Shmayda and N. P. Kherani, Fusion Eng. Des. **10**, 359 (1989).
19. P. L. Gant and K. Yang, Science **129**, 1548 (1959).
20. C. H. Cheh, J. Chromatography A **658**, 283 (1994).

All-Solid-State, Diode-Pumped, Multiharmonic Laser System for Timing Fiducial

Introduction

Laser timing fiducial signals are required as a timing reference for numerous laser and target diagnostics for inertial confinement fusion experiments. On OMEGA, infrared as well as visible and ultraviolet timing fiducial signals are needed to match the wavelength sensitivity of various diagnostics. Currently, a flash-lamp–pumped Nd:YLF/Nd:glass laser system operating at 1053 nm with frequency conversion to the second and fourth harmonics (527 and 264 nm) is used.[1] The system consists of a Nd:YLF master oscillator; a pulse-shaping system; a flash-lamp–pumped Nd:YLF regenerative amplifier; a Nd:glass, large-aperture ring amplifier; and frequency-conversion crystals. This fiducial laser system has a complicated design, a low repetition rate, low harmonic conversion efficiency, high maintenance because of flash-lamp pumping, and occupies a 5×14-ft optical table and a rack of electronics. We present an all-solid-state, diode-pumped, compact laser fiducial system that satisfies all OMEGA requirements, reduces the system complexity, and improves reliability while significantly reducing the space requirements.

Fiducial Laser System Requirements

The OMEGA fiducial laser system must produce a 3.5-ns comb of 200-ps FWHM optical pulses separated by 0.5 ns at IR, green, and UV wavelengths. A Nd:YLF laser system with second and fourth harmonic generators is used to produce IR, green, and UV fiducial signals. The amplitude variation of each pulse in the comb must not exceed 50% of the maximum. The required IR/green comb energy is 1 mJ. The most critical requirements for the fiducial system are 10-mJ energy at UV (4ω) fiducial and a stable time delay (~165 ns) between the IR/green and UV fiducials.

High-UV fiducial energy is required because of low photocathode sensitivity for the x-ray streak cameras employed as important OMEGA target diagnostics. A UV multimode fiber delivery system is used to couple fiducial combs into the diagnostics. The required UV energy is 10 μJ at the output of a fiber launcher. OMEGA needs up to 19 channels of UV fiducial; therefore, a 19-fiber bundle is used to launch the UV comb into the delivery fibers. To provide equal energy distribution and misalignment insensitivity for the fiber-bundle launcher, a UV fiducial beam must significantly overlap the 19-fiber bundle, bringing the total UV comb energy required to 10 mJ. Frequency-conversion efficiencies of 50%–75% for both second and fourth harmonic generation have been demonstrated;[2] therefore, the required IR energy should be in the 20- to 40-mJ range.

The relatively long delay between UV and IR/green fiducials is dictated by the physical location of various OMEGA diagnostics. IR/green fiducials must be generated ~165 ns before the UV comb to provide the simultaneous arrival of the fiducials to all OMEGA diagnostics. A 165-ns delay line is required between the IR/green and UV fiducial fiber launchers.

Laser System Description

A block diagram of the proposed system is shown in Fig. 103.33. The system is seeded by a shaped comb produced by a pulse-shaping system.[3] A single-frequency, diode-pumped Nd:YLF OMEGA master oscillator (OMO)[4] produces a 20-ns square pulse for shaping. The first integrated optics modulator is driven by the 24th harmonic of the 38-MHz OMEGA master-timing RF source. The second modulator is driven with a gate pulse that is precompensated for pulse-shape distortion caused by gain saturation in the amplifiers and gates an eight-pulse fiducial comb. A Nd:YLF OMEGA diode-pumped regenerative amplifier (ODR)[5] boosts the comb energy from tens of picojoules to ~4 mJ, the main portion of which is used as an IR fiducial and for generating a green fiducial.

An additional ODR is added to the system to provide the required 165-ns delay with a small footprint and without beam degradation. At the same time, it produces the additional gain required to achieve the UV energy specification. A portion of the ODR output is used to seed the second regenerative amplifier designated ODR+. A double-pass, diode-pumped amplifier provides additional gain and is discussed further in **Two-Pass,**

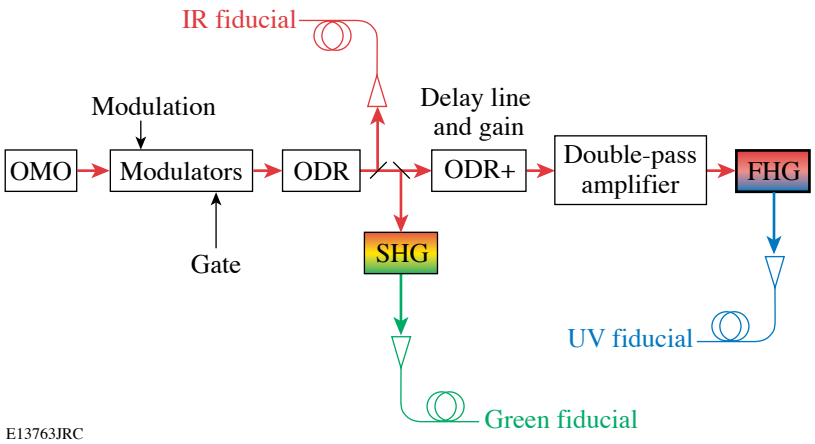

Figure 103.33
A block diagram of the proposed OMEGA fiducial laser system. OMO is the OMEGA master oscillator, ODR is the OMEGA diode-pumped regenerative amplifier, SHG and FHG are the second and fourth harmonic generators. The ODR, seeded by a pre-compensated fiducial comb, produces IR and green fiducial signals. ODR+ provides the necessary delay between IR/green and UV fiducials.

Diode-Pumped Nd:YLF Amplifier. Second-harmonic generation (SHG) and fourth-harmonic generation (FHG) are realized with BBO (beta-barium borate) crystals.

The ultraviolet pulses are launched into a bundle of 19 UV fibers to distribute UV fiducials to various OMEGA diagnostics.

Two-Pass, Diode-Pumped Nd:YLF Amplifier

The double-pass amplifier must produce 20 to 40 mJ of output energy in IR. Amplifier efficiency has to be estimated for the appropriate pump power choice. Amplifier efficiency includes (a) pump energy to active-element upper-state energy-conversion efficiency and (b) upper-state energy to amplifier output conversion efficiency.[6] Typical efficiencies for a Nd:YLF amplifier pumped by a fiber-coupled diode array through a dichroic mirror are

- Pump re-imaging optics transmission: 0.94
- Dichroic mirror transmission: 0.93
- Pump absorption: 0.8
- Quantum efficiency: 0.72

Pump energy to upper-state energy-conversion efficiency: 0.5.

Storage efficiency is calculated as follows:

$$\eta_s = \left[1 - \exp\left(-t_p/t_f\right)\right] \Big/ \left(t_p/t_f\right),$$

where t_p is the pump-pulse width and t_f is the active medium fluorescence lifetime. In the case of diode pumping, when the pump-pulse shape and wavelength do not change with the pulse duration increase, it is beneficial to make the pump pulse longer to increase the total stored energy. For Nd:YLF with $t_f = 0.5$ ms, a 1-ms pump pulse is used.

- Storage efficiency: 0.43
- Beam overlap efficiency: 0.75
- ASE loss: 0.05
- Gain extraction efficiency: 0.95

Upper-state energy to amplifier output conversion efficiency: 0.29

Total diode-pumped, Nd:YLF amplifier optical-to-optical efficiency: <0.15

Achieving 40 mJ of amplifier output energy requires 270 mJ of pump energy or 270 W of quasi-continuous wave power from a fiber-coupled diode array. To produce a uniformly pumped volume, an active element is pumped from both sides by 150-W, fiber-coupled diode packages from Apollo Instruments (Irvine, CA). The delivery fiber has a 1-mm core diameter. To avoid optical damage of the active element, the fluence is kept below 5 J/cm^2, and the delivery fiber is re-imaged into an active element with 2× magnification. Using the Frantz–Nodvik equation,[7] the output energy of an amplifier was calculated (Fig. 103.34). Achieving a >40-mJ amplifier output requires >10-mJ input energy.

An ODR produces ~4 mJ of energy when pumped with two 25-W fiber-coupled diodes, which yields an amplifier output of only 25 mJ. In order to increase amplifier input energy, the ODR+ is pumped with one 150-W fiber-coupled diode array (Apollo Instruments). The ODR+ output energy is >13 mJ at the maximum pump energy (Fig. 103.35). With this input, the amplifier produces ~50 mJ of IR, meeting the energy requirement.

The double-pass, all-solid-state, diode-pumped Nd:YLF amplifier shown in Fig. 103.36(a) is built as a generic platform for use in a variety of applications, including a laser system for OMEGA frequency-conversion crystal tuning.[8] An input

telescope can accommodate input beams with diameters in the range of 1 to 8 mm. The output telescope resizes and collimates the beam for efficient frequency conversion. A built-in fiber pickoff allows monitoring of the amplified pulse shape with a fast photodetector and oscilloscope. The amplifier output beam profile shown in Fig. 103.36(b) is excellent.

A block diagram of the frequency conversion setup is shown in Fig. 103.37. BBO crystals are utilized for frequency conversion to the fourth harmonic. An 11-mm-long type-I crystal is employed for SHG, followed by a 6-mm-long type-I crystal for FHG. A fused-silica Pellin–Broca prism is used to spatially separate the UV fiducial beam, and a telescope matches the beam size to efficiently launch the UV pulses into a multimode fiber bundle.

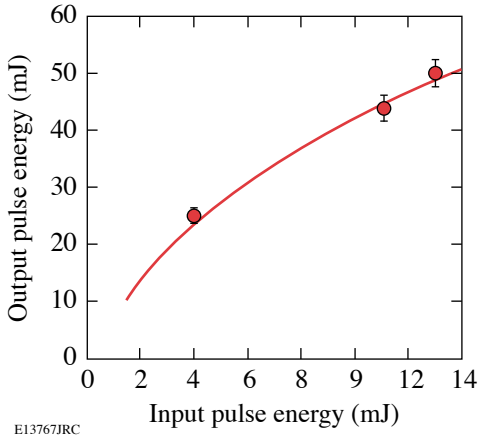

Figure 103.34
The output energies of a double-pass Nd:YLF amplifier calculated using the Frantz–Nodvik equation (solid line) and measured (open circles) are in good agreement.

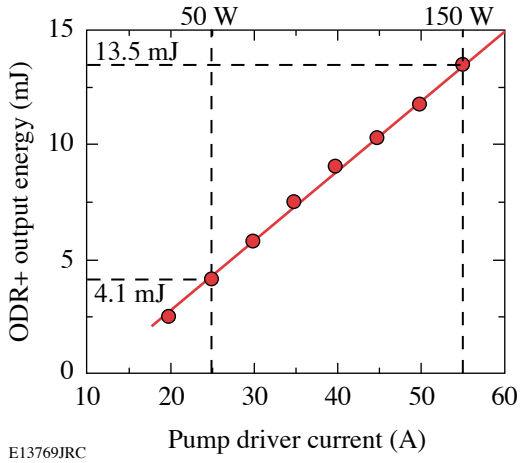

Figure 103.35
ODR+ is able to produce sufficient energy for efficient double-pass amplifier energy extraction.

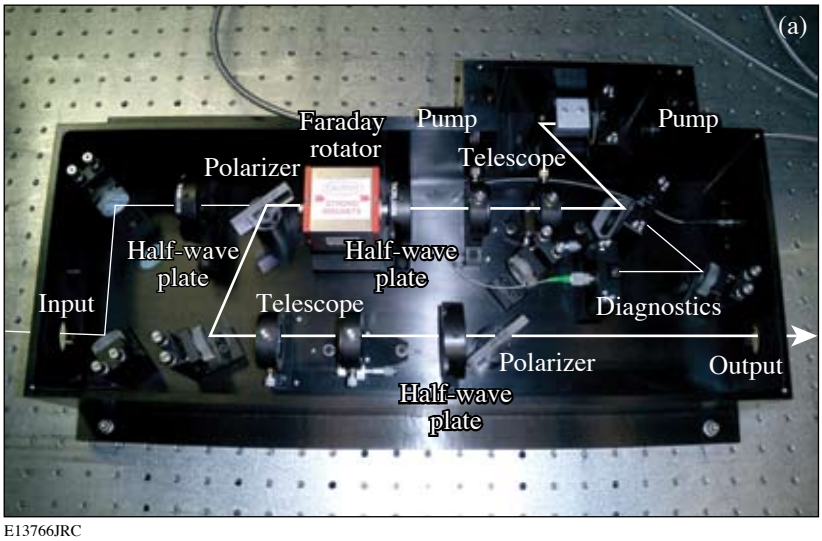

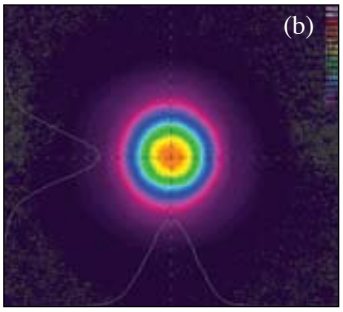

Figure 103.36
(a) All-solid-state, diode-pumped, double-pass Nd:YLF amplifier. (b) The output beam profile is excellent.

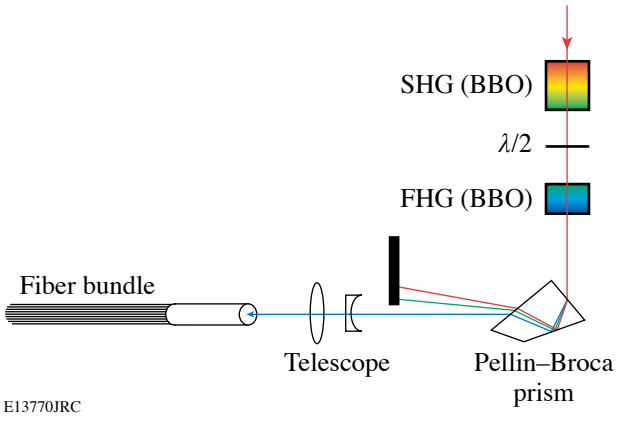

Figure 103.37
A block diagram of UV frequency conversion setup and fiber bundle launching.

Experimental Results

The double-pass amplifier must be heavily saturated in order to achieve high efficiency. To compensate for gain saturation, the ODR+ timing is set such that a switch-in Pockels cell shapes the first three to four pulses of the injected comb, decreasing their amplitudes. Even with this precompensation, the best pulse shape achieved [Fig. 103.38(a)] does not meet the requirements. After FHG, the first pulse in the comb shows significant reconversion into the fundamental wavelength, which results in two peaks instead of one [Fig. 103.38(b)], making the UV fiducial comb useless.

The ultraviolet comb energy has been measured in each fiber of the 19-fiber bundle [Fig. 103.39(a)]. On average, it is 4× higher than the requirement; therefore, the gain of the system can be reduced to avoid comb envelope distortion. With the two-pass amplifier off and the IR beam resized for efficient FHG, the energy requirement has been met [Fig. 103.39(b)]. Fourth-harmonic generation efficiency of over 30% has been observed without any sign of reconversion.

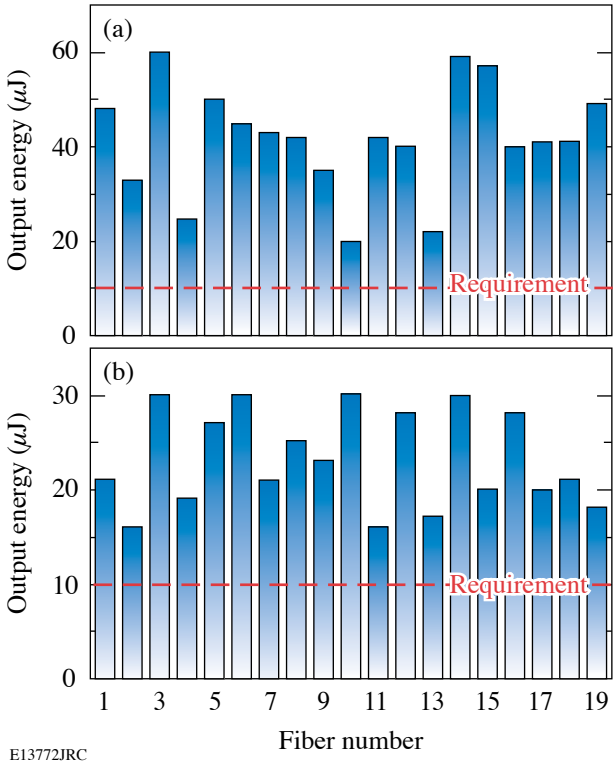

Figure 103.39
The double-pass amplifier produces, on average, 4× more energy than required at the fiber-bundle output (a). ODR+ delivers enough energy to meet the requirement (b).

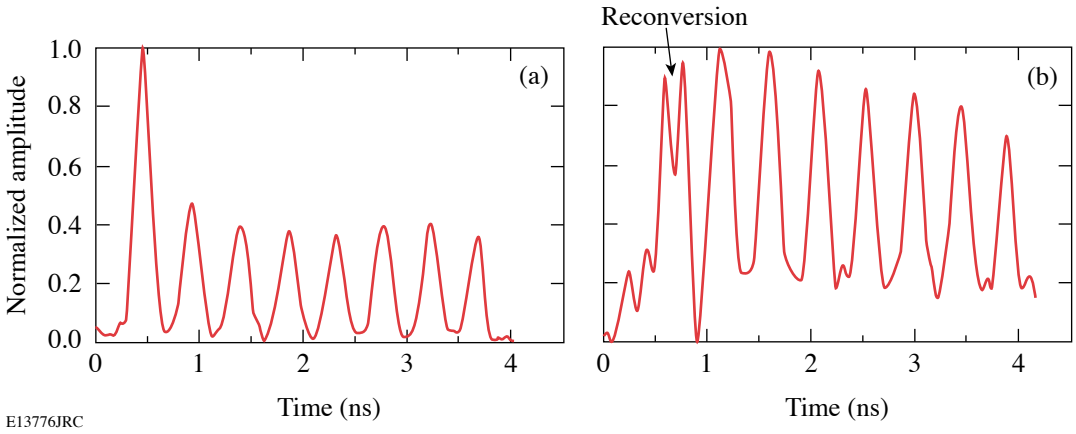

Figure 103.38
Double-pass amplifier IR output (a) and UV comb (b) pulse shapes. The first pulse in the UV comb shows significant reconversion of UV energy.

The fiducial comb injected into the ODR [Fig. 103.40(a)] has been precompensated such that both the green [Fig. 103.40(b)] and UV fiducials [Fig. 103.40(c)] meet the amplitude requirement. Fiducial laser system performance parameters have been measured over three days of operation. Figure 103.41 shows the stability of a UV fiducial comb in one of the fibers over three days; the peak pulse shape stability is ~2% rms. The UV energy stability is 1.5% rms over the same period of time.

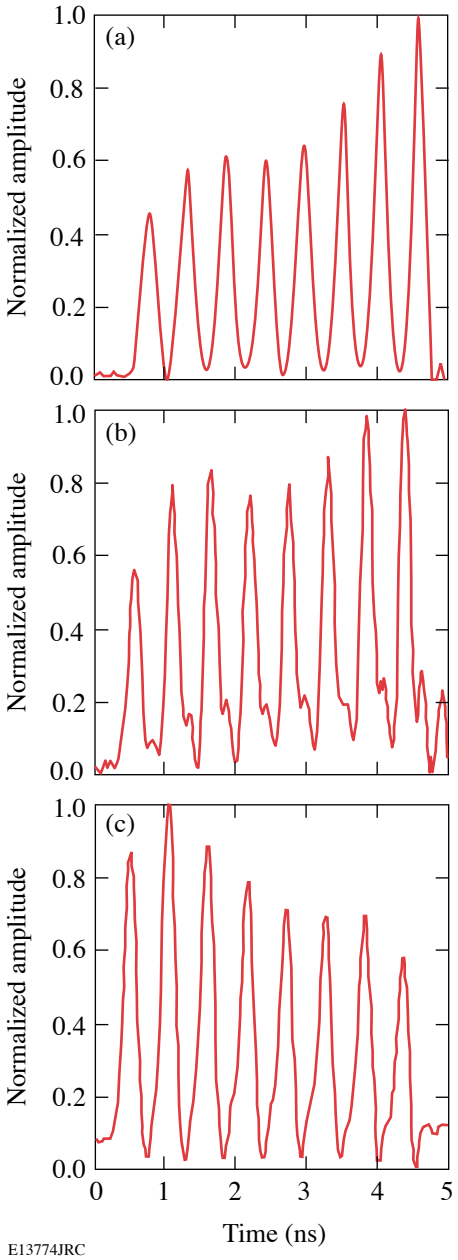

Figure 103.40
The ODR injection fiducial comb (a) is precompensated such that the green (b) and UV (c) fiducials satisfy the requirements.

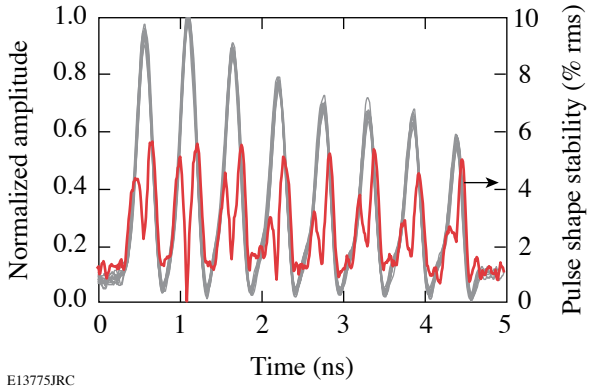

Figure 103.41
The UV fiducial peak pulse-shape stability is ~2% rms, and the energy stability is 1.5% rms over three days of operation.

Conclusion

An efficient, all-solid-state, diode-pumped fiducial laser system that produces IR, green, and UV fiducial combs for the OMEGA diagnostics timing reference has been developed, built, tested, and optimized. All requirements have been met. Excellent beam profile, high energy, and pulse-shape stability have been demonstrated. The turn-key system improves reliability compared to the existing flash-lamp–pumped system and has a smaller footprint of 4×5 ft.

ACKNOWLEDGMENT

This work was supported by the U.S. Department of Energy Office of Inertial Confinement Fusion under Cooperative Agreement No. DE-FC52-92SF19460, the University of Rochester, and the New York State Energy Research and Development Authority. The support of DOE does not constitute an endorsement by DOE of the views expressed in this article.

REFERENCES

1. A. Babushkin, W. Seka, S. A. Letzring, W. Bittle, M. Labuzeta, M. Miller, and R. Roides, in *22nd International Congress on High-Speed Photography and Photonics*, edited by D. L. Paisley and A. M. Frank (SPIE, Bellingham, WA, 1997), Vol. 2869, pp. 540–544.

2. C. Chen *et al.*, in *Laser and Nonlinear Optical Materials*, edited by L. G. DeShazer (SPIE, Bellingham, WA, 1986), Vol. 681, pp. 12–17.

3. M. D. Skeldon, Rev. Sci. Instrum. **71**, 3559 (2000).

4. A. V. Okishev, M. D. Skeldon, and W. Seka, in *Advanced Solid-State Lasers*, edited by M. M. Fejer, H. Injeyan, and U. Keller, OSA TOPS, Vol. 26 (Optical Society of America, Washington, DC, 1999), pp. 228–235.

5. A. V. Okishev and J. D. Zuegel, Appl. Opt. **43**, 6180 (2004).

6. W. Koechner, *Solid-State Laser Engineering*, 4th rev. ed., Springer Series in Optical Sciences, Vol. 1 (Springer, Berlin, 1996).

7. L. M. Frantz and J. S. Nodvik, J. Appl. Phys. **34**, 2346 (1963).

8. A. Babushkin, R. S. Craxton, S. Oskoui, M. J. Guardalben, R. L. Keck, and W. Seka, Opt. Lett. **23**, 927 (1998).

EXAFS Measurement of Iron bcc-to-hcp Phase Transformation in Nanosecond-Laser Shocks

Introduction

The dynamics of material response to shock loading has been extensively studied in the past.[1] The goal of those studies was to understand the shock-induced deformation and structural changes at the microscopic level. Laser-generated shocks have been recently employed[2] to broaden these studies to higher pressures (~100 GPa) and strain rates (~10^7 s^{-1} to 10^8 s^{-1}). The use of *in-situ* EXAFS for characterizing nanosecond laser-shocked vanadium and titanium has been recently demonstrated.[3] Additionally, the observed fast decay of the EXAFS modulations in titanium shocked to ~40 GPa was shown[3] to be due to the α-Ti to ω-Ti phase transformation. We show that EXAFS can likewise be used to demonstrate the bcc-to-hcp phase transformation in iron. The great interest in this transformation stems from the fact that a significant part of the earth's core is thought to consist of hcp iron.[4] Initially, Bancroft *et al*.[5] showed that the multiple fronts propagating within shocked iron indicated a phase transformation at around 13 GPa. Subsequently, Jamieson and Lawson have shown,[6] by diffraction in a diamond anvil cell, that a bcc-to-hcp phase transformation indeed occurs at around 13 GPa. The historical importance of this transition is that it was first observed under shocked, rather than static, compression. It also established the reliability of shocks for obtaining pressure-compression relations. The transformation has been extensively studied in gas-gun shock experiments[7,8] using the velocity history of the back surface of the target, where a long ($\gg$10 ns) characteristic time for the transformation was deduced. This contrasts with the subnanosecond time derived in the present experiment. The longer times deduced from velocity measurements[7] have been explained[8] in terms of the pressure dependence of the characteristic time. Using Fig. 5 of Ref. 8, we can estimate a characteristic time for iron at a pressure of 35 GPa of ~5 ns. Much shorter times have been inferred from the residual microstructure that is quenched after the passage of nanosecond and even subnanosecond shocks.[9] This observation of the transformation in nanosecond laser shocks confirms the latter finding. Unlike the evidence[9] derived from the examination of residual microstructure after the experiment, the measurements here are *in-situ*.

The EXAFS spectrum of iron is markedly different in the bcc (or α-Fe) phase as compared with the hcp (or ε-Fe) phase;[10] this provides a signature for identifying the transformation in laser-shock experiments. Transient phase-transformation experiments require methods for characterizing the crystal conditions (e.g., the pressure) during the transformation to substantiate the occurrence of the transformation. In static compression experiments, the temperature and pressure are independently controlled and measured. We show that the temperature and compression (and, hence, the pressure) can be deduced from the EXAFS record itself in addition to providing evidence of the phase transformation.

Experimental Setup

K-edge EXAFS measurements were performed on iron shocked to ~35 GPa with a 3-ns laser pulse, provided by 3 of the 60 beams of the OMEGA laser.[11] The radiation source for the EXAFS measurement was obtained by imploding a spherical target using the remaining 57 OMEGA beams. In a previous paper,[12] we showed that a CH shell imploded by a multibeam laser system emits intense and spectrally smooth radiation, lasting ~120 ps, and is suitable for EXAFS measurements on nanosecond time scales.

Figure 103.42 shows a schematic of the experimental configuration used to measure K-edge EXAFS absorption spectra in laser-shocked iron targets. Two cross-calibrated, flat-crystal spectrometers equipped with a Ge (1,1,1) crystal were used for measuring the incident and transmitted spectra on a single laser shot. The three shock-generating laser beams were stacked to form a 3-ns square pulse focused to an irradiance of 0.4 to 0.5 TW/cm^2. The delay time of the three-stacked beams, with respect to the remaining beams, was adjusted so that peak implosion (and emission) of the spherical target occurred just when the shock wave exited the metal layer. The planar target consisted of 8-μm-thick polycrystalline iron foil (purity of 99.85%) coated on both sides with a 17-μm-thick CH layer; thus, the iron layer is directly affected by the shock but not by the laser absorption and heating. A heat shield (1-mm-thick CH foil) minimizes the heating of the metal layer by the soft

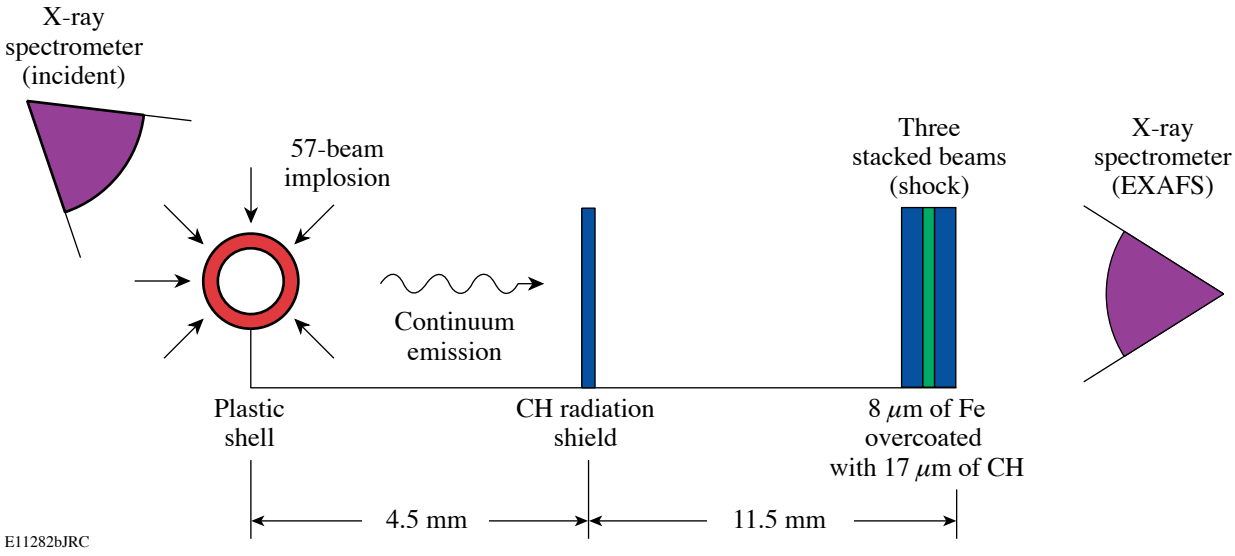

Figure 103.42
Schematic of the experimental configuration. The spherical target, imploded by 57 laser beams, serves as a radiation source for EXAFS measurements. The three-stacked beams launch a shock through the iron layer.

radiation from the imploding spherical target. The iron thickness is the largest that can still yield significant transmitted x-ray intensity. Although the spectrometers used in the EXAFS measurement are time integrated, a meaningful shock diagnosis can be obtained without streaking the spectrum in time because the x-ray pulse width is only ~120 ps,[12] much shorter than the shock transit time through the metal (~2 ns).

Theory

The expected shock strength and the properties of the shocked iron were determined using 1-D simulations with the hydrodynamic code *LASNEX*.[13] The tabular equation of state incorporated into the code includes the α-Fe to ε-Fe phase transformation. Figure 103.43 shows the computed profiles just as the shock exits the iron layer. The volume-averaged values are a pressure of 36 GPa, a temperature of 645 K, and a compression of 1.2 (or 20%).

The measured spectra were analyzed with the FEFF8 *ab initio* EXAFS software package.[14] The basic theory of EXAFS[15] yields an expression for the relative absorption $\chi(k) = \mu(k)/\mu_0 k - 1$, where $\mu(k)$ is the absorption coefficient and $\mu_0(k)$ is the absorption of the isolated atom. The wave number k of the ejected photoelectron is given by the de Broglie relation $\hbar^2 k^2/2m = E - E_K$, where E is the absorbed photon energy and E_K is the energy of the K edge. The FEFF8 package uses the scattering potential to calculate the amplitude and phase shift of the photoelectron waves scattered from several

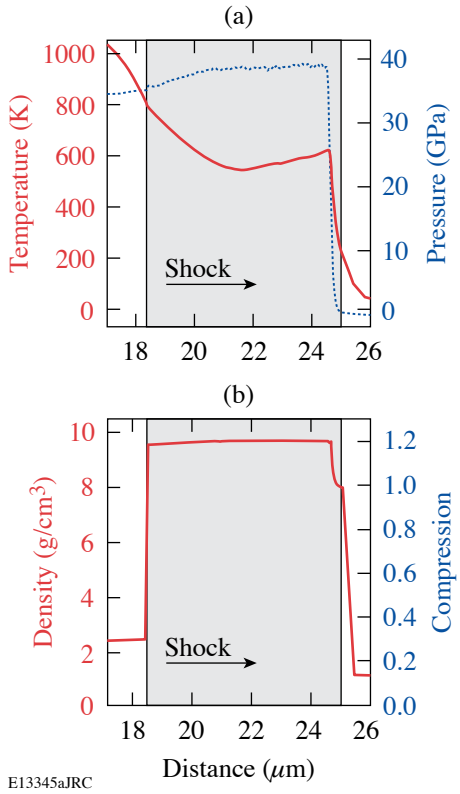

Figure 103.43
Profiles of (a) target pressure and temperature and (b) density calculated by *LASNEX* (the iron layer, enclosed within CH layers, is highlighted). The laser propagates toward the right.

shells of neighboring atoms, including multiple-scattering paths. The main fitting parameters are the nearest-neighbor distance R and the vibration amplitude σ^2 appearing in the Debye–Waller term.[15] The distance R yields the density or compression; σ^2 as a function of temperature was calculated using the Debye model[16] for the phonon density of states, including correlation, and it also depends on the density through the Debye temperature. The density dependence of the Debye temperature for Fe-ε was taken from published measurements.[17] The results (shown in Fig. 103.44) can be approximated by $\sigma^2(\text{Å}^2) = 0.001 + 2 \times 10^{-5}\, T(K)/C^{3.58}$, where $C = (\rho/\rho_0)$ is the compression ratio. Using this dependence and the result for σ^2 from FEFF8 fitting, the temperature can be derived.

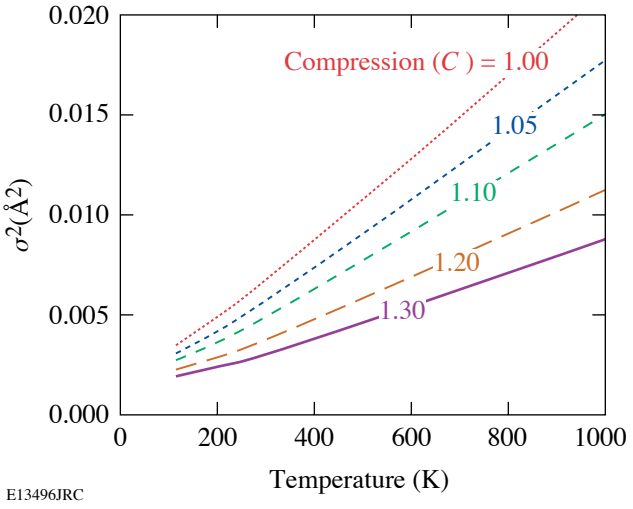

Figure 103.44
Debye–Waller factor (σ^2) of ε-Fe, calculated from the correlated model of Sevillano *et al.*[16] and the measured dependence of the ε-Fe Debye temperature on compression.[17]

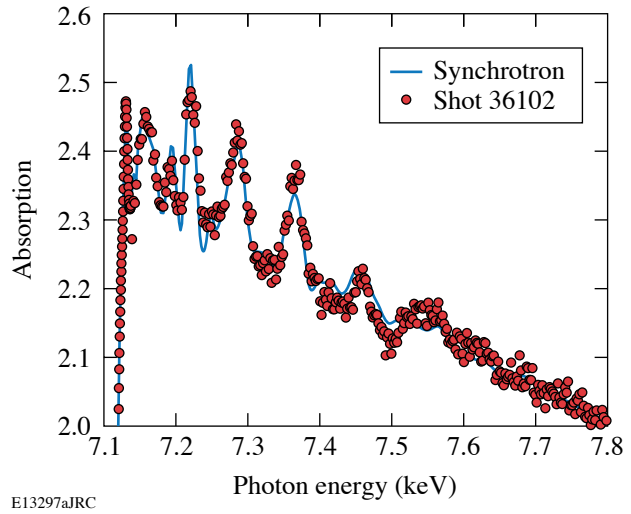

Figure 103.45
Comparison of the measured absorption of unshocked iron on OMEGA and a standard iron EXAFS measured at the Stanford Synchrotron Radiation Laboratory.

Experimental Results and Analysis

To assess the reliability of our Fe EXAFS measurements, we obtained the EXAFS spectrum for unshocked iron using the configuration described above but without firing the shock-launching beams. Figure 103.45 shows a comparison between the resulting absorption and a standard iron absorption spectrum measured at the Stanford Synchrotron Radiation Laboratory (SSRL). The agreement is seen to be good.

EXAFS provides a very distinct, qualitative signature for the bcc-to-hcp phase transformation in iron.[10] This is demonstrated by Fig. 103.46, showing (a) the EXAFS spectrum for the two phases calculated by the FEFF8 code and (b) the EXAFS spectrum measured on OMEGA for unshocked and shocked iron. Anticipating the fitting results described below, a compression of 20% (with respect to the initial bcc density) and a temperature of 700 K were assumed in Fig. 103.46(a) for the hcp phase. The bcc calculation is for room-temperature and ambient-pressure conditions. The main signature of the phase transformation is seen to be the disappearance of the peak marked "W." When the calculations for the bcc phase are repeated for a wide range of compressions, the feature W remains intact. Thus, its disappearance can only be because of the phase transformation, not because of the shock compression (we later show that this is true—even in the case of 1-D compression). The effect of compression on the EXAFS spectrum is to increase the period of oscillation (in k space), and the effect of the heating is to cause the oscillations to decay faster with increasing k; both are evident in Fig. 103.46(a).

The experimental results shown in Fig. 103.46(b) mirror the changes seen in Fig. 103.46(a). Compression and heating are evident, and the disappearance of the W feature indicates a bcc-to-hcp phase transformation. The complete disappearance of that feature indicates that the transformation is complete, hence that its time constant must be shorter than ~1 ns. Additionally, the predicted enhancement in the peak around k ~ 3 Å^{-1} is also observed in Fig. 103.46(b). These results were consistently observed on repeated experiments under the same conditions. These conclusions are borne out by the more precise fitting analysis below.

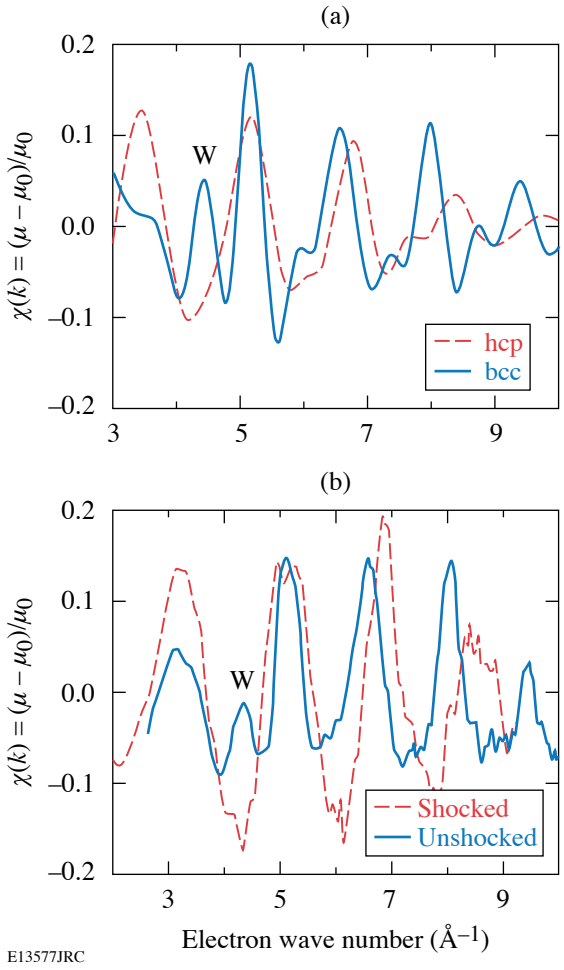

Figure 103.46
(a) FEFF8 code calculation of the EXAFS spectrum for unshocked α-Fe (bcc) and ε-Fe (hcp), the latter compressed by 20% with respect to the initial bcc iron. (b) Experimental results for unshocked and shocked iron. In the shocked case (at a deduced pressure of ~35 GPa), the peak marked W is seen to disappear, indicating a bcc-to-hcp phase transformation. Also, the period of oscillation is seen to increase, indicating compression. Finally, the damping rate increases, indicating heating.

To understand the origin of the W feature, we show the major components of the full EXAFS spectra calculated by the FEFF8 code for the bcc and hcp crystals in Fig. 103.47. The contributions from the first several shells of nearest neighbors, including several multiple scattering paths, are shown. Both crystals were assumed to be compressed by 20% and to have a temperature of 700 K. The calculation of a bcc crystal compression by 20% may seem unwarranted because the bcc phase is known to transform into the hcp phase at compressions above ~6%. However, because of the much higher strain rate in this experiment, the phase transformation cannot be assumed *a priori* to take place. The origin of the W feature is seen to be a coincidence in the waves scattered from the $n = 3$ and $n = 4$ shells occurring (for this compression) at $k \sim 4.7$ Å^{-1}. No such coincidence occurs for the hcp crystal. As mentioned before, the W feature is seen to remain intact even under compression. Thus, the disappearance of the W feature upon shocking in this experiment is not due to compression, but rather by phase transformation.

We now turn to FEFF fitting to the experimental EXAFS spectra. As Fig. 103.46 shows, we cannot fit the data with bcc EXAFS spectra; the two are qualitatively different. Conversely,

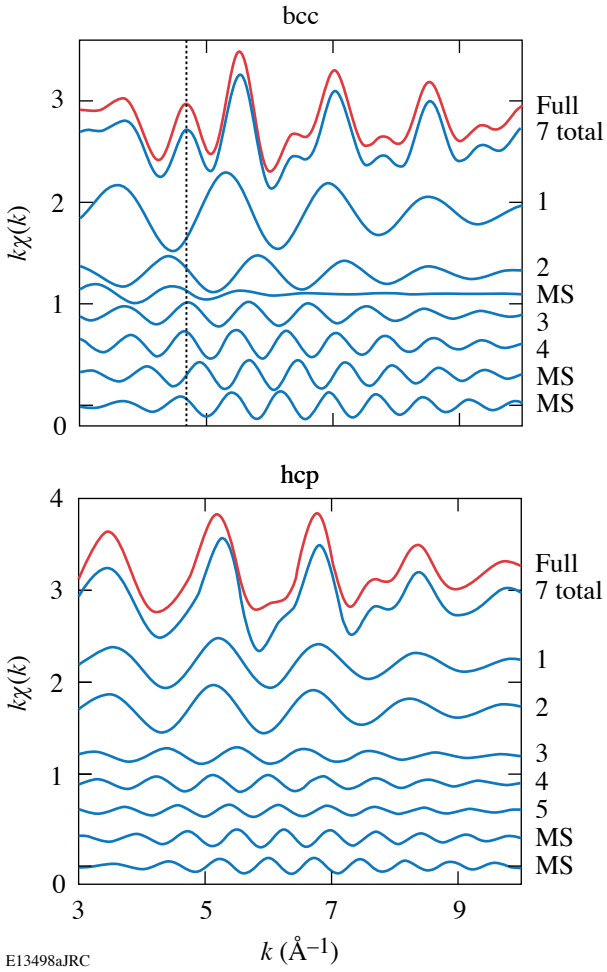

Figure 103.47
The major components of the FEFF-calculated EXAFS spectra due to scattering from the various shells of neighbors around the absorbing atom. The contributions of significant multiple scatterings are also shown ("7 total" is the sum of only the components shown in the figure). The peak marked W in Fig. 103.46 is marked here by a dotted vertical line. It is seen to arise from a coincidence in the scattering from the third and fourth shells at k ~4.7 Å^{-1}. Both crystals are assumed to be compressed by 20% and to be heated to 700 K.

hcp-calculated EXAFS agrees well with the experimental EXAFS data. Figure 103.48 shows the best fit, in wave number (k) space and in distance (r) space. The fit in r space (where the spectrum shows the spatial charge distribution around the absorbing atom) is obtained by inverse Fourier transforming the experimental, as well as the theoretical, curves in k space.[15] The dimensions a and c of the hcp unit cell are known as a function of hydrostatic compression[18] (for all compressions c/a ~ 1.6), and thus, the bond length (or nearest-neighbor distance) R is simply related to the compression under such conditions (we discuss the implications of finite shear strength below). Note that the value of R corresponding to the best fit is larger than the position of the peak in Fig. 103.48(b) because of the phase factors in the wave scattering. The fitting yields R = (2.39±0.0133) Å, which corresponds to a compression of 1.22±0.023. This value agrees well with the average compression of 1.2 predicted by *LASNEX* [see Fig. 103.43(b)]. Turning now to the estimate of temperature, the FEFF best fit to the data [Fig. 103.49(a)] corresponds to $\sigma^2 = 0.0078 \pm 0.0030$ Å^2. From Fig. 103.44, this value of σ^2 corresponds to a temperature of 670±170 K, thus agreeing well with the average temperature of 645 K predicted by *LASNEX* [Fig. 103.43(a)]. Using the equation of state of iron and the measured temperature and compression values leads to an estimate of the pressure as ~35 GPa. *LASNEX* uses the equation of state of iron, which includes the α to ε phase transformation (but not its kinetics). These values also agree with the equation of state calculated for the Hugoniot of iron.[19] The deduced pressure is well above

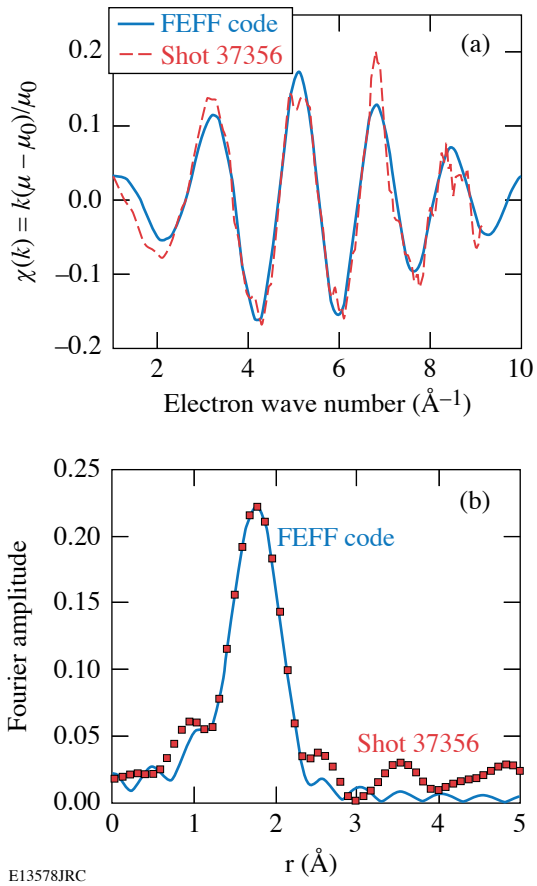

Figure 103.48
FEFF code fitting to the experimental results (a) in the k space and (b) in the r space. The simulations assume the hcp phase. The best fit corresponds to a bond length of R = (2.39±0.013) Å and σ^2 = (0.0078±0.0030) Å^2. These values correspond to a 20% volume compression and a temperature of 670 K.

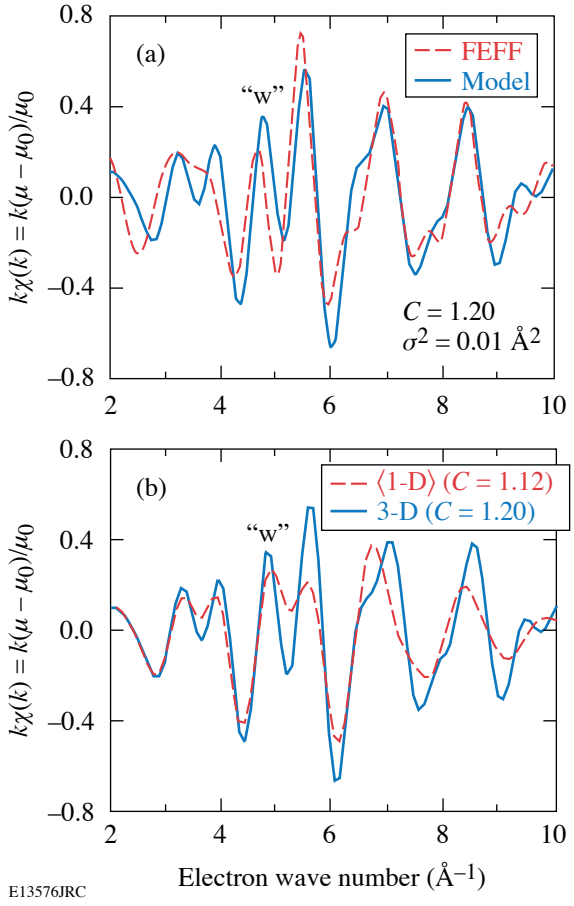

Figure 103.49
Simplified EXAFS calculations for 1-D and 3-D–compressed bcc iron. (a) Comparison of the simplified results and a full FEFF8 calculation for 3-D–compressed iron [$C = (\rho/\rho_0) = 1.2$, T = 700 K]. (b) Two simplified EXAFS calculations: 3-D compression of C = 1.2 and 1-D compression of C = 1.12 (averaged over all directions). The compression in each case is adjusted to yield the measured EXAFS modulation frequency.

the pressure of slower shocks in iron, where a bcc-to-hcp phase transformation takes place.[18] Also, the derived values of pressure and temperature correspond to a point on the phase diagram of iron[5] that is well within the Fe-ε (hcp) region.

Velocity interferometric measurements (VISAR)[20] were performed on iron targets identical to those used for the EXAFS measurements, except that the CH coating was placed only on the side facing the laser. In this way, the velocity of the iron-free back surface could be measured. From the surface velocity, the particle velocity could be determined by dividing by 2. This relationship has been shown[21] to hold for iron shocked to pressures of up to ~150 GPa. Because of the relatively high pressure and the small foil thickness in this experiment, the velocity waves[7,8] indicative of a transition to plastic flow and of a phase transformation were not resolved; thus, the VISAR results cannot confirm either transition. However, the deduced particle velocity can be used with the known Hugoniot curve of iron to determine the compression. For the measured rear-surface velocity of 1.5×10^5 cm/s, the resulting compression is $C = 1.17$, in agreement with the values predicted by *LASNEX* and with the values measured by EXAFS (using the FEFF8-code fitting).

Elastic-to-Plastic Transition

The analysis above has assumed that the compression of the hcp crystal, but not necessarily that of the bcc crystal, is hydrostatic. The dynamic yield stress in polycrystalline iron has been found to be lower than 1 GPa,[22] using millimeter-scale specimen thicknesses and strain rates of order of $10^5\ s^{-1}$. Because the dynamic yield stress in iron increases with strain rate as well as with decreasing specimen thickness,[22] we cannot assume plastic compression of the bcc crystal prior to the phase transformation; in thin iron samples, the Hugoniot elastic limit can even be higher than the pressure for phase transformation.[23] However, the transformation involves atomic motions in various mutually perpendicular directions in the bcc phase,[10,24] and thus, also in a direction perpendicular to the shock direction; this should lead to relaxation of the shear stress. In the hcp phase, the first shell of nearest neighbors, whose distance is given by the unit-cell parameter a, has a major contribution to the EXAFS spectrum; thus, the analysis primarily determines a, whereas the unit-cell parameter c is primarily needed for the calculation of volume compression. Therefore, values of c/a somewhat different from the static values used here cannot be excluded. However, such values would still imply a compression consistent within experimental error with the compression obtained by VISAR measurements and by hydrodynamic simulations.

Since the possibility of elastic compression of the bcc crystal cannot be discounted, the following question arises: Can the observed EXAFS be explained by a 1-D compression of the bcc crystal *with no* phase transformation? In other words: Would the W peak disappear because of 1-D compression where no phase transformation takes place? To answer this question, we calculated the EXAFS spectrum assuming that atomic coordinates in the bcc crystal are reduced only in the shock direction. Since the grains are oriented randomly in a polycrystalline sample, the angles between the crystal axes and the shock direction assume all possible values. Therefore, the result was averaged over all these angles. For simplicity, only single scattering from the first four nearest-neighbor shells was considered, using the scattering amplitudes and phase shifts from the tables of Teo and Lee.[25] To check the reliability of this model, Fig. 103.49(a) shows a comparison between the simplified and the full FEFF8 calculation for 20% isotropic compression of bcc iron at $T = 700$ K. Fair agreement between the two calculations is seen, and, in particular, the W feature appears in both. The W feature in both cases arises from the same coincidence of $n = 3$ and $n = 4$ scatterings. Figure 103.49(b) shows a comparison between the results for the cases of 3-D and 1-D compressions. The 3-D compression is 20%, as above. The 1-D compression was varied to match the experimental frequency of modulation, resulting in 12% compression (in slower shocks, the transformation starts to occur at a compression of ~6%). This is larger than the reduction in distances in the 3-D case (which is $1.2^{1/3} \sim 1.06$) because in 1-D compression distances not in the direction of compression are reduced by a smaller factor. Since the W feature has not disappeared upon 1-D compression (nor has the first peak increased in intensity), the measured EXAFS spectra cannot be explained as resulting from a 1-D compression without a phase transformation. Thus, only the analysis assuming the hcp phase agrees with the measurement. As shown above, this conclusion agrees with VISAR measurements and *LASNEX* predictions.

ACKNOWLEDGMENT

This work was supported by the U.S. Department of Energy Office of Inertial Confinement Fusion under Cooperative Agreement No. DE-FC52-92SF19460, the University of Rochester, and the New York State Energy Research and Development Authority. The support of DOE does not constitute an endorsement by DOE of the views expressed in this article. Portions of this research were carried out at the Stanford Synchrotron Radiation Laboratory, a national user facility operated by Stanford University on behalf of the U.S. Department of Energy, Office of Basic Energy Sciences. Portions of this work were performed under the auspices of the U. S. Department of Energy by the University of California, Lawrence Livermore National Laboratory (LLNL) under Contract No. W-7405-Eng-48. Additional support was provided by LDRD project 04-ERD-071 at LLNL.

REFERENCES

1. J. E. Dorn and S. Rajnak, Trans. Metall. Soc. AIME **230**, 1052 (1964); U. F. Kocks, A. S. Argon, and M. F. Ashby, *Thermodynamics and Kinetics of Slip*, 1st ed., Progress in Materials Science, Vol. 19 (Pergamon Press, Oxford, 1975); M. A. Meyers and L. E. Murr, eds. *Shock Waves and High-Strain-Rate Phenomena in Metals: Concepts and Applications* (Plenum Press, New York, 1981).
2. B. A. Remington, G. Bazan, J. Belak, E. Bringa, M. Caturla, J. D. Colvin, M. J. Edwards, S. G. Glendinning, D. S. Ivanov, B. Kad, D. H. Kalantar, M. Kumar, B. F. Lasinski, K. T. Lorenz, J. M. McNaney, D. D. Meyerhofer, M. A. Meyers, S. M. Pollaine, D. Rowley, M. Schneider, J. S. Stölken, J. S. Wark, S. V. Weber, W. G. Wolfer, B. Yaakobi, and L. V. Zhigilei, Metall. Mater. Trans. A **35A**, 2587 (2004).
3. B. Yaakobi, D. D. Meyerhofer, T. R. Boehly, J. J. Rehr, B. A. Remington, P. G. Allen, S. M. Pollaine, and R. C. Albers, Phys. Rev. Lett. **92**, 095504 (2004); B. Yaakobi, D. D. Meyerhofer, T. R. Boehly, J. J. Rehr, B. A. Remington, P. G. Allen, S. M. Pollaine, and R. C. Albers, Phys. Plasmas **11**, 2688 (2004).
4. G. Steinle-Neumann *et al*. Nature **413**, 57 (2001).
5. D. Bancroft, E. L. Peterson, and S. Minshall, J. Appl. Phys. **27**, 291 (1956).
6. J. C. Jamieson and A. W. Lawson, J. Appl. Phys. **33**, 776 (1962).
7. L. M. Barker and R. E. Hollenbach, J. Appl. Phys. **45**, 4872 (1974).
8. J. C. Boettger and D. C. Wallace, Phys. Rev. B **55**, 2840 (1997).
9. C. S. Smith, Trans. Am. Inst. Min. Pet. Eng. **212**, 574 (1958); T. Sano *et al*., Appl. Phys. Lett. **83**, 3498 (2003).
10. F. M. Wang and R. Ingalls, Phys. Rev. B **57**, 5647 (1998).
11. T. R. Boehly, R. S. Craxton, T. H. Hinterman, J. H. Kelly, T. J. Kessler, S. A. Kumpan, S. A. Letzring, R. L. McCrory, S. F. B. Morse, W. Seka, S. Skupsky, J. M. Soures, and C. P. Verdon, Rev. Sci. Instrum. **66**, 508 (1995).
12. B. Yaakobi, F. J. Marshall, T. R. Boehly, R. P. J. Town, and D. D. Meyerhofer, J. Opt. Soc. Am. B **20**, 238 (2003).
13. G. B. Zimmerman and W. L. Kruer, Comments Plasma Phys. Control. Fusion **2**, 51 (1975).
14. J. J. Rehr, R. C. Albers, and S. I. Zabinsky, Phys. Rev. Lett. **69**, 3397 (1992).
15. P. A. Lee *et al*., Rev. Mod. Phys. **53**, 769 (1981).
16. E. Sevillano, H. Meuth, and J. J. Rehr, Phys. Rev. B, Condens. Matter **20**, 4908 (1979).
17. L. S. Dubrovinsky *et al*., Am. Mineral. **85**, 386 (2000).
18. A. P. Jephcoat, H. K. Mao, and P. M. Bell, J. Geophys. Res. **91**, 4677 (1986).
19. R. G. McQueen *et al*., in *High-Velocity Impact Phenomena*, edited by R. Kinslow (Academic Press, New York, 1970), Chap. VII, pp. 293–417.
20. P. M. Celliers *et al*., Appl. Phys. Lett. **73**, 1320 (1998).
21. L. V. Al'tshuler *et al*., Sov. Phys.-JETP **11**, 573 (1960).
22. R. W. Rohde, Acta Metall. **17**, 353 (1969).
23. G. E. Duvall, P. M. Bellamy, and R. J. Livak, in *Shock Waves and High-Strain-Rate Phenomena in Metals: Concepts and Applications*, edited by M. A. Meyers and L. E. Murr (Plenum Press, New York, 1981), Chap. 40, pp. 717–732.
24. V. P. Dmitriev, Y. M. Gufan, and P. Toledano, Phys. Rev. B **44**, 7248 (1991).
25. B.-K. Teo and P. A. Lee, J. Am. Chem. Soc. **101**, 2815 (1979).

Publications and Conference Presentations

Publications

S. Chen, P. Zhang, W. Theobald, N. Saleh, M. Rever, A. Maksimchuk, and D. Umstadter, "Evidence of Ionization Blue Shift Seeding of Forward Raman Scattering," in *Advanced Accelerator Concepts: Eleventh Workshop*, edited by V. Yakimenko (American Institute of Physics, Melville, NY, 2004), Vol. 737, pp. 585–591.

T. J. B. Collins, A. Poludnenko, A. Cunningham, and A. Frank, "Shock Propagation in Deuterium-Tritium-Saturated Foam," Phys. Plasmas **12**, 062705 (2005).

R. S. Craxton and D. W. Jacobs-Perkins, "The Saturn Target for Polar Direct Drive on the National Ignition Facility," Phys. Rev. Lett. **94**, 095002 (2005).

R. S. Craxton, F. J. Marshall, M. J. Bonino, R. Epstein, P. W. McKenty, S. Skupsky, J. A. Delettrez, I. V. Igumenshchev, D. W. Jacobs-Perkins, J. P. Knauer, J. A. Marozas, P. B. Radha, and W. Seka, "Polar Direct Drive: Proof-of-Principle Experiments on OMEGA and Prospects for Ignition on the National Ignition Facility," Phys. Plasmas **12**, 056304 (2005) (invited).

V. N. Goncharov and D. Li, "Effects of Temporal Density Variation and Convergent Geometry on Nonlinear Bubble in Classical Rayleigh–Taylor Instability," Phys. Rev. E **71**, 046306 (2005).

L. Guazzotto and R. Betti, "Magnetohydrodynamics Equilibria with Toroidal and Poloidal Flow," Phys. Plasmas **12**, 056107 (2005) (invited).

D. R. Harding, F.-Y. Tsai, E. L. Alfonso, S. H. Chen, A. K. Knight, and T. N. Blanton, "Properties of Vapor-Deposited Polyimides," in *Polyimides and Other High Temperature Polymers: Synthesis, Characterizations and Applications*, edited by K. L. Mittal (VSP, Utrecht, The Netherlands, 2005), Vol. 3, pp. 49–67 (invited).

B. Hu, R. Betti, and J. Manickam, "Application of the Low-Frequency Energy Principle to Wall Modes," Phys. Plasmas **12**, 057301 (2005).

J. Kitaygorsky, J. Zhang, A. Verevkin, A. Sergeev, A. Korneev, V. Matvienko, P. Kouminov, K. Smirnov, B. Voronov, G. Gol'tsman, and R. Sobolewski, "Origin of Dark Counts in Nanostructured NbN Single-Photon Detectors," IEEE Trans. Appl. Supercond. **15**, 545 (2005).

J. P. Knauer, K. Anderson, R. Betti, T. J. B. Collins, V. N. Goncharov, P. W. McKenty, D. D. Meyerhofer, P. B. Radha, S. P. Regan, T. C. Sangster, V. A. Smalyuk, J. A. Frenje, C. K. Li, R. D. Petrasso, and F. H. Séguin, "Improved Target Stability Using Picket Pulses to Increase and Shape the Ablator Adiabat," Phys. Plasmas **12**, 056306 (2005) (invited).

A. Korneev, V. Matvienko, O. Minaeva, I. Milostnaya, I. Rubtsova, G. Chulkova, K. Smirnov, V. Voronov, G. Gol'tsman, W. Słysz, A. Pearlman, A. Verevkin, and R. Sobolewski, "Quantum Efficiency and Noise Equivalent Power of Nanostructured, NbN, Single-Photon Detectors in the Wavelength Range from Visible to Infrared," IEEE Trans. Appl. Supercond. **15**, 571 (2005).

T. Z. Kosc, "Particle Display Technologies Become E-Paper," Opt. Photonics News **16**, 18 (2005).

X. Li, Y. Xu, Š. Chromik, V. Štrbík, P. Odier, D. De Barros, and R. Sobolewski, "Time-Resolved Carrier Dynamics in Hg-Based High-Temperature Superconducting Photodetectors," IEEE Trans. Appl. Supercond. **15**, 622 (2005).

F. J. Marshall, R. S. Craxton, J. A. Delettrez, D. H. Edgell, L. M. Elasky, R. Epstein, V. Yu. Glebov, V. N. Goncharov, D. R. Harding, R. Janezic, R. L. Keck, J. D. Kilkenny, J. P. Knauer, S. J. Loucks, L. D. Lund, R. L. McCrory, P. W. McKenty, D. D.

Meyerhofer, P. B. Radha, S. P. Regan, T. C. Sangster, W. Seka, V. A. Smalyuk, J. M. Soures, C. Stoeckl, S. Skupsky, J. A. Frenje, C. K. Li, R. D. Petrasso, and F. H. Séguin, "Direct-Drive, Cryogenic Target Implosions on OMEGA," Phys. Plasmas **12**, 056302 (2005) (invited).

M. Mikulics, M. Marso, P. Javorka, P. Kordoš, H. Lüth, M. Kocan, A. Rizzi, S. Wu, and R. Sobolewski, "Ultrafast Metal-Semiconductor-Metal Photodetectors on Low-Temperature-Grown GaN," Appl. Phys. Lett. **86**, 211110 (2005).

S. Papernov and A. W. Schmid, "Two Mechanisms of Crater Formation in Ultraviolet-Pulsed-Laser Irradiated SiO_2 Thin Films with Artificial Defects," J. Appl. Phys. **97**, 114906 (2005).

A. Pearlman, A. Cross, W. Słysz, J. Zhang, A. Verevkin, M. Currie, A. Korneev, P. Kouminov, K. Smirnov, B. Voronov, G. Gol'tsman, and R. Sobolewski, "Gigahertz Counting Rates of NbN Single-Photon Detectors for Quantum Communications," IEEE Trans. Appl. Supercond. **15**, 579 (2005).

G. P. Pepe, L. Parlato, R. Latempa, P. D'Acunto, N. Marrocco, C. De Lisio, C. Altucci, G. Peluso, A. Barone, T. Taneda, and R. Sobolewski, "Fabrication and Optical Properties of Ultrathin Ferromagnet/Superconductor Metallic Bilayers," IEEE Trans. Appl. Supercond. **15**, 2942 (2005).

P. B. Radha, T. J. B. Collins, J. A. Delettrez, Y. Elbaz, R. Epstein, V. Yu. Glebov, V. N. Goncharov, R. L. Keck, J. P. Knauer, J. A. Marozas, F. J. Marshall, R. L. McCrory, P. W. McKenty, D. D. Meyerhofer, S. P. Regan, T. C. Sangster, W. Seka, D. Shvarts, S. Skupsky, Y. Srebro, and C. Stoeckl, "Multidimensional Analysis of Direct-Drive, Plastic-Shell Implosions on OMEGA," Phys. Plasmas **12**, 056307 (2005) (invited).

J. A. Randi, J. C. Lambropoulos, and S. D. Jacobs, "Subsurface Damage in Some Single Crystalline Optical Materials," Appl. Opt. **44**, 2241 (2005).

S. P. Regan, J. A. Marozas, R. S. Craxton, J. H. Kelly, W. R. Donaldson, P. A. Jaanimagi, D. Jacobs-Perkins, R. L. Keck, T. J. Kessler, D. D. Meyerhofer, T. C. Sangster, W. Seka, V. A. Smalyuk, S. Skupsky, and J. D. Zuegel, "Performance of a 1-THz-Bandwidth, Two-Dimensional Smoothing by Spectral Dispersion and Polarization Smoothing of High-Power, Solid-State Laser Beams," J. Opt. Soc. Am. B **22**, 998 (2005).

S. P. Regan, T. C. Sangster, D. D. Meyerhofer, K. Anderson, R. Betti, T. R. Boehly, T. J. B. Collins, R. S. Craxton, J. A. Delettrez, R. Epstein, O. V. Gotchev, V. Yu. Glebov, V. N. Goncharov, D. R. Harding, P. A. Jaanimagi, J. P. Knauer, S. J. Loucks, L. D. Lund, J. A. Marozas, F. J. Marshall, R. L. McCrory, P. W. McKenty, S. F. B. Morse, P. B. Radha, W. Seka, S. Skupsky, H. Sawada, V. A. Smalyuk, J. M. Soures, C. Stoeckl, B. Yaakobi, J. A. Frenje, C. K. Li, R. D. Petrasso, and F. H. Séguin, "Direct-Drive Inertial Confinement Fusion Implosions on OMEGA," Astrophys. Space Sci. **298**, 227 (2005).

V. A. Smalyuk, J. A. Delettrez, S. B. Dumanis, R. Epstein, V. Yu. Glebov, D. D. Meyerhofer, P. B. Radha, S. P. Regan, T. C. Sangster, C. Stoeckl, N. C. Toscano, J. A. Frenje, C. K. Li, R. D. Petrasso, F. H. Séguin, and J. A. Koch, "Hot-Core Characterization of Direct-Drive Spherical Cryogenic D_2 Target Implosion," Phys. Plasmas **12**, 052706 (2005).

V. A. Smalyuk, V. N. Goncharov, T. R. Boehly, J. A. Delettrez, D. Y. Li, J. A. Marozas, A. V. Maximov, D. D. Meyerhofer, S. P. Regan, and T. C. Sangster, "Measurements of Laser-Imprinting Sensitivity to Relative Beam Mistiming in Planar Plastic Foils Driven by Multiple Overlapping Laser Beams," Phys. Plasmas **12**, 072703 (2005).

V. A. Smalyuk, V. N. Goncharov, T. R. Boehly, J. A. Delettrez, D. Y. Li, J. A. Marozas, D. D. Meyerhofer, S. P. Regan, and T. C. Sangster, "Angular Dependence of Imprinting Levels in Laser-Target Interactions on Planar CH Foils," Phys. Plasmas **12**, 040702 (2005).

X. Teng and H. Yang, "Synthesis of Magnetic Nanocomposites and Alloys from Platinum–Iron Oxide Core–Shell Nanoparticles," Nanotechnology **16**, S554 (2005).

X. Teng and H. Yang, "Synthesis of Platinum Multipods: An Induced Anisotropic Growth," Nano Lett. **5**, 885 (2005).

Y. Wang and H. Yang, "Synthesis of CoPt Nanorods in Ionic Liquids," J. Am. Chem. Soc. **127**, 5316 (2005).

B. Yaakobi, C. Stoeckl, W. Seka, J. A. Delettrez, T. C. Sangster, and D. D. Meyerhofer, "Measurement of Preheat Due to Fast Electrons in Laser Implosions of Cryogenic Deuterium Targets," Phys. Plasmas **12**, 062703 (2005).

J. K. W. Yang, E. Dauler, A. Ferri, A. Pearlman, A. Verevkin, G. Gol'tsman, B. Voronov, R. Sobolewski, W. E. Keicher, and K. K. Berggren, "Fabrication Development for Nanowire GHz-Counting-Rate Single-Photon Detectors," IEEE Trans. Appl. Supercond. **15**, 626 (2005).

Forthcoming Publications

Y. V. Artemova, G. S. Bisnovatyi-Kogan, I. V. Igumenshchev, and I. D. Novikov, "Black Hole Advective Accretion with Optical Depth Transition," to be published in the Astrophysical Journal.

V. Bagnoud, I. A. Begishev, M. J. Guardalben, J. Puth, and J. D. Zuegel, "A 5-Hz, 250-mJ Optical Parametric Chirped-Pulse Amplifier at 1053 nm with New Ideal Performance," to be published in Optics Letters.

D. Clay, D. Poslunsy, M. Flinders, S. D. Jacobs, and R. Cutler, "Effect of $LiAl_5O_8$ Additions on the Sintering and Optical Transparency of LiAlON," to be published in the Journal of European Ceramic Society.

S. Costea, S. Pisana, N. P. Kherani, F. Gaspari, T. Kosteski, W. T. Shmayda, and S. Zukotynski, "The Use of Tritium in the Study of Defects in Amorphous Silicon," to be published in Fusion Science and Technology.

J. E. DeGroote, A. E. Marino, K. E. Spencer, and S. D. Jacobs, "Power Spectral Density Plots Inside MRF Spots Made with a Polishing Abrasive-Free MR Fluid," to be published in the Proceedings of Optifab.

W. R. Donaldson, M. Millecchia, and R. L. Keck, "A Multichannel, High-Resolution, UV Spectrometer for Laser Fusion Applications," to be published in Review of Scientific Instruments.

D. H. Edgell, W. Seka, R. S. Craxton, L. M. Elasky, D. R. Harding, R. L. Keck, and M. D. Wittman, "Analysis of Cryogenic Target Shadowgraphs at LLE," to be published in Fusion Science and Technology.

R. A. Forties and F. J. Marshall, "*In-Situ* Characterization of High-Intensity Laser Beams on OMEGA," to be published in Review of Scientific Instruments.

D. R. Harding, T. C. Sangster, D. D. Meyerhofer, P. W. McKenty, L. D. Lund, and T. H. Hinterman, "Producing Cryogenic Deuterium Targets for Experiments on OMEGA," to be published in Fusion Science and Technology.

A. Jukna, I. Barboy, G. Jung, X. Li, D. Wang, R. Sobolewski, S. S. Banerjee, Y. Myasoedov, V. Plausinaitiene and A. Abrutis, "Optically-Modified Channels of Easy Vortex Motion in $YBa_2Cu_3O_{7-x}$ films," to be published in Applied Physics Letters.

A. K. Knight and D. R. Harding, "Modeling the Sensitivity of a Polymer Vapor Deposition Process to Different Operating Conditions and Parameters," to be published in Fusion Science and Technology.

T. Z. Kosc, K. L. Marshall, S. D. Jacobs, and J. C. Lambropoulos, "Polymer Cholesteric Liquid Crystal Flake Reorientation in an Alternating-Current Electric Field," to be published in the Journal of Applied Physics.

T. Kosteski, N. P. Kherani, W. T. Shmayda, S. Costea, and S. Zukotynski, "Nuclear Batteries Using Tritium and Thin-Film Hydrogenated Amorphous Silicon," to be published in Fusion Science and Technology.

I. A. Kozhinova, H. J. Romanofsky, A. Maltsev, S. D. Jacobs, W. I. Kordonski, and S. R. Gorodkin, "Minimizing Artifact Formation in Magnetorheological Finishing of CVD ZnS Flats," to be published in Applied Optics.

R. L. McCrory, S. P. Regan, S. J. Loucks, D. D. Meyerhofer, S. Skupsky, R. Betti, T. R. Boehly, R. S. Craxton, T. J. B. Collins, J. A. Delettrez, D. H. Edgell, R. Epstein, V. Yu. Glebov, V. N. Goncharov, D. R. Harding, R. L. Keck, J. P. Knauer, J. Marciante, J. A. Marozas, F. J. Marshall, A. V. Maximov, P. W. McKenty, J. Myatt, P. B. Radha, T. C. Sangster, W. Seka, V. A. Smalyuk, J. M. Soures, C. Stoeckl, B. Yaakobi, J. D. Zuegel, C. K. Li, R. D. Petrasso, F. H. Séguin, J. A. Frenje, S. Padalino, C. Freeman, and K. Fletcher, "Direct-Drive Inertial Confinement Fusion Research at the Laboratory for Laser Energetics: Charting the Path to Thermonuclear Ignition," to be published in Nuclear Fusion.

M. Mikulics, R. Adam, M. Marso, A. Förster, P. Kordoš, H. Lüth, S. Wu, X. Zheng, and R. Sobolewski, "Ultrafast Low-Temperature-Grown Epitaxial GaAs Photodetectors Transferred on Flexible Plastic Substrates," to be published in IEEE Photonics Technology Letters.

M. Mikulics, M. Marso, I. C. Mayorga, R. Güsten, S. Stancek, P. Kovác, S. Wu, X. Li, M. Khafizov, R. Sobolewski, E. A. Michael, R. Schieder, M. Wolter, D. Buca, A. Förster, P. Kordoš, and H. Lüth, "Photomixers Fabricated on Nitrogen-Ion-Implanted GaAs," to be published in Applied Physics Letters.

L. Parlato, R. Latempa, G. Peluso, G. P. Pepe, R. Cristiano, and R. Sobolewski, "Characteristic Electron-Phonon Coupling Times in Unconventional Superconductors and Implications for Optical Detectors," to be published in Superconductor Science and Technology.

W. T. Shmayda, R. Janezic, T. W. Duffy, D. R. Harding, and L. D. Lund, "Tritium Operations at the Laboratory for Laser Energetics," to be published in Fusion Science and Technology.

D. Wang, A. Verevkin, R. Sobolewski, R. Adam, A. van der Hart, and R. Franchy, "Magneto-Optical Kerr Effect Measurements and Ultrafast Coherent Spin Dynamics in Co Nano-Dots," to be published in IEEE Transactions on Nanotechnology.

L. J. Waxer, D. N. Maywar, J. H. Kelly, T. J. Kessler, B. E. Kruschwitz, S. J. Loucks, R. L. McCrory, D. D. Meyerhofer, S. F. B. Morse, C. Stoeckl, and J. D. Zuegel, "High-Energy Petawatt Capability for the OMEGA Laser," to be published in Optics and Photonics News.

B. Yaakobi, T. R. Boehly, D. D. Meyerhofer, T. J. B. Collins, B. A. Remington, P. G. Allen, S. M. Pollaine, H. E. Lorenzana, and J. H. Eggert, "EXAFS Measurements of Iron bcc-to-hcp Phase Transformation in Nanosecond-Laser Shocks," to be published in Physical Review Letters.

B. Yaakobi, T. R. Boehly, D. D. Meyerhofer, T. J. B. Collins, B. A. Remington, P. G. Allen, S. M. Pollaine, H. E. Lorenzana, and J. H. Eggert, "EXAFS Measurement of Iron bcc-hcp Phase Transformation in Nanosecond-Laser Shocks," to be published in Physics of Plasmas.

L. Zheng, J. C. Lambropoulos, and A. W. Schmid, "Molecular Dynamics Study of UV-Laser-Induced Densification of Fused Silica. II. Effects of Laser Pulse Duration, Pressure, and Temperature, and Comparison with Pressure-Induced Densification," to be published in the Journal of Non-Crystalline Solids.

Conference Presentations

L. Guazzotto, R. Betti, and J. P. Freidberg, "Progress in the Development of a Linear MHD Stability Code for Axisymmetric Plasmas with Arbitrary Equilibrium Flow," 2005 International Sherwood Fusion Theory Conference, Stateline, NV, 11–13 April 2005.

The following presentations were made at the 16th Target Fabrication Specialist's Meeting, Scottsdale, AZ, 1–5 May 2005:

M. J. Bonino, S. G. Noyes, F. J. Marshall, R. S. Craxton, D. W. Turner, and D. R. Harding, "Fabrication of Polar-Direct-Drive Targets for the National Ignition Facility."

D. H. Edgell, W. Seka, R. S. Craxton, L. M. Elasky, D. R. Harding, R. L. Keck, and M. D. Wittman, "Analysis of Cryogenic Target Shadowgraphs at LLE."

L. M. Elasky, S. Verbridge, D. H. Edgell, and D. R. Harding, "Improvements and Present Limitations of D_2 Ice Layers for OMEGA Cryogenic Targets."

R. Q. Gram and D. R. Harding, "Thermal Conductivity of Solid, Liquid, and Gaseous D_2 and Precise Thermometry Using an Embedded Pt Wire."

D. R. Harding, M. D. Wittman, L. M. Elasky, R. Q. Gram, M. J. Bonino, L. D. Lund, R. Janezic, S. Verbridge, S. Scarantino, and M. Bobeica, "Overview of Cryogenic Target Research at LLE."

A. K. Knight and D. R. Harding, "Modeling the Sensitivity of a Polymer Vapor Deposition Process to Different Operating Conditions and Parameters."

D. D. Meyerhofer, "Innovative Target Designs for Direct-Drive Ignition."

W. T. Shmayda, D. R. Harding, L. D. Lund, R. Janezic, and T. W. Duffy, "Handling Cryogenic DT Targets at the Laboratory for Laser Energetics."

D. Turner, M. J. Bonino, S. G. Noyes, R. Q. Gram, K. J. Lintz, S. Scarantino, S. Verbridge, and D. R. Harding, "Fabricating, Testing, and Fielding of Planar Cryogenic and X-Ray Scattering Targets."

M. D. Wittman and D. R. Harding, "Freezing Behavior of H_2–HD–D_2 Mixtures."

J. E. DeGroote, A. E. Marino, K. E. Spencer, and S. D. Jacobs, "Power Spectral Density Plots Inside MRF Spots Made with a Polishing Abrasive-Free MR Fluid," Optifab 2005, Rochester, NY, 2–5 May 2005.

The following presentations were made at ICONO/LAT 2005, St. Petersburg, Russia, 11–15 May 2005:

A. V. Okishev, "OMEGA EP (Extended Performance): Adding High-Energy, Short-Pulse Capability to the OMEGA Facility."

A. V. Okishev, K. P. Dolgaleva, and J. D. Zuegel, "Experimental Optimization of Diode-Pumped Yb:GdCOB Laser Performance for Broadband Amplification at 1053 nm."

A. V. Okishev, R. G. Roides, I. A. Begishev, and J. D. Zuegel, "All-Solid-State, Diode-Pumped, Multiharmonic Laser System for a Timing Fiducial."

The following presentations were made at CLEO 2005, Baltimore, MD, 22–27 May 2005:

V. Bagnoud, J. Puth, I. A. Begishev, J. Bromage, M. J. Guardalben, and J. D. Zuegel, "A Multiterawatt Laser Using a High-Contrast, Optical Parametric Chirped-Pulse Preamplifier."

Z. Jiang and J. R. Marciante, "Mode-Area Scaling of Helical-Core, Dual-Clad Fiber Lasers and Amplifiers."

J. R. Marciante and J. D. Zuegel, "High-Gain, Polarization Preserving, Yb-Doped Fiber Amplifier for Low-Duty-Cycle Pulse Amplification."

N. G. Usechak and G. P. Agrawal, "An Analytic Technique for Investigating Mode-Locked Lasers."

N. G. Usechak and G. P. Agrawal, "Pulse-Switching and Stability in FM Mode-Locked Fiber Lasers."

S. G. Lukishova, A. W. Schmid, R. Knox, P. Freivald, R. W. Boyd, C. R. Stroud, Jr., and K. L. Marshall, "Deterministically Polarized Fluorescence from Single-Dye Molecules Aligned in Liquid Crystal Host," QELS 2005, Baltimore, MD, 22–27 May 2005.

The following presentations were made at the 32nd IEEE International Conference on Plasma Science, Monterey, CA, 18–23 June 2005:

V. Yu. Glebov, R. A. Lerche, C. Stoeckl, G. J. Schmid, T. C. Sangster, J. A. Koch, T. W. Phillips, C. Mileham, and S. Roberts, "Progress with CVD Diamond Detectors for ICF Time-of-Flight Applications."

W. Theobald, T. R. Boehly, E. Vianello, J. E. Miller, R. S. Craxton, V. N. Goncharov, I. V. Igumenshchev, D. D. Meyerhofer, D. G. Hicks, P. M. Celliers, and G. W. Collins, "Direct-Drive Shockwave-Timing Experiments in Planar Targets" (invited).

The following presentations were made at the 35th Annual Anomalous Absorption Conference, Fajardo, Puerto Rico, 26 June–1 July 2005:

R. S. Craxton, F. J. Marshall, M. J. Bonino, V. Yu. Glebov, J. P. Knauer, S. G. Noyes, W. Seka, and V. A. Smalyuk, "Polar-Direct-Drive Experiments on OMEGA Using Saturn Targets."

R. Epstein, T. J. B. Collins, R. S. Craxton, J. A. Delettrez, I. V. Igumenshchev, F. J. Marshall, J. A. Marozas, P. W. McKenty, P. B. Radha, S. Skupsky, and V. A. Smalyuk, "Numerical Investigation of X-Ray Core Images from OMEGA Implosions Driven with Controlled Polar Illumination."

V. N. Goncharov, O. V. Gotchev, and C. Cherfils-Clérouin, "Ablative Richtmyer–Meshkov Instability as a Test of Thermal Conduction Models Used in Hydrosimulations of ICF Experiments."

A. V. Maximov, "Electron Heat Transport in the Laser Field in Direct-Drive ICF Plasmas."

S. P. Regan, H. Sawada, T. R. Boehly, I. V. Igumenshchev, V. N. Goncharov, T. C. Sangster, D. D. Meyerhofer, B. Yaakobi, G. Gregori, D. G. Hicks, S. H. Glenzer, and O. L. Landen, "Diagnosing Shock-Heated, Direct-Drive Plastic Targets with Spectrally Resolved X-Ray Scattering."

T. C. Sangster, R. S. Craxton, J. A. Delettrez, D. H. Edgell, R. Epstein, V. Yu. Glebov, V. N. Goncharov, D. R. Harding, D. Jacobs-Perkins, J. P. Knauer, S. J. Loucks, F. J. Marshall, R. L. McCrory, P. W. McKenty, D. D. Meyerhofer, P. B. Radha, S. P. Regan, W. Seka, V. A. Smalyuk, J. M. Soures, C. Stoeckl, J. A. Frenje, C. K. Li, R. D. Petrasso, and F. H. Séguin, "High-Performance Direct-Drive Implosions Using Cryogenic D_2 Fuel."

W. Seka, H. Baldis, A. V. Maximov, J. Myatt, R. W. Short, R. S. Craxton, R. E. Bahr, and T. C. Sangster, "Various Forms of Stimulated Brillouin Scattering in Long-Scale-Length Plasmas Relevant to Direct-Drive Inertial Confinement Fusion."

R. W. Short and J. Myatt, "Micro-Instabilities of Relativistic Electron Beams in Plasmas."

V. A. Smalyuk, O. Sadot, J. A. Delettrez, D. D. Meyerhofer, S. P. Regan, and T. C. Sangster, "Nonlinear Rayleigh–Taylor Growth Measurements on OMEGA."

The following presentations were made at the 8th International Workshop on Fast Ignition Targets, Tarragona, Spain, 29 June–1 July 2005:

J. A. Delettrez, J. Myatt, P. B. Radha, C. Stoeckl, S. Skupsky, and D. D. Meyerhofer, "Hydrodynamic Simulations of Integrated Experiments Planned for the OMEGA/OMEGA EP Laser Systems."

J. Myatt, J. A. Delettrez, W. Theobald, C. Stoeckl, A. V. Maximov, R. W. Short, M. Storm, T. C. Sangster, R. P. J. Town, and L. A. Cottrill, "Hybrid-Implicit PIC Calculations of Laser-Generated MeV Electrons in Copper Targets."

C. Stoeckl, T. R. Boehly, R. B. Stephens, J. A. Delettrez, S. P. Hatchett, J. A. Frenje, V. Yu. Glebov, C. K. Li, J. Miller, R. D. Petrasso, F. H. Séguin, V. A. Smalyuk, W. Theobald, B. Yaakobi, and T. C. Sangster, "Fuel-Assembly Experiments with Gas-Filled, Cone-in-Shell, Fast-Ignitor Targets on OMEGA."

UNIVERSITY OF
ROCHESTER